

Overview article

A correlative four-dimensional study of phase-separation at the subnanoscale to nanoscale of a Ni–Al alloy

Elizaveta Y. Plotnikov ^a, Zugang Mao ^a, Sung-II Baik ^{a,f}, Mehmet Yildirim ^{a,b}, Yongsheng Li ^{a,c}, Daniel Cecchetti ^a, Ronald D. Noebe ^d, Georges Martin ^{a,e}, David N. Seidman ^{a,f,*}

^a Northwestern University, Department of Materials Science and Engineering, 2220 Campus Drive, Evanston, IL, 60208-3108, USA

^b Department of Metallurgical and Materials Engineering, 42310, Selçuklu, Konya Technical University, Turkey

^c Nanjing University of Science and Technology, School of Materials Science and Engineering, 200 Xiaolingwei, Nanjing, 210094, China

^d NASA Glenn Research Center, Materials and Structures Division, 21000 Brookpark Rd., Cleveland, OH, 44135-3191, USA

^e Directeur de Recherches Émérite, CEA Saclay, 9119, France

^f Northwestern University Center for Atom-Probe Tomography, 2220 Campus Drive, Evanston, IL, 60208-3108, USA

ARTICLE INFO

Article history:

Received 11 November 2018

Received in revised form

13 March 2019

Accepted 14 March 2019

Available online 28 March 2019

Keywords:

Nickel-based superalloys

Atom-probe tomography

Temporal evolution

Monovacancy-mediated lattice kinetic

Monte Carlo

Lifshitz-Slyozov (LS) model

ABSTRACT

The temporal evolution of ordered $\gamma'(\text{L}1_2)$ -precipitates precipitating in a disordered $\gamma(\text{f.c.c.})$ matrix is studied in extensive detail for a Ni-12.5 Al at.% alloy aged at 823 K (550 °C), for times ranging from 0.08 to 4096 h. Three-dimensional atom-probe tomography (3-D APT) results are compared to monovacancy-mediated lattice-kinetic Monte Carlo (LKMC₁) simulations on a rigid lattice, which include monovacancy-solute binding energies through 4th nearest-neighbor distances, for the same mean composition and aging temperature. The temporal evolution of the measured values of the mean radius, $\langle R(t) \rangle$, number density, aluminum supersaturations, and volume fraction of the $\gamma'(\text{L}1_2)$ -precipitates are compared to the predictions of a modified version of the Lifshitz-Slyozov diffusion-limited coarsening model due to Calderon, Voorhees et al. The resulting experimental rate constants are used to calculate the Gibbs interfacial free-energy between the $\gamma(\text{f.c.c.})$ - and $\gamma'(\text{L}1_2)$ -phases, which enter the model, using data from two thermodynamic databases, and its value is compared to all existing values. The diffusion coefficient for coarsening is calculated utilizing the same rate-constants and compared to all archival diffusivities, *not determined from coarsening experiments, and it is demonstrated to be the inter-diffusivity*, \tilde{D} , of Ni and Al. The monovacancy-mediated LKMC₁ simulation results are in good agreement with our 3-D APT data. The compositional interfacial width, for the {100}-interface, between the $\gamma(\text{f.c.c.})$ - and $\gamma'(\text{L}1_2)$ -phases, decreases continuously with increasing aging time and $\langle R(t) \rangle$, both for the 3-D APT results and the monovacancy-mediated LKMC₁ simulations, in disagreement with an *ansatz* intrinsic to the trans-interface diffusion-controlled coarsening model, which assumes the exact opposite trend for binary alloys.

© 2019 Acta Materialia Inc. Published by Elsevier Ltd. All rights reserved.

Contents

1. Introduction	309
1.1. A short history of the interfacial Gibbs free energy of the Ni(f.c.c.)/Ni ₃ Al(L1 ₂) heterophase interface, $\sigma^{\gamma/\gamma'}$	309
1.2. The mean-field coarsening models	310
1.2.1. Lifshitz-Slyozov (LS) mean-field model for diffusion-limited coarsening	310
1.2.2. Calderon-Voorhees-Murray-Kostorz (CVMK) model for diffusion-limited mean-field coarsening	312
1.3. A new methodology for calculating the interfacial Gibbs free energy of the Ni(f.c.c.)/Ni ₃ Al(L1 ₂) interface $\sigma^{\gamma/\gamma'}$	312
1.4. Overview of our current research	313

* Corresponding author. Northwestern University, Department of Materials Science and Engineering, 2220 Campus Drive, Evanston, IL, 60208-3108, USA.

E-mail address: d-seidman@northwestern.edu (D.N. Seidman).

Nomenclature

a_0	lattice parameter of Ni ₃ Al(L1 ₂)	k_B	Boltzmann's constant
$\langle a \rangle$	average of the lattice parameters of the γ (f.c.c.)- and γ' (L1 ₂)-phases	L	ratio of the elastic energy contribution to the interfacial Gibbs free energy contribution to the overall morphology of γ' (L1 ₂)-precipitates
$B^{\gamma'}$	bulk modulus of the γ' (L1 ₂)-phase	L^3	volume of monovacancy-mediated LKMC ₁ simulation box
b_{rand}	random number between 0 and 1	l^{γ}	capillary length in the γ (f.c.c.)- phase
C_{EQ}^V	equilibrium monovacancy concentration in a pure metal	N	total number of possible nucleation sites per unit volume
C_i^{γ}	concentration of element i in the γ (f.c.c.)-phase	N_{ppt}	effective number of γ' (L1 ₂)-precipitates per analyzed 3-D APT volume
$C_{Al}^{\gamma,eq}(R)$	the equilibrium concentration of Al in the γ (f.c.c.)-phase at the γ/γ' interface of a γ' (L1 ₂)-precipitate	$N_v(t)$	number density per unit volume of γ' (L1 ₂)-precipitates
$C_i^{\gamma,eq}(\infty)$	equilibrium concentration of element i in the γ (f.c.c.)- phase	n	total number of atoms enclosed within an isoconcentration surface
$\langle C_i^{\gamma,ff}(t) \rangle$	ff(far-field) concentration of element i in the γ (f.c.c.)-phase	n_j	number of jumps made by a monovacancy in monovacancy-mediated LKMC ₁ simulation by either an Al or Ni atom
$(C_i^{\gamma,eq}(\infty) - C_i^{\gamma,eq}(\infty))$	the difference between the equilibrium concentrations of the γ' (L1 ₂)- and γ (f.c.c.)-phases	n_{tot}	total number of data points in a distribution
C_{LKMC}^V	monovacancy concentration in LKMC ₁ simulations	p	temporal exponent for $\langle R(t) \rangle$ according to the LS and CVMK models
C_0	initial concentration of the precipitating solute element	Q	activation energy for solute diffusion in a thermally activated process
$D_{coarsening}^{experiment}$	diffusivity determined from 3-D APT coarsening experiments	q	temporal exponent for $N_v(t)$ according to the LS and CVMK models
D_i^{region}	diffusivity of element i ($i = \text{Ni or Al}$) determined in a given region from monovacancy-mediated LKMC ₁ simulations	R	γ' (L1 ₂)-precipitate radius
D_i^{necks}	diffusivity of element i ($i = \text{Ni or Al}$) determined in the necks connecting two γ' (L1 ₂)-precipitates from monovacancy-mediated LKMC ₁ simulations	R^*	critical radius for nucleation
D_i^{region}	diffusivity of element i ($i = \text{Ni or Al}$) determined in the supercell from monovacancy-mediated LKMC ₁ simulations	$\langle R(t) \rangle$	time-dependent mean γ' (L1 ₂)-precipitate radius
D_i^{region}	diffusivity of element i ($i = \text{Ni or Al}$) determined in the γ (f.c.c.)-phase from monovacancy-mediated LKMC ₁ simulations	$\langle R(t_0) \rangle$	mean γ' (L1 ₂)-precipitate radius at the onset of stationary coarsening, which is not in general $t = 0$
$D_i^{\gamma\text{precipitates}}$	diffusivity of element i ($i = \text{Ni or Al}$) determined in the γ' (L1 ₂)-phase from monovacancy-mediated LKMC ₁ simulations	r	temporal exponent for $\Delta C_i^{\gamma}(t)$ according to the LS and CVMK models
\tilde{D}	interdiffusivity of Ni and Al	SS_{res}	sum of square residuals
D_0	diffusivity pre-exponential factor	SS_{tot}	total sum of squares
$E_{sp-p,q}^i$	energy of atom i at the saddle point (sp) between sites p and q	T	temperature in Kelvin
$F(\phi_{\gamma'})$	correction factor applied to the calculation of K to account for a nonzero volume fraction, $\phi_{\gamma'}(t)$	t	aging time
$f(t)$	fraction of γ' (L1 ₂)-precipitates interconnected by necks	t_{LKMC}	monovacancy-mediated LKMC ₁ simulation time
G_m^{γ}	curvature of the Gibbs molar free energy of mixing in the γ (f.c.c.)- phase	t_0	time at which stationary coarsening commences in an alloy
$g(R/\langle R(t) \rangle, t)$	normalized and dimensionless quantity used for the ordinate axis of PSDs	V_a^{γ}	atomic volume of the γ (f.c.c.)- phase
J_{APT}^{st}	stationary nucleation current as measured by APT experiments	$V_a^{\gamma'}$	atomic volume of the γ' (L1 ₂)- phase
J_{CNT}^{st}	stationary nucleation current as calculated by CNT	$V_m^{\gamma'}$	molar volume of the γ' (L1 ₂)-precipitate phase in m^{-3}
$J_{experiment}^{st}$	stationary nucleation current measured experimentally using 3-D APT	W_i^*	critical net reversible work required for the formation of a spherical nucleus containing i atoms
J_{LKMC}^{st}	stationary nucleation current as calculated utilizing monovacancy-mediated LKMC ₁ simulations	$W_{p,q}^{i,v}$	exchange frequency between an atom of type i on a site p and a monovacancy, v , on a NN site q
K	rate constant for $\langle R(t) \rangle$ according to the LS and CVMK models	W_R	reversible work for the formation of a spherical nucleus
$K_i^{\gamma'/\gamma}(t)$	partitioning coefficient of element i between the γ' - and γ -phases	W_R^*	critical net reversible work required for the formation of a critical spheroidal nucleus
K_n	rate constant for $N_v(t)$ in the LS and CVMK models	y_i	measured quantity
		$\langle y \rangle$	mean of all y_i values
		Z	Zeldovich factor
		α	monovacancy jump distance in monovacancy-mediated LKMC ₁ simulations
		β^*	kinetic coefficient describing the rate of condensation of single atoms on the critical nuclei
		$\Delta C_i^{\gamma}(t)$	supersaturation of element i in the γ (f.c.c.)-phase
		$\Delta C_i^{\gamma'}(t)$	supersaturation of element i in the γ' (L1 ₂)-phase
		ΔF_{ch}	chemical energy component of the total Helmholtz free energy of an alloy
		ΔF_{el}	elastic energy component of the total Helmholtz free energy of an alloy

ΔH	change in enthalpy	$\phi_{\gamma'}(t)$	volume fraction of the γ' (L1 ₂)-precipitate phase
ΔH_V^F	enthalpy of formation of a monovacancy	$\phi_{\gamma'}^{eq}$	equilibrium volume fraction of the γ' (L1 ₂)-precipitate phase
ΔS	entropy change		
ΔS_V^F	entropy of formation of a monovacancy	3-D APT	3-D atom-probe tomography
$\delta(t)$	compositional interfacial widths between the γ (f.c.c.)- and γ' (L1 ₂)-phases	AV	Akaiwa-Voorhees precipitate size distribution
ϵ	lattice parameter misfit between the γ (f.c.c.)- and γ' (L1 ₂)-phases	BW	Brailsford-Wynblatt precipitate size distribution
ϵ_{j-j}^k	atom-atom interaction energies	CVMK	Calderon-Voorhees-Murray-Kostorz mean-field diffusion-limited coarsening model
ϵ_{v-i}^k	monovacancy-solute <i>ghost interactions</i> between an atom and a monovacancy in the k th NN shell	CNT	classical nucleation theory
ζ	detection efficiency of the two-dimensional microchannel plate (MCP)	DFT	density functional theory
$\eta_{correlation}^{region,Ni-Al}$	correlation factor for diffusion in dilute Ni-Al system	<i>ff</i>	far-field
κ	rate constant for $\Delta C_i^\gamma(t)$ according to the LS and CVMK models	GCMC	Grand Canonical Monte Carlo
$\langle \lambda_{edge-edge}(t) \rangle$	average minimum edge-to-edge distance between γ' (L1 ₂)-precipitates	ICP-AES	inductively coupled plasma atomic emission spectroscopy
μ_γ	shear modulus of the γ (f.c.c.)-phase	LDA	local-density approximation
v^i	attempt frequency for the exchange between a Ni or Al atom and a monovacancy	LKMC	lattice kinetic Monte Carlo
Ξ	correlation length: the interaction distance over which monovacancy-solute interactions occur	LKMC ₁	LKMC parameters that take into account the monovacancy-solute binding energies out to 4th NN distances
ξ^2	coefficient of determination	LKMC ₂	LKMC parameters that artificially truncate the monovacancy-solute binding beyond the 1st NN, keeping all atomic interactions the same as for LKMC ₁
ρ	atomic number density of the γ' (L1 ₂)-phase	LS	Lifshitz-Slyozov-diffusion-limited mean-field coarsening model
$\sum_{\text{broken bonds}}$	$(n_{ij}^k \epsilon_{i-j}^k + \epsilon_{v-i}^k)$ sum of the atomic interactions over all the bonds that are affected by having atom i and the monovacancy v exchange between sites p and q , respectively	MCP	microchannel plate
σ	one standard deviation from the mean	NN	nearest-neighbor
$\sigma_{\gamma/\gamma'}$	interfacial Gibbs free energy between γ (f.c.c.)- and γ' (L1 ₂)-phases	PSD	precipitate size distribution
τ_j	time for Monte Carlo step j	RTA	residence time algorithm
		TEM	transmission electron microscopy
		TIDC	trans-interface diffusion-controlled coarsening model
		VASP	Vienna <i>ab initio</i> simulation package
		W(Wagner, Carl)	model interface-limited coarsening model

2.	Methodologies	313
2.1.	Processing of specimens	313
2.2.	Micro-indentation measurements	314
2.3.	Three-dimensional atom-probe tomography	314
2.4.	Transmission electron microscopy	314
2.5.	Monovacancy-mediated lattice-kinetic Monte Carlo simulations	314
3.	Results	314
3.1.	Temporal evolution of the Vickers microhardness values	314
3.2.	Temporal evolution of the γ' (L1 ₂) precipitate volume fraction, $\phi_{\gamma'}(t)$, number density, $N_v(t)$, and mean radius $\langle R(t) \rangle$	314
3.3.	Temporal evolution of the compositions of the γ (f.c.c.)- and γ' (L1 ₂)-phases	316
3.4.	Temporal evolution of the γ' (L1 ₂)-precipitate size distributions (PSDs)	317
3.5.	Temporal evolution of the fraction of γ' (L1 ₂)-precipitates interconnected by necks, $f(t)$, and the minimum edge-to-edge distances, $\langle \lambda_{edge-edge}(t) \rangle$, between neighboring γ' (L1 ₂)-precipitates	317
3.6.	Temporal evolution of the interfacial compositional width, $\delta(t)$, between the gamma (f.c.c.)- and gamma-prime (L1 ₂ structure)-phases	318
3.7.	Calculation of four different diffusivities based on monovacancy-mediated lattice-kinetic Monte Carlo simulations	319
3.7.1.	The monovacancy's trajectories in four distinct regions	319
3.7.2.	Calculations of the four different diffusivities D_i^{region}	319
3.7.3.	Four distinct aluminum diffusivities	320
3.7.4.	Four distinct nickel diffusivities	321
3.7.5.	The diffusivities of Ni and Al in the supercell $D_i^{supercell}$	321
4.	Discussion	321
4.1.	Temporal evolution of the Vickers microhardness values	321
4.2.	Temporal evolution of the γ' (L1 ₂ -structure) precipitate volume fraction, $\phi_{\gamma'}(t)$, number density, $N_v(t)$, and mean radius $\langle R(t) \rangle$	321
4.2.1.	Temporal evolution of the volume fraction of γ' (L1 ₂ -structure)-precipitates $\phi_{\gamma'}(t)$	321
4.2.2.	Temporal evolution of the number density of γ' (L1 ₂ structure)-precipitates $N_v(t)$	321
4.2.3.	Temporal evolution of the mean radius, $\langle R(t) \rangle$, of γ' (L1 ₂ structure)-precipitates	323

4.3.	Temporal evolution of the compositions of the γ (f.c.c)- γ' (L1 ₂) structure-phases	323
4.4.	Temporal evolution of the γ' (L1 ₂)-precipitate size distributions (PSDs)	324
4.5.	Temporal evolution of the fraction of γ' (L1 ₂)-precipitates interconnected by necks, $f(t)$, and the minimum edge-to-edge distances, $\langle \lambda_{edge-edge}(t) \rangle$, between neighboring γ' (L1 ₂)-precipitates	324
4.5.1.	The evolution of the fraction of γ' (L1 ₂)-precipitates interconnected by necks $f(t)$	325
4.5.2.	The temporal evolution of the edge-to-edge distances, $\langle \lambda_{edge-edge}(t) \rangle$, between neighboring γ' (L1 ₂)-precipitates, and the flux diffusion mechanism	325
4.6.	Temporal evolution of the compositional interfacial widths, $\delta(t)$, between the γ (f.c.c)- and γ' (L1 ₂)-phases	326
4.6.1.	The temporal evolution of the concentration profiles between the γ (f.c.c)- and γ' (L1 ₂)-phases	326
4.6.2.	The {100}-type compositional interfacial width $\delta(t)$	326
4.7.	The interfacial free energy of the γ (f.c.c)/ γ' (L1 ₂) interface $\sigma^{\gamma/\gamma'}$	327
4.7.1.	The measured interfacial free energy of the γ (f.c.c)/ γ' (L1 ₂) interface determined from coarsening experiments and their comparison with first-principles calculations of $\sigma^{\gamma/\gamma'}$	327
4.7.2.	Equilibrium morphology of γ' (L1 ₂)-precipitates	327
4.8.	Comparison of the diffusivities calculated from atom-probe tomography experimental data and monovacancy-mediated lattice-kinetic Monte Carlo simulation results	327
4.8.1.	Relationship of the interdiffusivity, D , determined by monovacancy-mediated LKMC ₁ simulations and the diffusivity determined from the coarsening experiments $D_{coarsening}^{experiment}$	327
4.8.2.	Calculation of the diffusivity, $D_{coarsening}^{experiment}$, from atom-probe tomography coarsening data and the inter-diffusivity, D , of Al and Ni	328
5.	Summary and conclusions	328
	Acknowledgements	330
	Supplementary data	330
	References	330

1. Introduction

Commercial Ni-based superalloys are used for single-crystal turbine blades in aircraft engines (military and commercial) and land-based natural-gas fired turbine engines because of their high strength, coarsening, creep, oxidation and corrosion resistance, and toughness at elevated temperatures [1–3]. These alloys consist of a disordered Ni-rich matrix (γ (f.c.c)-phase) and coherent ordered Ni₃Al (L1₂-structure) precipitates (γ' (L1₂)-phase). Precipitation strengthening results from the nucleation, growth, and coarsening of the γ' (L1₂)-precipitate phase, though continued coarsening during usage at elevated temperatures will eventually lead to a loss in peak strength. Aluminum and Ti are commonly added to aid in the formation of the L1₂-phase precipitates. Refractory elements with small diffusivities, such as Mo, W, Nb, Ta, Zr, Ru, Re, and Hf, are added to decelerate the coarsening kinetics [1,2]. The primary thermodynamic driving force for coarsening is the minimization of the total interfacial area per unit volume of the γ' (L1₂)-precipitates, which minimizes the total Gibbs free energy because it is the product of the total interfacial area and the interfacial Gibbs free energy, $\sigma^{\gamma/\gamma'}$, between the γ (f.c.c)- and γ' (L1₂)-phases [3–6]. The coarsening rate in a commercial Ni-based superalloy is mainly controlled by: (1) the diffusivities of the alloying elements, which are strongly temperature dependent; (2) $\sigma^{\gamma/\gamma'}$, whose value decreases continuously with increasing temperature; and (3) the elastic stress field interactions among γ' (L1₂)-precipitates [7].

Our prior research has focused primarily on analyzing the nucleation, growth, and coarsening kinetics in ternary Ni-Al-Cr alloys aged at 873 K (600 °C) and quaternary Ni-Al-Cr-W, Ni-Al-Cr-Re, Ni-Al-Cr-Ta, and Ni-Al-Cr-Ru alloys aged at 1073 K (800 °C) [8–31]. The present research concentrates on comparing the temporal evolution and kinetic pathways for phase separation in a binary Ni-12.5 Al at.% alloy aged at 823 K (550 °C). This extensively studied binary Ni-Al alloy should, in principle, be simpler than concentrated multicomponent alloys, but it has some surprising subtleties and complexities that are resolved in this article in great detail and compared with prior

results.

1.1. A short history of the interfacial Gibbs free energy of the $\text{Ni}(\text{f.c.c})/\text{Ni}_3\text{Al}(\text{L1}_2)$ heterophase interface, $\sigma^{\gamma/\gamma'}$

The value of $\sigma^{\gamma/\gamma'}$ can be extracted from experimental coarsening data by determining the rate constants of the mean radius of γ' (L1₂)-precipitates, $\langle R(t) \rangle$, and the supersaturation of solute in the γ (f.c.c)-matrix, $\Delta C_{Al}^{\gamma}(t)$, utilizing one of several existing diffusion-limited mean-field coarsening models. Ardell and Nicholson used the Lifshitz-Slyozov (LS) [32] and the Wagner (W) [33] interface coarsening model and the then available archival diffusivities to estimate $\sigma^{\gamma/\gamma'}$ experimentally, for a Ni-13.5Al at.% alloy aged at 898 K (625 °C), 1023 K (750 °C), and 1048 K (775 °C), to be ~30 mJ m⁻² [34]. Additionally, Ardell used a technique developed by Ben Israel and Fine [35] to measure solute depletion in the γ (f.c.c)-matrix employing the change in the Curie temperature and the rate constant associated with $\langle R(t) \rangle$ for Ni-13.2 Al and Ni-12.9 Al at.% alloys aged at 898 (625 °C) and 988 K (715 °C), respectively, which yielded ~14 mJ m⁻² for $\sigma^{\gamma/\gamma'}$ [36]. Chellman and Ardell used the same methodology to calculate $\sigma^{\gamma/\gamma'}$ for four Ni-Al alloys (Ni-14.1 Al, Ni-15.9 Al, Ni-17.1 Al, and Ni-19.3 Al at.%) aged at 1073 K (800 °C) and obtained ~8 mJ m⁻² [37]. Hirata and Kirkwood used the LS model and archival diffusivities to calculate $\sigma^{\gamma/\gamma'}$ for a Ni-12.3 Al at.% alloy, aged at 943 K (670 °C), 953 (680 °C), 963 K (690 °C), and 968 K (695 °C), to be 17.4, 16.6, 19.8, and 24.3 mJ m⁻², respectively [38]. Marsh and Chen measured the rate constants for $\langle R(t) \rangle$ and the volume fraction of the γ' (L1₂)-phase, $\phi_{\gamma'}(t)$, from coarsening data of a Ni-12.5 Al at.% alloy aged at 823 K (550 °C), 873 K (600 °C), 923 K (650 °C), and 973 K (700 °C) to obtain $\sigma^{\gamma/\gamma'}$ values of 16.9, 21.7, 16.6, and 10.3 mJ m⁻², respectively [39]. Calderon, Voorhees, Murray, and Kostorz (CVMK) determined the $\langle R(t) \rangle$ rate constant from the coarsening data for a Ni-12.8 Al at.% alloy aged at 848 K (575 °C) and 863 K (590 °C) using a modified LS model that takes into account the thermodynamics of the γ (f.c.c)-phase for the very first time [40]; they obtained a $\sigma^{\gamma/\gamma'}$ value of ~40–80 mJ m⁻² based on an early approximate thermodynamic database for the γ (f.c.c)-matrix-phase. These large differences in $\sigma^{\gamma/\gamma'}$ were

Table 1

Summary of prior studies conducted to determine the interfacial free energy, $\sigma_{\gamma/\gamma'}$, between the γ (f.c.c.) and γ' (L1₂)-phases. All the values are displayed graphically in Fig. 1.

Composition (at.%)	Aging Temp. (K)	$\sigma_{\gamma/\gamma'} (\text{mJ m}^{-2})$	Method	Reference
Ni-13.5 Al	898	31.2	Electron microscopy	[34]
Ni-13.5 Al	1023	27.2	"	[34]
Ni-13.5 Al	1048	32.3	"	[34]
Ni-13.1 Al	898	14.4	Ferromagnetic Curie temperature measurements	[36]
Ni-12.8 Al	988	14.2	"	[36]
Ni-14.1 Al	1073	6.2	Magnetic analysis and TEM	[37]
Ni-15.9 Al	1073	8.9	"	[37]
Ni-17.7 Al	1073	11.9	"	[37]
Ni-19.3 Al	1073	8.3	"	[37]
Ni-12.3 Al	943	17.4	Electron microscopy	[38]
Ni-12.3 Al	953	16.6	"	[38]
Ni-12.3 Al	963	19.8	"	[38]
Ni-12.3 Al	968	24.3	"	[38]
Ni-14 Al	823	19	Atom-probe field ion microscopy	[146]
Ni-12.5 Al	823	16.9	X-ray diffraction	[39]
Ni-12.5 Al	873	21.7	"	[39]
Ni-12.5 Al	923	16.6	"	[39]
Ni-12.5 Al	973	10.3	"	[39]
Ni-12 Al	773	14	High resolution TEM	[121]
Ni-12.8 Al	848	42 ± 2	Small angle neutron scattering and TEM	[40]
Ni-12.8 Al	863	$68 \pm 6, 80 \pm 8$	"	[40]
Ni-13.1 Al	898	8.2	Reanalysis of [36]	[41]
Ni-12.8 Al	988	8.0	Reanalysis of [36]	[41]
Ni-12.5 Al	823	8.7	Reanalysis of [39]	[41]
Ni-12.5 Al	873	8.6	Reanalysis of [39]	[41]
Ni-12.5 Al	923	3.0	Reanalysis of [39]	[41]
Ni-12.5 Al	973	0.9	Reanalysis of [39]	[41]
Ni-12.86 Al	898	4.29 ± 0.35	Reanalysis of [147]	[137]
Ni-12.86 Al	988	3.71 ± 0.74	Reanalysis of [147]	[137]
Ni-13.1 Al	898	22.33 ± 1.31	Reanalysis of [36]	[42]
Ni-12.8 Al	988	19.52 ± 0.90	Reanalysis of [36]	[42]

attributed to the measurements being performed at different temperatures, because $\sigma_{\gamma/\gamma'}$ is temperature dependent [40]. Next, Ardell used a non-ideal solution value for the curvature of the molar Gibbs free energy of mixing of the γ (f.c.c.)-phase, G_m^γ , from Calderon et al.'s research to reanalyze his prior results [36] and obtained an estimate of $\sim 8 \text{ mJ m}^{-2}$ for $\sigma_{\gamma/\gamma'}$ at 898 K (625 °C) to 973 K (700 °C) [41]. More recently, Ardell employed his trans-interface diffusion-controlled (TIDC) coarsening model to reanalyze his earlier results and obtained a value of $\sim 20 \text{ mJ m}^{-2}$ for $\sigma_{\gamma/\gamma'}$ at 898 K (625 °C) and 988 K (715°) [42]. A summary of all the previously determined experimental $\sigma_{\gamma/\gamma'}$ values for different binary Ni-Al alloys aged at different temperatures is listed in Table 1 and also displayed graphically in Fig. 1.

In contrast, there exist substantially fewer theoretical results for values of $\sigma_{\gamma/\gamma'}$ than experimental ones. Price and Cooper used density functional theory (DFT) to calculate $\sigma_{\gamma/\gamma'}$ and compared the effect of either including or ignoring spin-polarization on $\sigma_{\gamma/\gamma'}$ for a {100}-type interface [43]. They found that $\sigma_{\gamma/\gamma'}$ ranges from 63 mJ m^{-2} when spin-polarization is included to 25 mJ m^{-2} when it is ignored. Mishin used an embedded-atom-method potential, which he developed, to calculate values of $\sigma_{\gamma/\gamma'}$ for interfaces parallel to the {100}-, {110}-, and {111}-type planes as a function of supercell size [44], which yielded $\sigma_{\gamma/\gamma'}$ values of 46, 28, and 12 mJ m^{-2} for the {100}, {110}, and {111} planes, respectively, at 700 K. Mao et al. used first-principles calculations, including ferromagnetism and vibrational entropy, and Monte Carlo simulations to study the γ (f.c.c.)/ γ' (L1₂) interface parallel to the {100}-, {110}-, and {111}-type planes as a function of temperature [45]. They found a linear decrease in $\sigma_{\gamma/\gamma'}$ from 0 to 1100 K (827 °C) for each {hkl}-type interface. Woodward et al. also used first-principles calculations to study the γ (f.c.c.)/ γ' (L1₂) interface parallel to the {100}-, {110}-, and {111}-type planes as a function of temperature [46]. They observed a non-linear decrease in $\sigma_{\gamma/\gamma'}$ from 1300 K

(1027 °C) to 0 K, which varied with {hkl}-type plane and asymptotically approached $\sim 10 \text{ mJ m}^{-2}$ above 600 K (323 °C) for each {hkl}-type interface. Next, Mishin utilized the capillary fluctuation methodology to calculate $\sigma_{\gamma/\gamma'}$ for the {100}-type planes as a function of temperature and obtained a value of 14 mJ m^{-2} at 800 K (527 °C) [47]. A summary of all the theoretical/computationally determined $\sigma_{\gamma/\gamma'}$ values for binary Ni-Al alloys is presented in Table 2. Aluminum has a non-zero size effect in Ni, which differs from that of Ni₃Al, and hence there exists a dependence of the precipitate energy on precipitate radius, which is non-trivial even in the absence of precipitate-precipitate interactions: Section 4.2.2.1.

1.2. The mean-field coarsening models

1.2.1. Lifshitz-Slyozov (LS) mean-field model for diffusion-limited coarsening

The LS model for a binary alloy assumes: (i) no elastic interactions among γ' (L1₂)-precipitates, thereby limiting $\phi_{\gamma'}(t)$ to zero; (ii) γ' (L1₂)-precipitates have a spherical morphology; (iii) coarsening occurs in a stress-free matrix; (iv) the γ' (L1₂)-precipitate diffusion fields do not overlap; (v) dilute solid-solution theory obtains in the γ (f.c.c.)-matrix; (vi) the linearized version of the Gibbs-Thomson equation obtains; (vii) coarsening is diffusion-controlled and occurs by the classical evaporation-condensation (*the big eat the small*) mechanism; and (viii) γ' (L1₂)-precipitates coarsen with a fixed chemical composition, which is 100% solute. These assumptions are highly restrictive and extremely difficult to obtain experimentally. And yet little experimental evidence (in systems where $\phi_{\gamma'}(t)$ is greater than zero) exists to support the prediction of the LS temporal dependency of $\langle R(t) \rangle$. The experimental γ' (L1₂)-precipitate size distributions (PSDs) are consistently broader, flatter, and more symmetric than what the mean-field LS

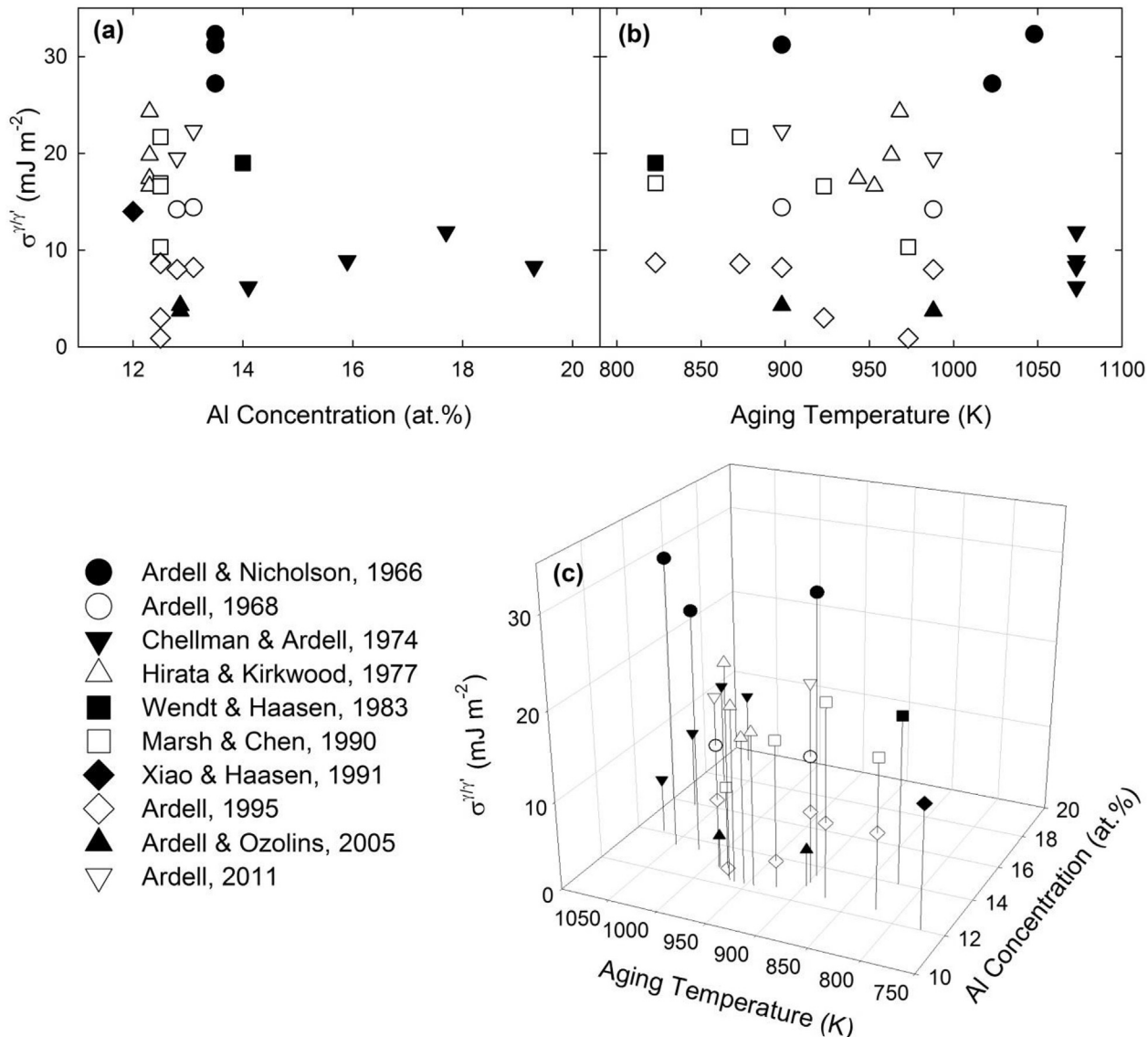


Fig. 1. Summary of prior values determined for the interfacial free energy, $\sigma_{\gamma/\gamma'}$, between the γ (f.c.c.) and γ' (L1₂)-phases as a function of Al concentration and aging temperature. The values are also displayed in tabular form in Table 1.

Table 2

Summary of computationally determined values of $\sigma_{\gamma/\gamma'}$ (mJ m^{-2}) for the {100}-, {110}-, and {111}-type planes for the $\gamma(\text{Ni})/\gamma'(\text{Ni}_3\text{Al})$ interface in Ni-Al alloys.

Method	Temperature (K)	{100}	{110}	{111}	Reference
Density functional theory	0	63	—	—	[43]
Embedded atom method	700	46	28	12	[44]
First-principles calculations	823 ^a	23.11	26.83	28.42	[45]
First-principles calculations	823	16.5	17.7	15.9	[46]
Capillary fluctuation method	800	14	—	—	[47]

^a In reference [45] $\sigma_{\gamma/\gamma'}$ is determined as a function of [hkl], for temperatures between 0 and 1100 K, plus the effects of coherency strain, phonon vibrational entropy, and ferromagnetism are included, which makes this the most complete study to date.

model predicts [48–53]. Hence, the LS PSD is generally agreed to be incorrect, as is probably the modified LS PSD [54]. A more realistic approach, which is dependent on $\phi_{\gamma}(t)$, was developed by Brailsford and Wynblatt (BW) [55]. Akaiwa and Voorhees (AV) used a numerical solution to the multi-particle diffusion problem to model PSDs during the later stages of coarsening, when $\phi_{\gamma}(t)$ is close to its equilibrium value [56]. Additionally, Marsh and Glicksman (MG) developed a model that treats γ' (L1₂)-precipitates as an equivalent distribution of field cells, each of which is analyzed using a diffusion

field [57]. The LS, BW, AV, and MG diffusion-limited coarsening models all assume that γ' (L1₂)-precipitates have a spherical morphology.

The LS model for a binary alloy, subject to the above assumptions, yields the following relationships for: (1) $\langle R(t) \rangle$; (2) the number density per unit volume of γ' (L1₂)-precipitates, $N_{\nu}(t)$; and (3) the supersaturation of element i , $\Delta C_i^{\gamma}(t)$:

$$\langle R(t) \rangle^p - \langle R(t_0) \rangle^p = K(t - t_0) \quad (1)$$

$$N_v(t)^q = K_n(t - t_0) \quad (2)$$

$$\Delta C_i^\gamma(t) = \langle C_i^{\gamma,ff}(t) \rangle - C_i^{\gamma,eq}(\infty) = \kappa(t - t_0)^{-1/r} \quad (3)$$

where $\langle R(t_0) \rangle$ is the mean $\gamma'(\text{L1}_2)$ -precipitate radius at the onset of quasi-stationary coarsening at time t_0 ; $\Delta C_i^\gamma(t)$ is the difference between the far-field (*ff*) matrix concentration of component i , $\langle C_i^{\gamma,ff}(t) \rangle$, and the equilibrium concentration of component i , $C_i^{\gamma,eq}(\infty)$; and where K , K_n , and κ are the associated rate constants. In the diffusion-limited LS model the temporal exponents p , q , and r are 3, -1, and 3, respectively. In our analyses we take p , q , and r to be *unknown constants*, which are determined from 3-D atom-probe tomography (APT) data and monovacancy mediated lattice-kinetic Monte Carlo (LKMC₁) simulations, utilizing a nonlinear multivariate regression methodology for analyzing the data [58], **Supplement A**. If p , q , and r are not equal to 3, -1, and 3, then the values of K , K_n , and κ are dimensionally incorrect, which is not a generally appreciated fact.

1.2.2. Calderon-Voorhees-Murray-Kostorz (CVMK) model for diffusion-limited mean-field coarsening

CVMK developed a diffusion-limited mean-field coarsening model for binary alloys that: (1) incorporates a nonzero value of $\phi_{\gamma'}(t)$; (2) permits a nonzero solubility of the solute species i in the $\gamma(\text{f.c.c.})$ -matrix; and (3) incorporates non-ideal solution thermodynamics for the $\gamma(\text{f.c.c.})$ -matrix [40]. The CVMK model utilizes a capillary length, l^γ , for the $\gamma(\text{f.c.c.})$ -phase:

$$l^\gamma = \frac{2V_m^\gamma \sigma^{\gamma/\gamma'}}{(C_i^{\gamma,eq}(\infty) - C_i^{\gamma,eq}(\infty)) G_m^\gamma} \quad (4)$$

where V_m^γ is the molar volume of the solute in the $\gamma'(\text{L1}_2)$ -precipitate phase; and $(C_i^{\gamma,eq}(\infty) - C_i^{\gamma,eq}(\infty))$ is the difference between the equilibrium concentrations of element i in the $\gamma'(\text{L1}_2)$ - and $\gamma(\text{f.c.c.})$ -phases, respectively. This approach permitted CVMK to rewrite K , and κ^γ (the value of κ is measured in the $\gamma(\text{f.c.c.})$ -phase) utilizing Eqs. (1) and (3) in terms of l^γ and the diffusivity, $D_{\text{experiment}}^{\text{coarsening}}$, obtained from coarsening experiments:

$$K = \frac{4D_{\text{experiment}}^{\text{coarsening}} l^\gamma F(\phi_{\gamma'})}{9(C_i^{\gamma,eq}(\infty) - C_i^{\gamma,eq}(\infty))} \quad (5)$$

$$\kappa^\gamma = \left(\frac{4D_{\text{experiment}}^{\text{coarsening}}}{9(l^\gamma)^2 (C_i^{\gamma,eq}(\infty) - C_i^{\gamma,eq}(\infty))} \right)^{-1/3} \quad (6)$$

where $F(\phi_{\gamma'})$ is a correction factor that includes the effect of a nonzero value of $\phi_{\gamma'}(t)$, which is calculated numerically [40,59]. The CVMK model does not provide a corresponding correction factor for κ^γ .

Following the CVMK coarsening model, the $\gamma'(\text{L1}_2)$ -precipitates nucleate initially from the $\gamma(\text{f.c.c.})$ -matrix as spheroids, which subsequently grow and coarsen temporally. The $\gamma'(\text{L1}_2)$ -precipitates in a Ni-12.5 Al at.% alloy aged at 823 K (550 °C) follow four distinct regimes of phase separation (or phase decomposition or precipitation): (I) quasi-stationary $\gamma'(\text{L1}_2)$ -precipitate nucleation; (II) concomitant $\gamma'(\text{L1}_2)$ -precipitate nucleation and growth; (III) concurrent growth and coarsening via the coagulation and coalescence mechanism as opposed to the classic evaporation-

condensation (“the big eat the small”) mechanism; and (IV) quasi-stationary coarsening of $\gamma'(\text{L1}_2)$ -precipitates. During the nucleation and growth stages of the aging process, coagulation and coalescence of $\gamma'(\text{L1}_2)$ -precipitates (a phenomenon often ignored in mean-field coarsening models [60]) plays a significant role in the coarsening of $\gamma'(\text{L1}_2)$ -precipitates in Ni-Al and Ni-Al-Cr alloys. Coagulation and coalescence occurs when an L1_2 partially-ordered neck forms between two adjacent $\gamma'(\text{L1}_2)$ -precipitates. Mao et al. performed a correlative 3-D APT study and monovacancy-mediated LKMC₁ simulations to determine the role of the diffusion mechanism on precipitation in three different Ni-Al-Cr alloys aged at 873 K (600 °C), for times ranging from 0.17 to 4096 h [61,62]. Their studies demonstrate that coagulation and coalescence is a consequence of overlapping nonequilibrium concentration profiles surrounding the $\gamma'(\text{L1}_2)$ -precipitates, which yield *initially nonequilibrium diffuse interfaces: that is, non-atomically sharp. These diffuse interfaces are energetically unfavorable, leading to the coagulation and coalescence of two adjacent $\gamma'(\text{L1}_2)$ -precipitates, and the complete disappearance of the necks with increasing aging times*. At later aging times, coagulation and coalescence is less prevalent because $N_v(t)$ is continuously decreasing and concomitantly the edge-to-edge distance between $\gamma'(\text{L1}_2)$ -precipitates is continuously increasing, and coarsening is then dominated by the classical evaporation-condensation mechanism (*the big eat the small*), which also occurs during nucleation, regime I (Sections 3.2 and 4.2), when $N_v(t)$ is rapidly increasing and $\langle R(t) \rangle$ is approximately constant. At long aging times $N_v(t)$ decreases to a value at which the diffusion fields of the $\gamma'(\text{L1}_2)$ -precipitates are no longer overlapping. Also observed in the Ni-Al-Cr alloys is the beginning of a transition, at aging times >1000 h, of the $\gamma'(\text{L1}_2)$ -precipitates, from a spheroidal-to-a-cuboidal morphology, and the alignment of the $\gamma'(\text{L1}_2)$ -precipitates along a <100>-type direction to minimize elastic strain energy [34,63–65], which is a phenomenon commonly called rafting [66]. The small elastic strain energy in a Ni-12.5 Al at.% alloy is caused by a lattice parameter misfit at 823 K (550 °C) between the $\gamma(\text{f.c.c.})$ -matrix (lattice parameter = 3.58 Å) and the $\gamma'(\text{L1}_2)$ -precipitates (lattice parameter = 3.59 Å), yielding a fractional value of 0.003 ± 0.001 for the lattice parameter misfit [67].

1.3. A new methodology for calculating the interfacial Gibbs free energy of the Ni(f.c.c.)/Ni₃Al(L1₂) interface $\sigma^{\gamma/\gamma'}$

Ardell [41] utilized the CVMK mean-field coarsening model [40], to develop a new approach for calculating $\sigma^{\gamma/\gamma'}$ from two of the three rate constants for a binary alloy by demonstrating that l^γ can be rewritten in terms of K and κ^γ , by combining Eqs. (5) and (6):

$$l^\gamma = K^{1/3} \kappa^\gamma F(\phi_{\gamma'})^{-1/3} \quad (7)$$

Combining Eqs. (4) and (7) yields an expression for $\sigma^{\gamma/\gamma'}$ that is independent of $D_{\text{experiment}}^{\text{coarsening}}$:

$$\begin{aligned} \sigma^{\gamma/\gamma'} &= \frac{l^\gamma (C_i^{\gamma,eq}(\infty) - C_i^{\gamma,eq}(\infty)) G_m^\gamma}{2V_m^\gamma} \\ &= \frac{K^{1/3} \kappa^\gamma F(\phi_{\gamma'})^{-1/3} (C_i^{\gamma,eq}(\infty) - C_i^{\gamma,eq}(\infty)) G_m^\gamma}{2V_m^\gamma} \end{aligned} \quad (8)$$

This approach yields more accurate values for $\sigma^{\gamma/\gamma'}$ than those obtained using an archival value of D , which was the main approach employed prior to Ardell's model, which permits $\sigma^{\gamma/\gamma'}$ to be calculated *independent of* $D_{\text{experiment}}^{\text{coarsening}}$. Once l^γ is determined, $D_{\text{experiment}}^{\text{coarsening}}$ is then calculated by combining Eqs. (5) and (6) to yield:

$$D_{\text{coarsening}}^{\text{experiment}} = \frac{9K^{2/3} (C_i^{\gamma,\text{eq}}(\infty) - C_i^{\gamma,\text{eq}}(0))}{4\kappa\gamma F(\phi_{\gamma})^{2/3}} \quad (9)$$

All the values of $\sigma^{\gamma/\gamma'}$ we calculate employ Eq. (8), which takes into account the effect of $\phi_{\gamma}(t)$ on K and are independent of $D_{\text{coarsening}}$, which is calculated using Eq. (9). We demonstrate unequivocally, Section 4.8, that $D_{\text{coarsening}}$ is equal to the interdiffusivity of Ni and Al, \bar{D} . In this work, all experimental determined values of $\sigma^{\gamma/\gamma'}$ are in a disagreement with the approach Ardell's used (1995) because they utilized a value of a diffusivity from the archival literature, rather than determining both values independently of one another.

1.4. Overview of our current research

In our research, a Ni-12.5 Al at.% alloy aged at 823 K (550 °C) is studied utilizing Vickers microhardness measurements, 3-D APT, monovacancy-mediated LKMC₁ simulations, and some transmission electron microscopy (TEM). Our research focuses strongly on analyzing: (1) Vickers microhardness of the alloy; (2) $\gamma'(\text{L1}_2)$ -precipitate morphology; (3) $\gamma'(\text{L1}_2)$ -precipitate volume fraction, $\phi_{\gamma}(t)$; (4) $\gamma'(\text{L1}_2)$ -precipitate number density, $N_v(t)$; (5) mean radius of $\gamma'(\text{L1}_2)$ -precipitates, $\langle R(t) \rangle$; (6) Al concentration of the $\gamma(\text{f.c.c.})$ -phase, $C_{\text{Al}}^{\gamma}(t)$; (7) Al concentration of the $\gamma'(\text{L1}_2)$ -phase, $C_{\text{Al}}^{\gamma'}(t)$; (8) supersaturation of Al in the $\gamma(\text{f.c.c.})$ -phase, $\Delta C_{\text{Al}}^{\gamma}(t)$; (9) supersaturation of Al in the $\gamma'(\text{L1}_2)$ -phase, $\Delta C_{\text{Al}}^{\gamma'}(t)$; (10) partitioning coefficient of Al, $K_{\text{Al}}^{\gamma'/\gamma}(t)$, between the two phases; (11) partitioning coefficient of Ni, $K_{\text{Ni}}^{\gamma'/\gamma}(t)$, between the two-phases; (12) $\gamma'(\text{L1}_2)$ -precipitate PSDs; (13) fraction of $\gamma'(\text{L1}_2)$ -precipitates interconnected by necks, $f(t)$; (14) average minimum edge-to-edge distance between $\gamma'(\text{L1}_2)$ -precipitates, $\langle \lambda_{\text{edge-edge}}(t) \rangle$; and (15) interfacial compositional widths between the $\gamma(\text{f.c.c.})$ - and $\gamma'(\text{L1}_2)$ -phases, $\delta(t)$. Monovacancy-mediated LKMC₁ simulations of these

15 quantities are compared to all the experimental 3-D APT results.

This study constitutes the most complete and detailed investigation of the temporal evolution of the nanostructure and chemical compositions of a first-order phase transformation in any metallic two-phase alloy made to date. While there exists considerable data quantifying phase separation (or phase decomposition or precipitation) in Ni-Al alloys for an Al concentration that is in the [$\gamma(\text{f.c.c.})$] plus $\gamma'(\text{L1}_2)$] phase field, most research has focused on either the early regimes (nucleation and growth) or the later regimes (growth and coarsening), but not the four regimes. Additionally, while a prior study also focused on measurements of $\langle R(t) \rangle$ and $C_{\text{Al}}^{\gamma}(t)$, these measurements were taken from different experiments [36].

3-D APT allows us to derive all the quantities listed above (with the exception of the Vickers microhardness) from only 3-D APT experiments for each aging time, implying that our data is completely self-consistent. We further demonstrate that the monovacancy-mediated LKMC₁ simulations (Section 2.5) are in excellent agreement with the experimental 3-D APT results, which provide extremely valuable physical insights into the origin of $\delta(t)$. The latter has been a subject of recent great interest.

2. Methodologies

2.1. Processing of specimens

High-purity Ni and Al were vacuum induction melted under a small partial pressure of argon and chill cast in a 19 mm diameter copper mold to form a polycrystalline master ingot with a target composition of Ni-12.5 Al at %. The composition of the ingot was determined to be $\text{Ni-12.5} \pm 0.1$ Al at %, utilizing inductively-coupled plasma atomic-emission spectroscopy (ICP-AES). Samples from the master ingot underwent a three-stage heat treatment. The first stage was homogenization in the $\gamma(\text{f.c.c.})$ -phase field in vacuum at 1573 K (1300 °C) for 20 h. The second stage was a vacancy anneal in the $\gamma(\text{f.c.c.})$ -phase field in vacuum/argon at 1223 K (950 °C) for 3 h,

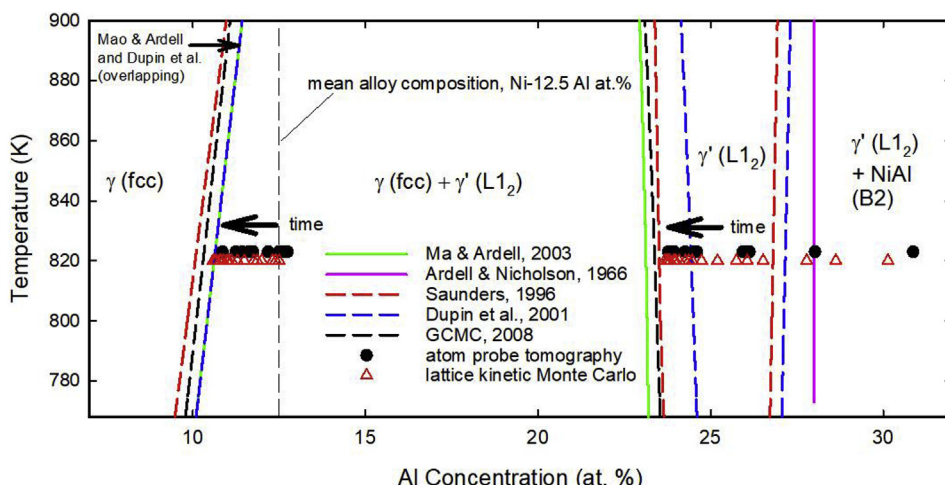


Fig. 2. The overall composition of the alloy, 12.5 at.% Al, is indicated by a vertical dashed-line in the pertinent portion of the Ni-Al phase diagram. On the left-hand side, the solvus curves are displayed for calculations performed using Saunders's [68] (dot-dashed green-curve), quasi-grand canonical Monte Carlo (GCMC) simulation (dashed black-curve) [22], Dupin et al.'s thermodynamic databases (purple dotted-curve) [70], employing Thermo-Calc [69], and Ma and Ardell's (solid blue-curve) experimental curve. Dupin et al.'s $\gamma(\text{f.c.c.})$ / (f.c.c.) plus $\gamma'(\text{L1}_2)$) solvus curve (purple dotted-curve) overlaps with Ma's and Ardell's γ/γ plus γ' solvus curve (solid blue-curve) [71]. On the right-hand side, the solvus curves are as follows: solid-blue curve, Ma and Ardell [71]; the dashed black-curve, GCMC simulation [22]; dot-dashed green-curve, Saunders [68]; purple dotted-curve, Dupin [70]; and dashed red-curve on the extreme right-hand side, Ardell and Nicholson [34]. The $(\gamma$ plus $\gamma')$ / γ' solvus curves due to Ma and Ardell, GCMC simulation, and Saunders overlap approximately, while Dupin's solvus curve is significantly to the right of those three solvus curves. The $\gamma/\gamma'(\text{L1}_2)$ plus NiAl(B2) structure phase field lies to the right of the dashed red-curve. Note that both the APT and LKMC simulations indicate that nucleation of a second-phase occurs in this phase field. While synchrotron x-ray diffraction studies were unable to differentiate between these two structures at the shortest aging time. Also note the large supersaturation of Al in the $\gamma'(\text{L1}_2)$ -precipitate-phase. The horizontal heavy black arrows, pointing to the left, indicate the direction in which the compositions of the $\gamma(\text{f.c.c.})$ - and $\gamma'(\text{L1}_2)$ -phases are temporally evolving. The 3-D APT and LKMC₁ results are offset for clarity, but they represent data for the same aging temperature, 823 K (550 °C). (For interpretation of the references to colour in this figure legend, the reader is referred to the Web version of this article.)

followed by a direct drop-quench into water. The latter temperature was chosen to be above the γ (f.c.c.)/ γ' (L1₂) solvus temperature, which was calculated to be 1180 K (907 °C), utilizing Saunders's thermodynamic database [68] in Thermo-Calc [69]. The final stage was an aging anneal in the [γ (f.c.c.) plus γ' (L1₂)-phase field] at 823 K (550 °C) under flowing Ar for times ranging from 0.08 to 4096 h, followed by an ice-brine water-quench. Fig. 2 displays a partial Ni-Al phase diagram as determined experimentally by Ma and Ardell, Ardell and Nicholson, simulations using two different databases in Thermo-Calc, and our grand canonical Monte Carlo (GCMC) simulations [22,34,68–71]. The average composition of the alloy, Ni-12.5 Al at.%, is indicated by a vertical dashed line. The compositional trajectories of the γ (f.c.c.)- and γ' (L1₂)-phases are indicated by two horizontal heavy black arrows, Sections 3.3 and 4.3.

2.2. Micro-indentation measurements

Vickers microhardness measurements were conducted on specimens aged from 0.08 to 2607 h, utilizing a Struers Duramin-5 microhardness tester with an applied load of 300 g for 5 s at ambient temperature across a flat area of a bulk sample. The samples were prepared by hot mounting at 180 °C, followed by grinding using 2400 grit SiC paper, and then polished to a 1 μm finish using an alumina solution. At least 16 separate indentation measurements were averaged for each aging time.

2.3. Three-dimensional atom-probe tomography

This research was performed utilizing a pulsed-laser 3-D APT (a LEAP 4000X Si tomograph [72–82], employing a picosecond ultraviolet (UV) laser (wavelength = 355 nm), at a target detection rate of 0.05 ions pulse⁻¹, a specimen temperature of 40.0 ± 0.3 K, a pulse repetition rate of 200 kHz, and an ambient gauge pressure of $<6.7 \times 10^{-8}$ Pa. A UV laser energy of 5 pJ pulse⁻¹ was determined to be the optimum value for this Ni-12.5 Al at.% alloy [83]. These experimental conditions were optimized to provide the highest possible compositional accuracy. 3-D APT data were analyzed utilizing the program IVAS 3.6 (Cameca Instruments, Madison, Wisconsin). The γ (f.c.c.)-matrix/ γ' (L1₂)-precipitate heterophase interfaces were delineated with Al iso-concentration surfaces utilizing the inflection-point technique [13], and compositional information was obtained using the proximity histogram methodology [84,85]. The overall composition of each dataset was found to vary slightly from those given by ICP-AES testing, ± 0.5 at.%, especially at longer aging times. Additionally, preferential evaporation of Ni was observed. To account for these variations, the overall composition of each data set was normalized to the ICP-AES

composition measurement based on the measured value of $\phi_{\gamma'}(t)$. **Supplement B.** The standard errors for all quantities are calculated based on counting statistics and represent two standard deviations from the mean value [86]. A solutionized specimen ($t = 0$) was analyzed by 3-D APT to establish whether or not γ' (L1₂)-precipitates were present in the initial quenched-in state, and none were detected: thus, $\phi_{\gamma'}(t = 0) = 0$. Additional details of the procedures are given elsewhere [18,23,30].

2.4. Transmission electron microscopy

Conventional TEM specimens were prepared from standard 3 mm diam. discs. The 500 μm thick discs were ground mechanically to a thickness of ~100 μm. These discs were electropolished utilizing a Struers Tenupol-5 double-jet electropolisher operating at 21 Vdc at a temperature of 253 K (−20 °C), using liquid nitrogen as a coolant. The electrolyte consisted of 8 vol% perchloric acid and 14 vol% 2-butoxyethanol in 78 vol% methanol. Conventional TEM investigations were performed employing a Hitachi HT-7700 instrument operating at 120 kV, utilizing a double-tilt sample holder. The ordered γ' (L1₂)-precipitates were imaged employing a centered dark-field condition utilizing a superlattice reflection of the ordered L1₂-structure of the γ' (L1₂)-phase.

2.5. Monovacancy-mediated lattice-kinetic Monte Carlo simulations

The detail methodology for monovacancy-mediated LKMC₁ simulations can be found in **Supplement C**.

3. Results

3.1. Temporal evolution of the Vickers microhardness values

The temporal evolution of the Vickers microhardness values for Ni-12.5 Al at.% aged for 0.08–2607 h at 823 K (550 °C) is displayed in Fig. 3. The value of the Vickers microhardness remains fairly constant for <4 h of aging, where the alloy is in the nucleation and nucleation plus growth regimes, regimes I and II (Sections 3.2 and 4.2). After the initiation of regime III (growth and coarsening) the Vickers microhardness proceeds to increase continuously as the alloy enters the quasi-stationary coarsening regime, IV, through 1024 h. This indicates that the increase in $\phi_{\gamma'}(t)$ is responsible for the increase of the Vickers microhardness, Section 3.2. The Vickers microhardness achieves a maximum value (peak hardness) of 247 ± 11 at 1024 h and then decreases to 233 ± 5 at 2607 h, which is commonly referred to as over aging.

3.2. Temporal evolution of the γ' (L1₂) precipitate volume fraction, $\phi_{\gamma'}(t)$, number density, $N_v(t)$, and mean radius ($R(t)$)

The temporal evolution of the γ' (L1₂)-precipitate morphology, presented in $50 \times 50 \times 100$ nm³ 3-D APT reconstructions, of the alloy aged for 0.25, 1, 256, 1024, 2607, and 4096 h is displayed in Fig. 4a–f. Spheroidal γ' (L1₂)-precipitates are detected commencing at the earliest aging time [$\langle R(t = 0.08h) \rangle = 0.79 \pm 0.20$ nm], which grow and coarsen temporally to $\langle R(t = 4096h) \rangle = 14.59 \pm 1.62$ nm, where they have a cuboidal morphology, faceted on {100}-type planes. The corresponding increase in $\langle R(t) \rangle$ is a factor of 18.47. The γ' (L1₂)-precipitates at 256 h [$\langle R(t = 256h) \rangle = 5.65 \pm 0.22$ nm, Fig. 4c] are still spheroidal in morphology, while γ' (L1₂)-precipitates at 1024 h [$\langle R(t = 1024h) \rangle = 9.43 \pm 0.65$ nm, Fig. 4d], are undergoing the spheroidal-to-cuboidal morphological transition to minimize elastic strain energy, which is commonly observed in Ni-Al alloys [20,34,63,64,87].

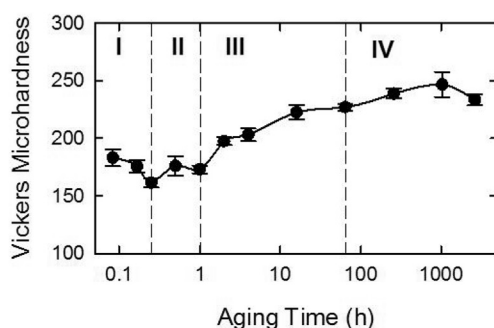


Fig. 3. The temporal evolution of the Vickers microhardness of the Ni-12.5 Al at.% alloy aged at 823 K (550 °C). The increase in Vickers microhardness is consistent with the increase in volume fraction of the γ' (L1₂)-phase, Fig. 5a.

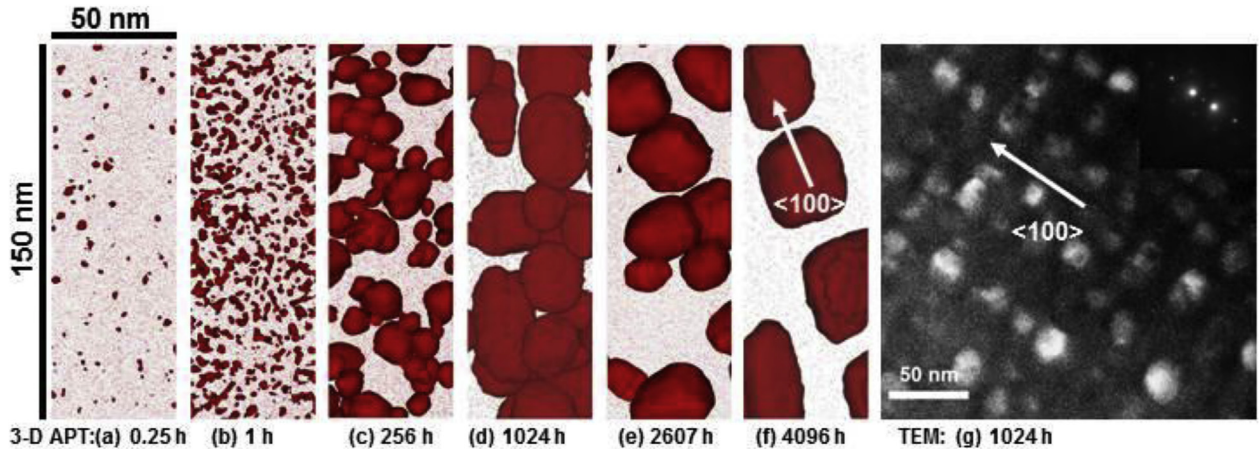


Fig. 4. A display of 3-D-APT reconstructions of a Ni-12.5 Al at. % alloy aged for: (a) 0.25 h; (b) 1; (c) 256; (d) 1024; (e) 2607; (f) 4096 h at 823 K (550 °C), and a dark-field TEM micrograph of a specimen aged for 1024 h at 823 K (550 °C); and (g) The γ' (L₁₂)-precipitates are indicated by red Al iso-concentration surfaces. The value of the Al iso-concentration surface was determined for each dataset using the inflection point method [13]. Aluminum atoms are represented by red dots, while the Ni atoms are omitted for clarity. The γ' (L₁₂)-precipitate number density is increasing in the nucleation regime, (a) and (b). $\langle R(t) \rangle$ increases and $N_v(t)$ decreases beyond 1 h due to growth and coarsening, (c)–(f). The γ' (L₁₂)-precipitates nucleate and grow as spheroids, (a), (b), and (c). In (d) they commence becoming faceted cuboids on the <100>-type planes as a result of a spheroid-to-cuboid transformation. Finally, in (e) and (f) they complete the transformation to cuboids, which are aligned along a <100>-type direction due to elastic interactions, which is commonly called rafting. (For interpretation of the references to colour in this figure legend, the reader is referred to the Web version of this article.)

Some of the γ' (L₁₂)-precipitates at 1024 h, Fig. 4d, are spheroidal, while others are already cuboids once the radii of the precipitates become larger. At 2607 h [$\langle R(t = 2076h) \rangle = 10.72 \pm 0.87$ nm, Fig. 4e] all the visible γ' (L₁₂)-precipitates are cuboidal, and at 4096 h, the γ' (L₁₂)-precipitates have a cuboidal morphology and are aligned along a <100>-type direction, Fig. 4f, which is called rafting [66]. Fig. 4g is a dark-field TEM micrograph for an aging time of 1024 h, which can be directly compared to the 3-D APT results in Fig. 4d. The γ' (L₁₂)-precipitates, displayed in the white against the black γ (f.c.c.)-matrix background, are aligned along a <100>-type direction, which is less obvious in Fig. 4d because 3-D APT reconstructions have a smaller field-of-view than TEM micrographs. The better spatial resolution of the 3-D APT reconstructions demonstrates, however, that all the γ' (L₁₂)-precipitates are not yet cuboids at 1024 h once the radii of the precipitates become larger, which Fig. 4g does not indicate well. The value of $\langle R(t = 1024h) \rangle$ obtained by TEM is 8.05 ± 0.16 nm, and the 3-D APT value at 1024 h is 9.43 ± 0.65 nm, which is in reasonable agreement with the TEM value.

Fig. 5 displays the temporal evolution of $\phi_{\gamma'}(t)$, $N_v(t)$, and $\langle R(t) \rangle$ of the γ' (L₁₂)-precipitates as a function of aging time. The 3-D APT results, through 4096 h, are compared to results from the monovacancy-mediated LKMC₁ simulations through 800 h. The horizontal dashed line in Fig. 5a indicates that the equilibrium volume fraction, $\phi_{\gamma'}^{eq} = 13.48\%$, calculated using Dupin et al.'s phase diagram [70], is consistent with the $\phi_{\gamma'}(t = 4096h)$ value measured by 3-D APT, $12.80 \pm 1.40\%$, within experimental error. The temporal exponent of $N_v(t)$, q , is continuously evolving as the alloy proceeds from the growth and coarsening regime, III, into the quasi-stationary coarsening regime, IV, and it is anticipated to approach -1 at long aging times, Eq. (2), as described by the N(umerical)-model [88]. The temporal exponent q is calculated from the 3-D APT $N_v(t)$ data for the five longest aging times (64, 256, 1024, 2607, and 4096 h), yielding $q = -0.75 \pm 0.03$. Fig. 5b indicates the four regimes of phase separation: (I) quasi-stationary γ' (L₁₂)-precipitate nucleation; (II) concomitant γ' (L₁₂)-precipitate nucleation and growth; (III) concurrent growth and coarsening of γ' (L₁₂)-precipitates by the coagulation and coalescence mechanism; and (IV) quasi-stationary coarsening of γ' (L₁₂)-precipitates. Even though the transitions between these regimes are indicated

by sharp lines they are in fact more gradual. This is indicated by the overlapping precipitation kinetics in regimes (2) and (3). $N_v(t)$ is continuously increasing in regimes I and II, and continuously decreasing in regimes III and IV, which implies that nucleation of γ' (L₁₂)-precipitates has ceased by the end of regime II.

The $\langle R(t) \rangle$ values in Fig. 5c are determined using the *spherical volume equivalent radius method* [89,90], whereby the volume equivalent radius, R , of each γ' (L₁₂)-precipitate is calculated using the total number of atoms in a γ' (L₁₂)-precipitate given by the *so-called cluster analysis algorithm* in IVAS 3.6 [91,92]:

$$R = \left(\frac{3n}{4\pi\rho\zeta} \right)^{1/3} \quad (10)$$

where n is the total number of atoms enclosed within an iso-concentration surface; ρ is the atomic number density of the γ' (L₁₂)-phase, 86.22 atoms nm⁻³; and ζ is the detection efficiency of the 2-D microchannel plate (MCP), 50%, in the LEAP4000X Si tomograph. The quantity R assumes a spherical morphology for all γ' (L₁₂)-precipitates; it can be used to compare the dimensions of spheroidal γ' (L₁₂)-precipitates at aging times of <100 h with cuboidal γ' (L₁₂)-precipitates that appear at aging times >100 h, including the transition from spheroids-to-cuboids [89,90]. The 3-D APT data points within regime IV in Fig. 5c (64, 256, 1024, 2607, and 4096 h of aging) are fitted to Eq. (1) using a nonlinear multivariate regression analysis [58], which yields a temporal exponent of $1/p = 0.34 \pm 0.02$ for $\langle R(t) \rangle$, and a rate constant, $K = 2.09 \pm 0.10 \times 10^{-31}$ m³ s⁻¹. This experimental value of $1/p$ is in excellent agreement with the LS value of $1/3$. Once again, we utilized a nonlinear multivariate regression analysis [58] as opposed to assuming a temporal exponent of $1/3$ and then plotting $\langle R(t) \rangle^3$ versus time and calculating the coefficients of determination for this exponent. Supplement A1 explicates the reasons for not using the latter approach, which linearizes Eq. (1) and yields coefficients of determination that are similar for values of $1/p$ ranging from $1/2$ to $1/4$, thereby demonstrating that it is an insensitive mathematical methodology and should not be employed.

The numerical values of the 3-D APT results are also listed in Supplement D. The monovacancy-mediated LKMC₁ simulation results displayed in Fig. 5 are in generally good agreement with the 3-

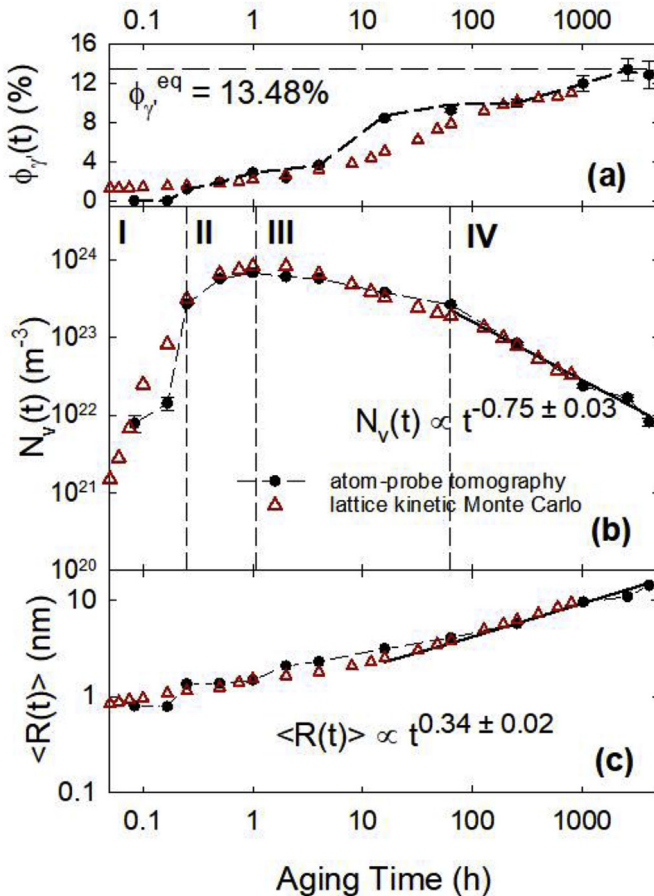


Fig. 5. The temporal evolution of: (a) the γ' (L₁₂)-precipitate volume fraction, $\phi_{\gamma'}(t)$; (b) number density, $N_v(t)$; and (c) mean radius, $\langle R(t) \rangle$, aged at 823 K (550 °C). The quantity $\langle R(t) \rangle$ is proportional to $t^{0.34 \pm 0.02}$, during quasi-stationary coarsening for aging times of 16 h and longer, as predicted by the LS and Calderon, Voorhees et al. (CVMK) diffusion-limited mean-field coarsening models. Once $\phi_{\gamma'}(t)$ is within 25% of the equilibrium volume fraction (>64 h of aging), the temporal dependence of the quantity $N_v(t)$ commences to approach t^{-1} , as predicted by the LS and CVMK diffusion-limited mean-field coarsening models. The numerical values can be found in [Supplement D](#).

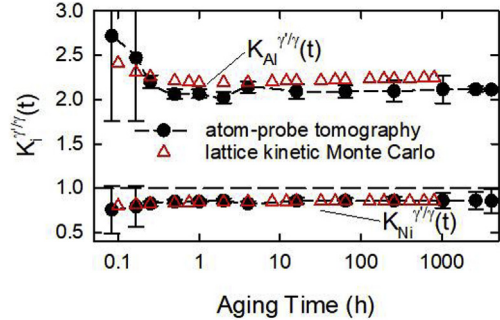


Fig. 7. The partitioning coefficients, $K_i^{\gamma'/\gamma}(t)$, of Al and Ni demonstrate that the Ni-12.5 Al at.% alloy aged at 823 K (550 °C) exhibits partitioning of Al to the γ' (L₁₂)-precipitates and Ni to the γ (f.c.c.)-matrix.

D APT results, but slightly underestimate $\phi_{\gamma'}(t)$ between 4 and 256 h of aging.

3.3. Temporal evolution of the compositions of the γ (f.c.c.)- and γ' (L₁₂)-phases

The compositions of the γ (f.c.c.)- and γ' (L₁₂)-phases, $C_{\text{Al}}^{\gamma}(t)$ and $C_{\text{Al}}^{\gamma'}(t)$, are displayed in Fig. 6a–b, respectively, from the 3-D APT derived proximity histograms [84,85] and the monovacancy-mediated LKMC₁ simulations. The numerical values from the 3-D APT results are listed in [Supplement B](#). The γ (f.c.c.)-phase experiences an initial state, where $C_{\text{Al}}^{\gamma}(t)$ remains approximately constant for aging times <1 h. At aging times >1 h, $C_{\text{Al}}^{\gamma}(t)$ and $C_{\text{Al}}^{\gamma'}(t)$ decrease continuously while the thermodynamic driving force (Al supersaturation) is concomitantly decreasing. The monovacancy-mediated LKMC₁ simulation results are in very good agreement with the experimental data for $C_{\text{Al}}^{\gamma}(t)$; they, however, slightly underestimate $C_{\text{Al}}^{\gamma}(t)$. The equilibrium concentrations of Al in the γ (f.c.c.)- and γ' (L₁₂)-phases, 11.14 ± 0.32 and 23.14 ± 0.47 at.%, respectively, are calculated by fitting the 3-D APT data, [Fig. 6](#) to Eq. (3), employing a nonlinear multivariate regression analysis [58]. Employing our GCMC simulations [22] to calculate the equilibrium concentrations of Al in the γ (f.c.c.)- and γ' (L₁₂)-phases yields values of 10.54 ± 0.15 and 23.24 ± 0.21 at.%, respectively. The data in

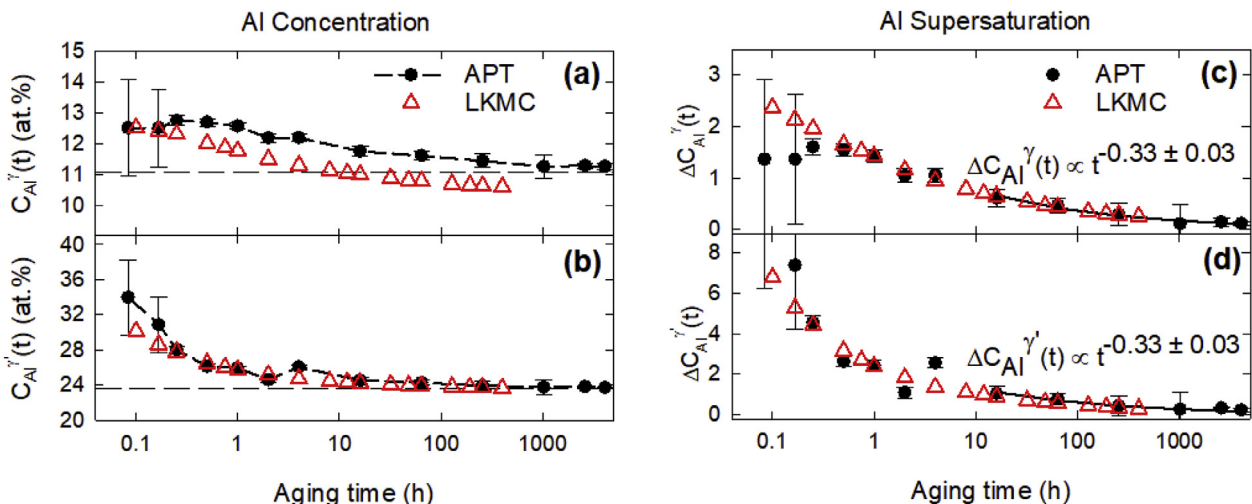


Fig. 6. Concentrations of Al in: (a) γ (f.c.c.)-matrix and (b) γ' (L₁₂)-precipitates (numerical values in [Supplement B](#)), and supersaturations of Al in (c) γ (f.c.c.)-matrix and (d) γ' (L₁₂)-precipitates from 3-D atom-probe tomography data and lattice kinetic Monte Carlo (LKMC₁) simulations. Both phases are initially supersaturated in Al and with increasing aging time the Al concentrations of the γ (f.c.c.)- and γ' (L₁₂)-phases approach equilibrium values of 11.14 ± 0.32 and 23.14 ± 0.47 at.%, respectively. At 4096 h of aging, the supersaturation of Al in the γ (f.c.c.)-matrix is essentially zero and hence it is not plotted on the log₁₀ scale.

Fig. 6a–b are also plotted on the partial Ni–Al phase diagram, **Fig. 2**, where the temporal compositional trajectories of both phases are indicated by horizontal bold black arrows going toward the left as the degree of phase separation increases with the Al-supersaturation concomitantly decreasing.

In the $[\gamma(\text{f.c.c.}) + \gamma'(\text{L}1_2)]$ phase-field, **Fig. 2**, the temporal compositional trajectory of the $\gamma(\text{f.c.c.})$ -phase evolves toward the solvus curve separating the $\gamma(\text{f.c.c.})$ -phase-field from the $[\gamma(\text{f.c.c.}) + \gamma'(\text{L}1_2)]$ phase-field, and at 4096 h it terminates on the overlapping solvus curves determined by Ma and Ardell [71] and Dupin et al. [70]. The initial composition of the $\gamma'(\text{L}1_2)$ -phase ($C_{\text{Al}}^{\gamma'} = 33.97 \pm 8.49$ at.%) is very far from the $[\gamma(\text{f.c.c.}) + \gamma'(\text{L}1_2)]/\gamma'(\text{L}1_2)$ solvus curves at 0.08 h of aging, which is initially in the indicated $[\gamma'(\text{L}1_2) + \text{NiAl(B2)}]$ phase-field. At 4096 h, the composition of the $\gamma'(\text{L}1_2)$ -phase approaches the solvus curve due to Saunders [68], Section 4.3.

The 3-D APT and monovacancy-mediated LKMC₁ simulation results for the temporal evolutions of $C_{\text{Al}}^{\gamma}(t)$ and $C_{\text{Al}}^{\gamma'}(t)$ are displayed in **Fig. 6c–d**, respectively, and their temporal exponents are also calculated using a nonlinear multivariate regression analysis technique [58]. The monovacancy-mediated LKMC₁ simulation results agree with the 3-D APT results for $\Delta C_{\text{Al}}^{\gamma}(t \geq 0.5\text{ h})$, **Fig. 6c**. In contrast, for aging times <0.5 h, the monovacancy-mediated LKMC₁ results exhibit a decrease in $\Delta C_{\text{Al}}^{\gamma}(t < 0.5\text{ h})$, while the 3-D APT results remain approximately constant, within experimental error, indicating that 3-D APT does not, for the LEAP 4000X Si, have sufficient detection efficiency to measure a decrease in $\Delta C_{\text{Al}}^{\gamma}(t)$ for very small $\gamma'(\text{L}1_2)$ -precipitates.

The 3-D APT results for $\Delta C_{\text{Al}}^{\gamma'}(t)$ decrease slightly more rapidly than the monovacancy-mediated LKMC₁ results, **Fig. 6d**. Eq. (3) is utilized to analyze the 3-D APT data, again employing a nonlinear multivariate regression analysis technique [58]. The 3-D APT temporal exponents for $\Delta C_{\text{Al}}^{\gamma}(t)$ and $\Delta C_{\text{Al}}^{\gamma'}(t)$ are both $1/r = -0.033 \pm 0.003$ (**Supplement A2**), which are in excellent

agreement with the LS value of $-1/3$. The resulting values of κ^{γ} and $\kappa^{\gamma'}$ from the 3-D APT data for the $\gamma(\text{f.c.c.})$ -matrix and $\gamma'(\text{L}1_2)$ -precipitates are 0.25 ± 0.01 and 0.68 ± 0.09 $\text{s}^{1/3}$, respectively. The corresponding κ^{γ} and $\kappa^{\gamma'}$ values from the monovacancy-mediated LKMC₁ results are 0.18 ± 0.01 and 0.47 ± 0.03 $\text{s}^{1/3}$, respectively, which are in approximate agreement.

The partitioning coefficients $K_{\text{Al}}^{\gamma'/\gamma}(t)$ and $K_{\text{Ni}}^{\gamma'/\gamma}(t)$ are displayed in **Fig. 7**, where $K_{\text{Al}}^{\gamma'/\gamma}(t)$ is defined as the ratio $C_i^{\gamma'}(t)$ to $C_i^{\gamma}(t)$, where the concentrations are in atomic fraction (at. fr.). The horizontal dashed line corresponds to $K_i^{\gamma'/\gamma}(t) = 1$, which indicates a complete absence of preferential partitioning behavior. **Fig. 7** demonstrates that for aging at 823 K (550 °C) Al partitions to the $\gamma'(\text{L}1_2)$ -phase and Ni to the $\gamma(\text{f.c.c.})$ -phase. Both $K_i^{\gamma'/\gamma}(t)$ ratios are slightly time-dependent for aging times <0.5 h, after which $K_{\text{Al}}^{\gamma'/\gamma}(t)$ approaches 2.1 and $K_{\text{Ni}}^{\gamma'/\gamma}(t)$ approaches 0.9.

3.4. Temporal evolution of the $\gamma'(\text{L}1_2)$ -precipitate size distributions (PSDs)

See **Supplement E1** for this section.

3.5. Temporal evolution of the fraction of $\gamma'(\text{L}1_2)$ -precipitates interconnected by necks, $f(t)$, and the minimum edge-to-edge distances, $\langle \lambda_{\text{edge-edge}}(t) \rangle$, between neighboring $\gamma'(\text{L}1_2)$ -precipitates

Fig. 8a displays $f(t)$ and **Fig. 8b** displays $\langle \lambda_{\text{edge-edge}}(t) \rangle$, for the 3-D APT experiments and monovacancy-mediated LKMC₁ simulations; the 3-D APT derived values are also included in **Supplement D**. An increase in $f(t)$ corresponds to a decrease in $\langle \lambda_{\text{edge-edge}}(t) \rangle$ and vice versa, as $\gamma'(\text{L}1_2)$ -precipitates need to be close to one another for coalescence and coagulation to occur [61]. The quantity $\langle \lambda_{\text{edge-edge}}(t) \rangle$ can be measured directly from the 3-D APT data set using the approach developed by Karnesky et al. [93]. Alternatively, Nembach's analytical equation for calculating $\langle \lambda_{\text{edge-edge}}(t) \rangle$ between $\gamma'(\text{L}1_2)$ -precipitates in a regular array is given by Ref. [94]:

$$\langle \lambda_{\text{edge-edge}}(t) \rangle = \sqrt{\frac{2\pi \langle R(t)^3 \rangle}{3\phi_{\gamma'}(t)\langle R(t) \rangle}} - 2\langle R(t) \rangle \quad (11)$$

The first-term on the right-hand side of Eq. (11) is the mean center-to-center distance between $\gamma'(\text{L}1_2)$ -precipitates and subtracting $2\langle R(t) \rangle$ from it yields $\langle \lambda_{\text{edge-edge}}(t) \rangle$; note that $\langle R(t)^3 \rangle$ is not equal to $\langle R(t) \rangle^3$. The two $R(t)$ related terms in the numerator and denominator of Eq. (11) do not cancel as $\langle R(t)^3 \rangle$ is greater than $\langle R(t) \rangle^3$ for all aging times due to the asymmetry of the PSDs, **Supplement E**. Based on Nembach's approach [94], $\langle \lambda_{\text{edge-edge}}(t) \rangle$ is large for the shortest aging time; for 0.08 h, $\langle \lambda_{\text{edge-edge}}(t) \rangle = 272.71 \pm 15.19$ nm, as $N_v(t)$ is initially small ($N_v(t=0.08\text{h}) = 7.88 \pm 1.97 \times 10^{21} \text{ m}^{-3}$). The quantity $\langle \lambda_{\text{edge-edge}}(t) \rangle$ then decreases with increasing aging time and finally it increases because $N_v(t)$ decreases at long aging times. The value of $\langle \lambda_{\text{edge-edge}}(t) \rangle$ is approximately a constant between 1 and 64 h [$10 < \langle \lambda_{\text{edge-edge}}(t) \rangle < 15$ nm], and eventually it increases to a final value of 37.38 ± 4.15 nm at 4096 h. Karnesky et al.'s approach calculates distances between $\gamma'(\text{L}1_2)$ -precipitates based on the X-Y-Z location of each $\gamma'(\text{L}1_2)$ -precipitate's center and its R value. It yields smaller values of $\langle \lambda_{\text{edge-edge}}(t) \rangle$ than does Nembach's model.

3-D APT results display a maximum in $f(t)$ at 1 h ($39.68 \pm 2.81\%$), while the monovacancy-mediated LKMC₁ simulation results display a maximum in $f(t)$ at 2 h (34.47%). The 3-D APT results for $f(t)$ at 2 h ($39.53 \pm 2.80\%$) are, however, almost identical to the 3-D APT results for $f(t)$ at 1 h, with a difference of only 0.4%, and hence the monovacancy-mediated LKMC₁ simulations agree with 3-D APT results for this quantity.

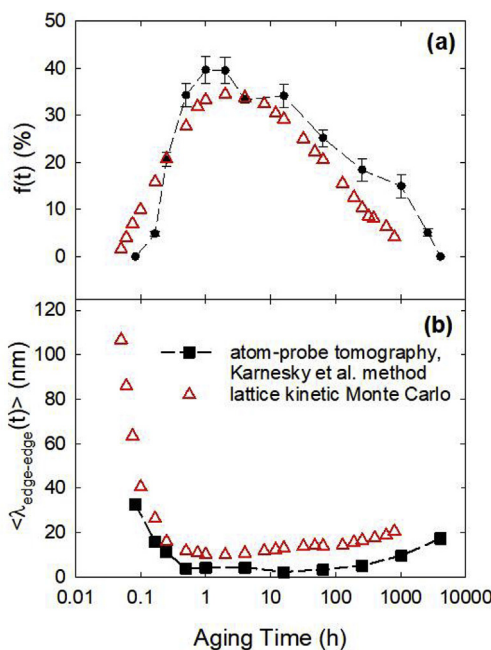


Fig. 8. (a) Fraction of $\gamma'(\text{L}1_2)$ -precipitates interconnected by necks, $f(t)$, as compared to (b) the mean minimum edge-to-edge distance between neighboring $\gamma'(\text{L}1_2)$ -precipitates, $\langle \lambda_{\text{edge-edge}}(t) \rangle$. The black solid-circles correspond to the APT results and the red outlined triangles represent the monovacancy-mediated LKMC₁ data. The numerical values can be found in **Supplement D**. (For interpretation of the references to colour in this figure legend, the reader is referred to the Web version of this article.)

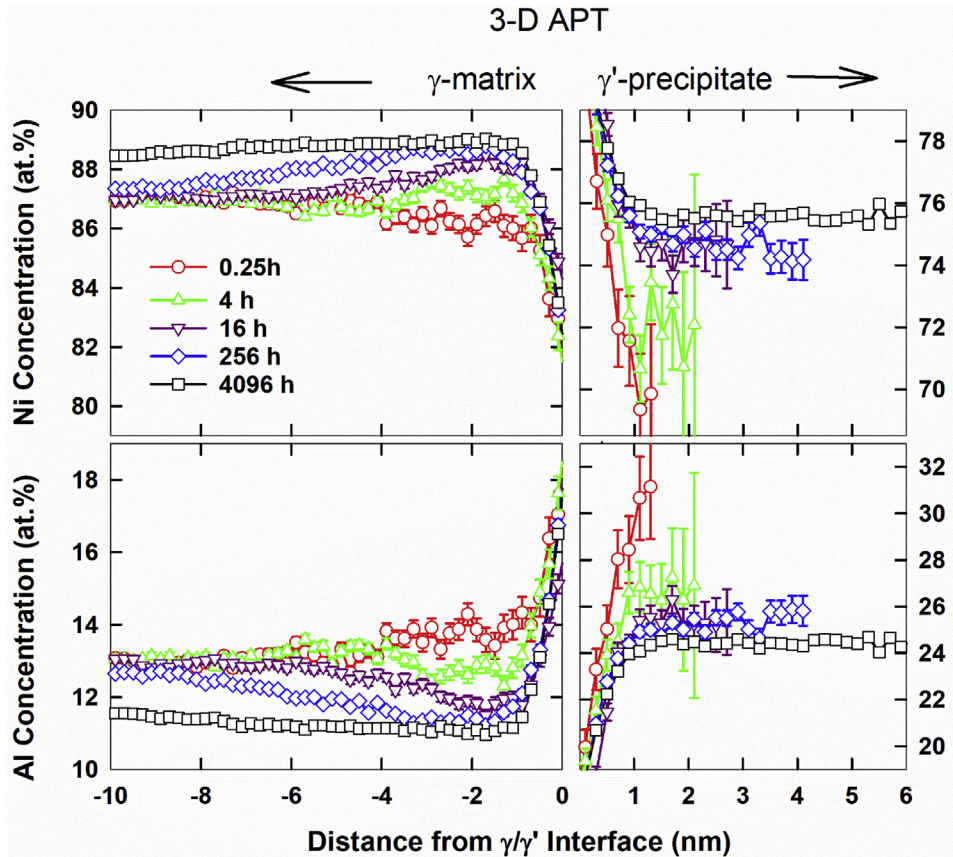


Fig. 9. Concentration profiles for Ni and Al on either side of the γ (f.c.c.)/ γ' (L1₂) interface for: (a) 0.25, 1, 256, and 4096 h extracted from 3-D APT data; and (b) 0.25, 4, 16, and 256 h from LKMC₁ simulations, Section 2.5. Positive distances are defined as into the γ' (L1₂)-precipitates, while negative distances are into the γ (f.c.c.)-matrix. The values of $\langle R(t) \rangle$ for these aging times are 1.34 ± 0.03 , 1.47 ± 0.03 , 5.65 ± 0.22 , and 14.59 ± 1.62 nm, respectively.

In summary, the monovacancy-mediated LKMC₁ results are in good agreement with the 3-D APT data for $\langle \lambda_{edge-edge}(t) \rangle$ calculated using Nembach's approach for aging times ≥ 0.25 h, and slightly overestimate the 3-D APT data for $\langle \lambda_{edge-edge}(t) \rangle$ calculated using Karnesky et al.'s approach, Fig. 8b. Monovacancy-mediated LKMC₁ results for $f(t)$ underestimate somewhat the experimental 3-D APT values at aging times greater than about 0.25 h. In LKMC₁, due to the small size of the simulation box, the periodic boundary conditions introduce artificially certain long-range ordering of the γ' (L1₂)-precipitates, which can account for this underestimation.

3.6. Temporal evolution of the interfacial compositional width, $\delta(t)$, between the gamma (f.c.c.)- and gamma-prime (L1₂ structure)-phases

Fig. 9 displays the concentration profiles for Ni and Al on both sides of the γ (f.c.c.)/ γ' (L1₂) interface for 0.25, 4, 16, 256, and 4096 h as measured by 3-D APT. A positive distance is defined as into the γ' (L1₂)-precipitates, while a negative distance is into the γ (f.c.c.)-matrix. At 1 h the γ (f.c.c.)/ γ' (L1₂) (100) interfacial width is initially somewhat diffuse [$\delta(t) = 1.71 \pm 0.08$ nm], with large values of ΔC_{Al}^{γ} and $\Delta C_{Al}^{\gamma'}$, Fig. 6c–d. An atomically sharp interface is given by a step function, which is an inadequate description of the interfaces we observe. With increasing aging time, the compositions of each phase are quasi-stationary and the γ (f.c.c.)/ γ' (L1₂) (100) interface width becomes sharper [$\delta(t = 4096\text{ h}) = 1.12 \pm 0.12$ nm], but they are never equal to zero; the difference between the two interfacial width values constitutes a 34% decrease. Moreover, while the concentration profiles for each phase change dramatically from

0.25 to 4 h and from 4 to 256 h, the changes from 256 to 4096 h are small. This is also demonstrated by the asymptotic approaches of C_{Al}^{γ} and $C_{Al}^{\gamma'}$ toward their equilibrium concentrations, Fig. 6a–b.

Fig. 10a displays $\delta(t)$ for the 3-D APT data, and the monovacancy-mediated LKMC₁ simulations as a function of aging time. The values for $\delta(t)$ are measured by fitting the concentration profiles across the γ (f.c.c.)/ γ' (L1₂) interface at each aging time to a spline curve, with the plateaus of the concentration profiles matching the far-field (ff) concentrations determined for the γ (f.c.c.)- and γ' (L1₂)-phases [95]. A spline fit produces a piecewise-defined function, where the distance between each data point in a data set is fit to a cubic interpolation [96]. The horizontal distance between the 10th and 90th percentiles of the concentration difference between the γ (f.c.c.)- and γ' (L1₂)-phases is defined to be $\delta(t)$ [95], which is the definition employed commonly in phase-field modeling. The spatial resolution of each concentration profile is 0.1 nm, which is less than the lattice parameter of Ni₃Al, 0.359 nm [67]. Note that all of the γ' (L1₂)-precipitates have a morphology with {100}-type facets starting at 2607 h, Fig. 4e, with the value of $\delta(t)$ decreasing with increasing aging time, as $t^{-0.08 \pm 0.01}$, Fig. 10a. Fig. 10b combines the $\langle R(t) \rangle$ data from Fig. 5c with the $\delta(t)$ data from Fig. 10a to display $\delta(t)$ as a function of $\langle R(t) \rangle$ for each aging time. The value of $\delta(t)$ is decreasing continuously as $\langle R(t) \rangle$ is increasing, varying as $\langle R(t) \rangle^{-0.47 \pm 0.03}$. The value of $\delta(t)$ is asymptotically approaching a constant value at the longest aging time, 4096 h, which is definitely not equal to zero. We measured $\delta(t)$ at long aging times (> 1000 h) for the {100}-type interface planes because the γ' (L1₂)-precipitates are mainly cuboidal at 1024 h and are additionally aligning and rafting along <100>-type directions: TEM micrograph, Fig. 4g. The

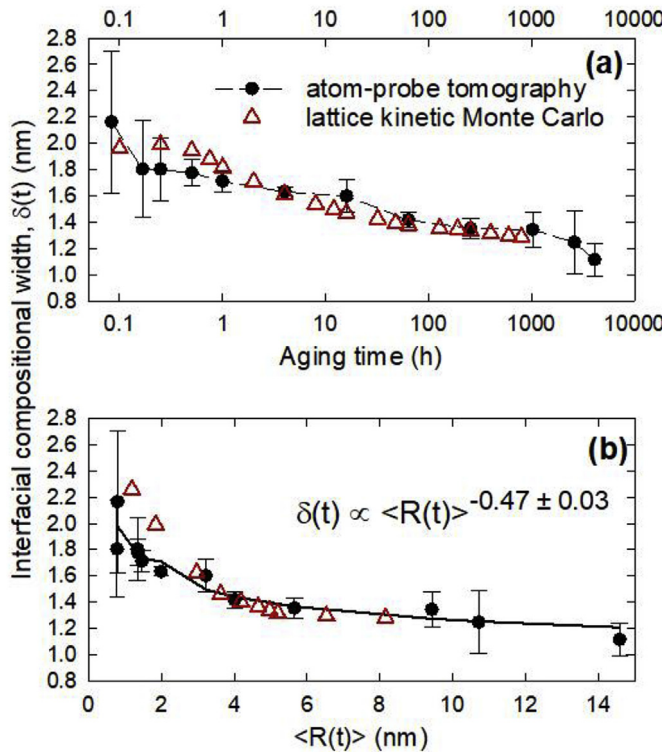


Fig. 10. (a) Effect of aging time on the interfacial compositional width between the γ (f.c.c.)- and γ' (L1₂)-phases for a {100}-type plane. The interfacial compositional width is defined using the 10 and 90% points when fitting the proximity histogram for each dataset to a spline curve: (a) the value of $\delta(t)$ varies as $t^{-0.08 \pm 0.01}$; (b) Combination of the $\langle R(t) \rangle$ data from Fig. 5c with the $\delta(t)$ data from Fig. 10(a) to display the relationship between $\delta(t)$ and $\langle R(t) \rangle$ as the alloy is aged. The quantity $\delta(t)$ decreases continuously with increasing $\langle R(t) \rangle$, varying as $\langle R(t) \rangle^{-0.47 \pm 0.03}$, which is in strong contrast to the relationship obtained based on the so-called trans-interface-diffusion-controlled (TIDC) ansatz.

significance of the results presented in Fig. 10 concerning the time dependency of $\delta(t)$ and the dependency of $\delta(t)$ on $\langle R(t) \rangle$ are discussed in Section 4.6.

3.7. Calculation of four different diffusivities based on monovacancy-mediated lattice-kinetic Monte Carlo simulations

3.7.1. The monovacancy's trajectories in four distinct regions

Fig. 11, taken from LKMC₁ simulations (Supplement C and Table C1), displays three stages of precipitate evolution (right-hand column) together with successive locations of the monovacancy at work in LKMC₁, during this process (left-hand column). In the left-hand column, the γ (f.c.c.)-matrix appears as the yellow background, and successive positions of the monovacancy are indicated by red-dots. In the right-hand column, Ni and Al atoms are only displayed in the γ' (L1₂)-precipitate, respectively in green and red.

In Fig. 11, the two first rows (a, b and c, d) deal with the coagulation and coalescence of two γ' (L1₂)-precipitates at, respectively, 1 and 4 h, at 823 K (550 °C) in a 128 × 128 × 128 lattice sites super-cell. The third row (Fig. 11 e, f) displays the growth of a single precipitate at 400 h, at the same temperature, in a 256 × 256 × 256 lattice sites super-cell.

The partial ordering of Ni and Al atoms within the γ' (L1₂)-precipitates and the neck region are clearly evident (Fig. 11b and d). At 1 and 4 h the γ' (L1₂)-precipitates do not yet exhibit {100}-type facets, while these facets are clearly evident at 400 h, consistent

with the 3-D APT reconstructions, Fig. 4. Additionally, the interfacial regions between the γ (f.c.c.)-matrix and γ' (L1₂)-precipitates (Fig. 11b, d, and 11f) are all qualitatively diffuse: less so at 1 and 4 h than at 400 h. Table 3 presents the normalized times, t/t_{matrix} , the monovacancy spends in the four distinct regions: (1) the γ (f.c.c.)-matrix; (2) the γ' (L1₂)-precipitates; (3) the partially ordered neck connecting two γ' (L1₂)-precipitates; and (4) the super-cell for 1 and 4 h, Fig. 11, normalized to the volume of the cell. The monovacancy is 3.12–3.25 times more likely to be found inside the γ' (L1₂)-precipitates than in the γ (f.c.c.)-matrix, and 3.58 to 3.85 times more likely to be found inside the neck region connecting the two γ' (L1₂)-precipitates than in the γ (f.c.c.)-matrix at 1 and 4 h. Note that the normalized times decrease with increasing aging time, Table 3.

Fig. 11b, d, and 11f display the positions of the Ni (green) and Al (red) atoms for γ' (L1₂)-precipitates at 1, 4 and 400 h, respectively. Fig. 11b, d and 11f complement and supplement Fig. 11a, 11c and 11e, with the former showing the positions of the Ni and Al atoms, and the latter displaying the positions of the single monovacancy as a function of time. The partial ordering of the Ni and Al atoms within the γ' (L1₂)-precipitates and the neck-region are clearly evident: Fig. 11b and d. At 1 and 4 h the γ' (L1₂)-precipitates do not yet exhibit {100}-type facets, while these facets are clearly evident at 400 h, in agreement with the 3-D APT reconstructions in Fig. 4. Additionally, the interfacial regions between the γ (f.c.c.)-matrix and γ' (L1₂)-precipitates, Fig. 11b, d, and 11f, are all qualitatively diffuse: less so at 1 and 4 h than at 400 h.

3.7.2. Calculations of the four different diffusivities D_i^{region}

Table 3 presents four different calculated diffusivities, D_i^{region} , based on the following standard equation [97,98], Eq. (12), where D_i^{region} includes the correlation factor for a monovacancy diffusion mechanism. The correlation factor for random walk in an f.c.c. crystal structure is 0.78 for a tracer-diffusion experiment [99]. The binary alloy studied herein has strong correlations between diffusional fluxes, which are less than 0.78. Bocquet utilized a novel jump frequency model, taking into account the full range of solute–vacancy interactions up to third NN sites, and determined it in the dilute Ni–Cr system, 0.41 [100]. Ramunni studied diffusion coefficients of solute atoms in the Ni–Al and Al–U systems employing the classical molecular statics technique (CMST), where migrating solute atoms interchange with 1st NN vacancies in the temperature range 700–1700 K, where there is experimental data. Ramunni determined the correlation factor for solute atoms using the five-frequency model. The relevant value for dilute Ni–Al alloys is 0.611 at 823 K [101], which is an upper bound of this value and therefore the diffusivities calculated using this value are also upper bounds. There isn't prior research data on correlated diffusion in either γ' (L1₂) or the ordered interconnected neck regions. In this study, the diffusivity is calculated using the following expression, which is at a specified temperature, for the root-mean-square diffusion distance:

$$\sqrt{4D_i^{\text{region}}t} = \sqrt{n_{\text{correlation}}^{\text{region}, \text{Ni-Al}} n_j \alpha^2} \quad (12)$$

where n_j is the total number of jumps made by the monovacancy for all its exchanges with an atom of type i ($i = \text{Ni}$ or Al) in a time t in a specified region; and α is the jump distance, $a_0/\sqrt{2}$, where a_0 is the lattice parameter of Ni₃Al(L1₂). Time, t , in Eq. (12), is a rescaled monovacancy-mediated LKMC₁ time, which has been adjusted for the difference in the monovacancy concentrations between the LKMC₁ cell and a bulk material, utilizing Eq. (14)(Supplement C1). The quantity n_j is multiplied by a correlation factor, $\eta_{\text{correlation}}^{\text{region}, \text{Ni-Al}}$, which reduces the value of each D_i^{region} caused by correlations

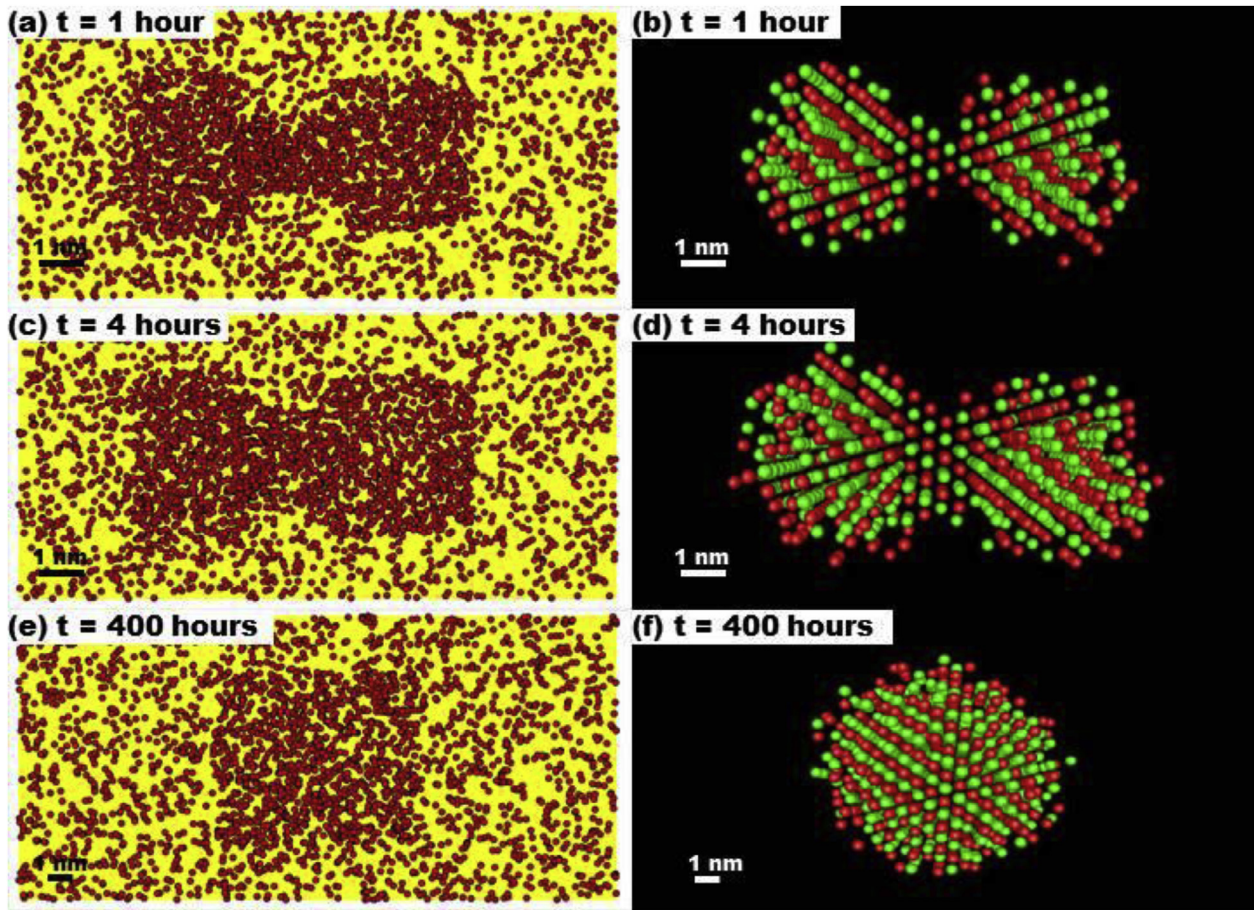


Fig. 11. LKMC₁ snapshots of two γ' (L1₂)-precipitates in a γ (f.c.c.)-matrix (yellow background) at (a) 1 and (c) 4 h of aging time at 823 K (550 °C) for a 128 × 128 × 128 cell; and (e) an LKMC₁ snapshot of a single γ' (L1₂)-precipitate in a γ (f.c.c.)-matrix at 400 h of aging time at 823 K (550 °C) for a 256 × 256 × 256 cell. (a), (c), and (e) display the positions of a single monovacancy's trajectory (red circles) using monovacancy-solute binding energies through 4th NN distance. Note that the monovacancy spends the majority of its time inside the γ' (L1₂)-precipitates and the partially ordered necks between them, (a), (c), and (e). Additionally, the corresponding positions of the Ni (green) and Al (red) atoms are displayed for the γ' (L1₂)-precipitates for (b) 1, (d) 4, and (f) 400 h of aging. The partial ordering of the atoms in an L1₂ structure is evident in (b), (d), and (f). At 400 h the γ' (L1₂)-precipitate has {100}-type facets and appears to be essentially fully ordered; its interface is qualitatively diffuse. The compositional interfacial width is quantified in Fig. 10. (For interpretation of the references to colour in this figure legend, the reader is referred to the Web version of this article.)

Table 3

Relative rescaled monovacancy-mediated lattice-kinetic Monte Carlo (LKMC₁) simulations times spent by the monovacancy in the γ (f.c.c.)-matrix, the γ' (L1₂)-precipitates, the neck between two γ' (L1₂)-precipitates, and in the supercell for the aging times 1, 4 and 400 h. Fig. 11, are normalized to the volume of the supercell. The different diffusivities for Al and Ni for each region, D_i^{region} , calculated utilizing monovacancy-mediated LKMC₁ simulations, Eq. (12), for 1, 4, and 400 h, are listed in the last three columns. Too few interconnected γ' (L1₂)-precipitates are detected for 400 h to yield satisfactory statistics, and therefore there aren't D_i^{neck} values listed. All values include a correlation factor for a monovacancy diffusion mechanism in a f.c.c. lattice, 0.611.

Region	Ratio of relative travel time, t/t_{matrix} (normalized to volume of cell)		$D_{\text{Al}}^{\text{region}} (\times 10^{-21} \text{ m}^2 \text{ s}^{-1})$			$D_{\text{Ni}}^{\text{region}} (\times 10^{-22} \text{ m}^2 \text{ s}^{-1})$		
	1 h	4 h	1 h	4 h	400 h	1 h	4 h	400 h
1. γ (f.c.c.)-matrix	1	1	2.22 ± 0.38	2.18 ± 0.36	1.62 ± 0.26	1.11 ± 0.14	1.02 ± 0.38	0.99 ± 0.14
2. γ' (L1 ₂)-precipitates	3.12	3.25	1.22 ± 0.17	1.16 ± 0.15	0.71 ± 0.09	0.57 ± 0.06	0.45 ± 0.17	0.33 ± 0.03
3. Neck region	3.85	3.58	1.11 ± 0.19	1.15 ± 0.19	—	0.49 ± 0.07	0.53 ± 0.19	—
4. supercell	—	—	2.19 ± 0.26	2.04 ± 0.26	1.51 ± 0.14	1.07 ± 0.11	0.98 ± 0.26	0.93 ± 0.09

among diffusion fluxes. We use 0.611 from Ref. [101] for all regions due to the lack of the availability of diffusion data with correlation. We note that this value only applies to the disordered matrix and it should be smaller than 0.611 in both the γ' (L1₂)-precipitates and the interconnected ordered neck-regions. The diffusivities in these two regions can be estimated from the vacancy formation energy

and the migration energy using the five-frequency model, with the consideration of the local atomic environment, in a concentrated alloy system [102].

3.7.3. Four distinct aluminum diffusivities

For exchanges between Al atoms and the monovacancy the

calculated diffusivity in the γ (f.c.c.)-matrix, $D_{Al}^{\gamma\text{-matrix}}$, has the largest value, $(2.22\text{--}1.62) \times 10^{-21} \text{ m}^2 \text{s}^{-1}$, of the four calculated diffusivities listed in Table 3. The calculated value of the Al diffusivity in the γ' (L1₂)-precipitates, $D_{Al}^{\gamma'\text{-precipitates}}$, ranges from $(1.22\text{--}0.71) \times 10^{-21} \text{ m}^2 \text{s}^{-1}$, which is 43–56% smaller than $D_{Al}^{\gamma\text{-matrix}}$. The calculated value of the Al diffusivity in the neck region, D_{Al}^{necks} , is $(1.11\text{--}1.15) \times 10^{-21} \text{ m}^2 \text{s}^{-1}$, which is 46–48% smaller than $D_{Al}^{\gamma\text{-matrix}}$. The value of D_{Al}^{necks} is measured only at 1 and 4 h, because too few necks between γ' (L1₂)-precipitates are detected at 400 h to obtain good statistics.

3.7.4. Four distinct nickel diffusivities

For exchanges between Ni atoms and the monovacancy, all the calculated diffusivities listed in Table 3 are smaller than those for Al exchanges with the monovacancy in the corresponding regions by an order-of-magnitude. This was anticipated because Al is a significantly faster diffuser in Ni than is Ni in Ni. $D_{Ni}^{\gamma\text{-matrix}}$ has the largest value, $(1.11\text{--}0.99) \times 10^{-22} \text{ m}^2 \text{s}^{-1}$, of the four calculated diffusivities listed in Table 3. $D_{Ni}^{\gamma'\text{-precipitates}}$ ranges from $(0.57\text{--}0.33) \times 10^{-22} \text{ m}^2 \text{s}^{-1}$, which is 55–69% smaller than $D_{Ni}^{\gamma\text{-matrix}}$. Additionally, the calculated value of D_{Ni}^{necks} is $(0.49\text{--}0.53) \times 10^{-22} \text{ m}^2 \text{s}^{-1}$, which is 51–56% smaller than $D_{Ni}^{\gamma\text{-matrix}}$. As is the Al-case, D_{Ni}^{necks} is measured only at 1 and 4 h because too few necks between γ' (L1₂)-precipitates are detected at 400 h to obtain good statistics. While $D_{Al}^{\gamma'\text{-precipitates}}$ is consistently greater than D_{Al}^{necks} , the values of $D_{Ni}^{\gamma'\text{-precipitates}}$ and D_{Ni}^{necks} are approximately equal to one another.

3.7.5. The diffusivities of Ni and Al in the supercell $D_i^{\text{supercell}}$

The values of $D_i^{\text{supercell}}$ in Table 3 are obtained for 1, 4 and 400 h by taking a weighted average of the calculated D_i^{region} values, based on the fraction of the total volume of the cell that each region occupies. The volume occupied by the neck region is defined as the volume where the short-range order parameter is 80% of that of the γ' (L1₂)-phase. For both $D_{Ni}^{\text{supercell}}$ and $D_{Al}^{\text{supercell}}$, their weighted averages are 38–64% greater than $D_i^{\gamma'\text{-precipitates}}$, 5–36% smaller than $D_i^{\gamma\text{-matrix}}$, and 47–56% greater than D_i^{necks} .

4. Discussion

4.1. Temporal evolution of the Vickers microhardness values

The Vickers microhardness of Ni-12.5 Al at.% aged at 823 K (550 °C) is directly proportional to $\phi_{\gamma'}(t)$ at early aging times and inversely proportional to $\langle \lambda_{\text{edge-edge}}(t) \rangle$ at long aging times. The Vickers microhardness values increase continuously through 1024 h of aging after a small decrease at 0.25 h, Fig. 3. The peak microhardness achieved is 247 ± 11 at 1024 h, with $\phi_{\gamma'}(t)$ increasing from 2.87 ± 0.05 at 1 h to $11.96 \pm 0.82\%$ at 1024 h. The continuous increase in $\phi_{\gamma'}(t)$ between 1 and 1024 h, Fig. 5a, explains the continuous increase in the value of the Vickers microhardness during this same time frame. The slight decrease in Vickers microhardness at 2607 h to 233 ± 5 may be accounted for by the alignment of γ' (L1₂)-precipitates along a <100>-type direction (rafting), which begins to occur at 1024 h, Fig. 4d and g. Additionally, the value of the Vickers microhardness is inversely proportional to the value of $\langle \lambda_{\text{edge-edge}}(t) \rangle$ for the Orowan dislocation-looping strengthening mechanism, which is consistent with this strengthening mechanism at room temperature, where $\phi_{\gamma'}(t)$ is continuously increasing. The value of $\langle \lambda_{\text{edge-edge}}(t) \rangle$ is in the range 10–15 nm between 1 and 64 h of aging, Fig. 8b, before increasing to 26.80 ± 2.18 nm at 2607 h of aging.

4.2. Temporal evolution of the γ' (L1₂-structure) precipitate volume fraction, $\phi_{\gamma'}(t)$, number density, $N_v(t)$, and mean radius $\langle R(t) \rangle$

4.2.1. Temporal evolution of the volume fraction of γ' (L1₂-structure)-precipitates $\phi_{\gamma'}(t)$

Our results for $\phi_{\gamma'}(t)$ indicate that at 4096 h of aging at 823 K (550 °C) it has achieved its equilibrium value, $\phi_{\gamma'}^{\text{eq}}$. Different values of $\phi_{\gamma'}^{\text{eq}}$ are calculated using the lever rule from the solvus curves, Fig. 2. The $\phi_{\gamma'}^{\text{eq}}$ values of the γ' (L1₂)-phase at 823 K (550 °C) are 18.33, 13.48, 15.02, and 16.75 vol% using the Saunders, Dupin et al., Ma and Ardell, and GCMC solvus curves, respectively [22,68–71]. At the longest aging time, $\phi_{\gamma'}(t = 4096\text{h})$ is $12.80 \pm 1.40\%$, which is 7% smaller than the Dupin et al. value of $\phi_{\gamma'}^{\text{eq}}$, and 31% smaller than the Saunders value of $\phi_{\gamma'}^{\text{eq}}$. The $\phi_{\gamma'}(t = 4096\text{h})$ is, however, equal to the Dupin et al. value of $\phi_{\gamma'}^{\text{eq}}$ within error, implying that this alloy has most likely achieved its equilibrium volume fraction after 4096 h of aging at 823 K (550 °C). Therefore, the Dupin et al. value is in the best agreement with the 3-D APT data, Fig. 5a. The monovacancy-mediated LKMC₁ simulation result for 800 h has not achieved an equilibrium value of $\phi_{\gamma'}$, but an extrapolation of the monovacancy-mediated LKMC₁ trajectory, Fig. 5a, indicates agreement with Dupin et al.'s results as well. A summary of the $\phi_{\gamma'}^{\text{eq}}$ values is presented in Table 4.

4.2.2. Temporal evolution of the number density of γ' (L1₂-structure)-precipitates $N_v(t)$

Our results for the temporal evolution of $N_v(t)$ indicate that four regimes, from nucleation through coarsening, are observed for Ni-12.5 Al at.% aged at 823 K (550 °C) for 0.08–4096 h. We focus mainly on discussing regimes I and IV.

4.2.2.1. Regime I: quasi-stationary nucleation of γ' (L1₂)-precipitates. The quasi-stationary γ' (L1₂)-precipitate nucleation regime, indicated by the initial rapid increase in $N_v(t)$, regime I in Fig. 5b, can be modeled using classical nucleation theory (CNT) [30,88,103–113]. CNT states that the supersaturation of an element in a binary system depends on a Helmholtz free energy expression, which has both a chemical energy component, ΔF_{ch} (which is negative), and an elastic strain energy component, ΔF_{el} (which is always positive).

For the strain energy to depend solely on $\langle R(t) \rangle$, one must assume that there are no precipitate-precipitate elastic interactions; that is, the solid-solution is elastically isotropic and the γ' (L1₂)-precipitates have the same elastic moduli as the γ (f.c.c.)-matrix. The fact that rafting is observed during the later stages implies that this is not the case. Such effects are, however, negligible during the early stages of nucleation because $\langle \lambda_{\text{edge-edge}}(t) \rangle$ is large, Fig. 8b, and hence this assumption is reasonable for regime I. The Helmholtz free energy expression also contains an interfacial free energy term, $\sigma_{\gamma/\gamma'}$, which is always positive. The net reversible work required for the formation of a spherical nucleus, W_R , as a function of a nucleus's radius, R , is given by:

Table 4

Equilibrium volume fraction of the γ' (L1₂)-phase, $\phi_{\gamma'}^{\text{eq}}$, as determined by: (a) Thermo-Calc using two different thermodynamic databases (Saunders and Dupin et al.); (b) the Ni-Al phase diagram (Ma and Ardell); (c) experimental 3-D atom-probe tomographic data from this study at 4096 h; and (d) our grand canonical Monte Carlo (GCMC) simulation for Ni-12.5 Al at.% aged at 823 K.

Source	$\phi_{\gamma'}^{\text{eq}}$
Saunders [68]	18.33%
Dupin et al. [70]	13.48%
Ma and Ardell [71]	15.02%
3-D APT data for 4096 h	$12.80 \pm 1.40\%$
GCMC [22]	16.56%

$$W_R = (\Delta F_{ch} + \Delta F_{el}) \frac{4\pi}{3} R^3 + 4\pi R^2 \sigma^{\gamma/\gamma'} \quad (13)$$

The critical radius, R^* , for nucleation is:

$$R^* = -\frac{2\sigma^{\gamma/\gamma'}}{\Delta F_{ch} + \Delta F_{el}} \quad (14)$$

and the critical net reversible work required for the formation of a critical spherical nucleus, W_R^* , is:

$$W_R^* = \frac{16\pi}{3} \frac{(\sigma^{\gamma/\gamma'})^3}{(\Delta F_{ch} + \Delta F_{el})^2} \quad (15)$$

Alternatively, R^* can be derived using capillarity theory by considering the Hessian matrix of the Gibbs free energy of all the terms, including off-diagonal terms [114].

The chemical formation free energies are calculated based on a first-principles dilute solid-solution model, $Ni_xAl \rightarrow Ni_3Al + Ni_{x-3}$, where $x = 31$. The equation for ΔF_{ch} is given by:

$$\begin{aligned} \Delta F_{ch} &= \Delta F(Ni_3Al) + (x-3)\Delta F(Ni) - \Delta F(Ni_xAl) - T[\Delta S(Ni_3Al) \\ &= [\Delta H(Ni_3Al) - \Delta H(Ni_xAl)] \\ &\quad - \Delta S(Ni_xAl)] \end{aligned} \quad (16)$$

where ΔH and ΔS are the enthalpy and entropy changes of formation, respectively. We take ΔH to be equal to the internal energy change of formation because in the solid-state the pressure-volume term in ΔH is negligible compared to the internal energy change. The entropy changes of formation are based on the vibrational entropies of the ordered Ni_3Al and Ni_xAl cells. The calculated value of ΔF_{ch} of $Ni_3Al(L1_2)$, using Eq. (16), is $-7.86 \times 10^7 \text{ kJ m}^{-3}$ at 823 K (550°C). An alternative value can be calculated using a classical thermodynamic methodology [88,115], which yields $\Delta F_{ch} = -6.70 \times 10^6 \text{ kJ m}^{-3}$, which is within the experimentally measured range of values of -4.93×10^6 to $-6.97 \times 10^6 \text{ kJ m}^{-3}$ in the temperature range 820 K (547°C) to 920 K (647°C) [116].

The ΔF_{el} value is small in magnitude compared to the thermodynamic driving force during nucleation, and is calculated using the approach outlined by Booth-Morrison et al. [30,117]:

$$\Delta F_{el} = \frac{2\mu^\gamma B^{\gamma'} (V_a^{\gamma'} - V_a^\gamma)^2}{(3B^{\gamma'} + 4\mu^\gamma)(V_a^{\gamma'})^2} \quad (17)$$

where μ^γ is the shear modulus of the γ (f.c.c.)-matrix phase; $B^{\gamma'}$ is the bulk modulus of the $\gamma'(L1_2)$ -phase; and $V_a^{\gamma'}$ and V_a^γ are the atomic volumes of the γ (f.c.c.)-matrix and $\gamma'(L1_2)$ -precipitates, respectively. The value of μ^γ is 100 GPa [118], and the value of $B^{\gamma'}$ is 175 GPa [119]. The values of $V_a^{\gamma'}$ and V_a^γ are calculated based on the lattice parameters of the γ (f.c.c.)-matrix and $\gamma'(L1_2)$ -precipitates, 3.58 Å and 3.59 Å, respectively [67]; this small lattice parameter mismatch, 0.01 Å, implies that the $\gamma'(L1_2)$ -precipitates are coherent with the γ (f.c.c.)-matrix. This approach yields $\Delta F_{el} = 4.96 \times 10^6 \text{ kJ m}^{-3}$ at 823 K (550°C), which is 6% of ΔF_{ch} as calculated employing Eqs. (16), and 74% of ΔF_{ch} as calculated using a classical thermodynamic approach [88,115]; the latter is dependent on the thermodynamic activities of Al and Ni. Because the thermodynamic activities of Al are unmeasured for Ni-12.5 Al at.% at 823 K (550°C), approximate estimates are used in the calculations. We, therefore, employ the value of ΔF_{ch} calculated using a first-principles approach, Eq. (16), as opposed to the classical thermodynamic approach. Booth-Morrison et al. found a similar

relationship between ΔF_{ch} , which was calculated using Saunders' database in Thermo-Calc [68,69], and ΔF_{el} for a Ni-6.5 Al-9.5 Cr at.% alloy aged at 873 K; they calculated ΔF_{ch} to be $-6.25 \times 10^7 \text{ kJ m}^{-3}$ and ΔF_{el} to be $2.67 \times 10^6 \text{ kJ m}^{-3}$, making ΔF_{el} 4% of ΔF_{ch} for this ternary Ni-Al-Cr alloy [30].

We then calculate the stationary nucleation current, J_{CNT}^{st} , the number of nuclei formed per unit volume per unit time ($\text{m}^{-3} \text{ s}^{-1}$) [22,30], from:

$$J_{CNT}^{st} = Z\beta^* N \exp\left(-\frac{W_R(R^*)}{k_b T}\right) \quad (18)$$

where Z is the Zeldovich factor, which accounts for the dissolution of supercritical clusters; β^* is a kinetic coefficient describing the rate of condensation of single atoms on the critical nuclei; and N is the total number of possible nucleation sites per unit volume. The value of N is taken to be the volume density of lattice sites occupied by the precipitating solute element, Al [103,120], which yields an absolute upper bound to the classical homogeneous nucleation current. The quantities Z and β^* are given by:

$$Z = \left(-\left(\frac{\partial W_{R,i}^*}{\partial n_i} \right) \left(\frac{1}{2\pi k_b T} \right) \right)^{1/2} \quad (19)$$

$$\beta^* = \frac{4\pi(R^*)^2 D_{solute}^{coarsening} C_0}{\langle a \rangle^4} \quad (20)$$

where C_0 is the initial concentration of the precipitating solute-element. And $\langle a \rangle$ is the mean of the lattice parameters of the γ (f.c.c.)-matrix and $\gamma'(L1_2)$ -precipitates, 0.3585 nm [67]. And n_i is the average number of atoms in each precipitate. Using a value of $28.55 \pm 1.61 \text{ mJ m}^{-2}$ for $\sigma^{\gamma/\gamma'}$ (calculated using the Dupin et al. thermodynamic database [70], Section 4.7), Eqs. (14) and (15) yield $R^* = 0.68 \text{ nm}$ and $W_R^* = 7.19 \times 10^{-20} \text{ J}$. Alternatively, R^* and W_R^* are 0.72 nm and $8.29 \times 10^{-20} \text{ J}$, respectively, if a value of $29.94 \pm 1.69 \text{ mJ m}^{-2}$ is chosen for $\sigma^{\gamma/\gamma'}$ (calculated using Saunders's thermodynamic database [68], Section 4.7). These values of R^* are slightly smaller, by 0.07–0.11 and 0.12–0.16 nm, than the smallest values of $\langle R(t) \rangle$ measured by 3-D APT ($\langle R(t = 0.08 \text{ h}) \rangle = 0.79 \pm 0.20 \text{ nm}$) and monovacancy-mediated LKMC₁ ($\langle R(t = 0.05 \text{ h}) \rangle = 0.84 \text{ nm}$), respectively, which are physically reasonable results. Using these values and $D_{experiment}^{coarsening} = 2.51 \pm 0.14 \times 10^{-21} \text{ m}^2 \text{ s}^{-1}$ (Section 4.8.2), J_{CNT}^{st} is $1.34 \times 10^{22} \text{ m}^{-3} \text{ s}^{-1}$ (for a $\sigma^{\gamma/\gamma'}$ value of $28.55 \pm 1.61 \text{ mJ m}^{-2}$). Alternatively, it is $5.20 \times 10^{21} \text{ m}^{-3} \text{ s}^{-1}$ for $\sigma^{\gamma/\gamma'} = 29.94 \pm 1.69 \text{ mJ m}^{-2}$. This value is 66 times greater than the 3-D APT value, J_{APT}^{st} , of $2.03 \times 10^{20} \text{ m}^{-3} \text{ s}^{-1}$ and 57 times greater than the monovacancy-mediated LKMC₁ value, J_{LKMC}^{st} , of $2.37 \times 10^{20} \text{ m}^{-3} \text{ s}^{-1}$. In general, calculated values of J_{CNT}^{st} are significantly greater than experimentally measured values of the stationary nucleation current, $J_{experiment}^{st}$, with the former being 7 to 707 times greater than the latter for Ni-Al and Ni-Al-Cr alloys, Table 5 [22,30,121], respectively. Xiao and Haasen obtained a value of $4.1 \times 10^{22} \text{ m}^{-3} \text{ s}^{-1}$ for J_{CNT}^{st} , as compared to $8.4 \times 10^{19} \text{ m}^{-3} \text{ s}^{-1}$ for $J_{experiment}^{st}$ using HREM for Ni-12 Al at.% aged at 773 K (500°C), which makes J_{CNT}^{st} 488 times greater than $J_{experiment}^{st}$ [121]. This is most likely because they calculated ΔF_{ch} and ΔF_{el} using the activity of Al from Ref. [88], which is unmeasured in the Ni-Al system at 773 K (500°C).

The calculated value of J_{CNT}^{st} is linearly proportional to N , Eq. (18), where we assumed initially that every Al solute atom in solid-solution serves as a possible nucleation site for a $\gamma'(L1_2)$ -precipitate, whereas the correct effective value of N is much smaller.

Table 5

Comparison of calculated and atom-probe tomographic measured values of the stationary nucleation current, number of nuclei per unit volume per unit time, from the archival literature and current research. The ratio of J_{CNT}^{st} , calculated assuming classical nucleation theory (CNT) to $J_{experiment}^{st}$ measured experimentally is given for each case. For the Ni-12 Al at.% alloy $J_{experiment}^{st}$ was measured using high-resolution transmission electron microscopy [121], whereas for the Ni-12.5 Al at.% and three Ni-Al-Cr alloys atom-probe tomography was utilized.

Alloy composition (at.%)	Aging Temperature (K)	J_{CNT}^{st} from CNT ($\text{m}^{-3} \text{s}^{-1}$)	$J_{experiment}^{st}$ from experimental data ($\text{m}^{-3} \text{s}^{-1}$)	Ratio of J_{CNT}^{st} to $J_{experiment}^{st}$	$N_{effective}/N(\%)$	Reference
Ni-12 Al	773	4.1×10^{22}	8.4×10^{19}	488	0.21	[121]
Ni-7.5 Al-8.5 Cr	873	4.0×10^{22}	5.4×10^{21}	7	14.29	[22]
Ni-5.2 Al-14.2 Cr	873	3.2×10^{23}	5.9×10^{21}	54	1.85	[22]
Ni-6.5 Al-9.5 Cr	873	1.06×10^{23}	1.5×10^{20}	707	0.14	[30]
Ni-12.5 Al	823	1.34×10^{22}	2.03×10^{20}	66	1.52	Present study

Considering pre-existing short-range ordering of solute clusters in the as-quenched samples; therefore $J_{CNT}^{st} = 1.34 \times 10^{22} \text{ m}^{-3} \text{s}^{-1}$ is an absolute maximum upper bound to the true value of J_{CNT}^{st} . As we reported for concentrated Ni-Al-Cr alloys, solute clusters can form and diffuse faster than monomers [61]. To obtain the correct value of J_{CNT}^{st} , we can use the effective number of nucleation sites per unit volume, $N_{effective}$, to replace the total number of possible nucleation sites per unit volume to address the faster diffusing solute clusters. In this study, $N_{effective}$ is only about 1.52% of the value of N . Additionally, the calculated value of J_{CNT}^{st} is strongly affected by the value of W_R^* , Eq. (18). W_R^* is in turn proportional to $(\sigma^{\gamma/\gamma'})^3$, Eq. (15). Hence, our measured values of 28.55 ± 1.61 and $29.94 \pm 1.69 \text{ mJ m}^{-2}$ for $\sigma^{\gamma/\gamma'}$ (Section 4.7) result in a range of values for W_R^* , and therefore a possible range of values of J_{CNT}^{st} (1.44×10^{21} to $3.57 \times 10^{22} \text{ m}^{-3} \text{s}^{-1}$), which implies a factor of 25 between the largest and smallest value of J_{CNT}^{st} , due solely to the uncertainty in the value $\sigma^{\gamma/\gamma'}$. Additionally, the value of $\sigma^{\gamma/\gamma'}$ requires correction terms for $\gamma'(\text{L1}_2)$ -precipitates with small values of $\langle R(t) \rangle$, which represent contributions from precipitate edges (which are a function of $\langle R(t) \rangle$), and from vertices (a constant) [122–125].

4.2.2.2. Regime II: concomitant $\gamma'(\text{L1}_2)$ -precipitate nucleation and growth. Regime II, Fig. 5b, begins at the end of regime I (nucleation regime), $t = 0.25 \text{ h}$, and ends when $N_v(t)$ achieves a maximum value at 1 h [$N_v(t = 1 \text{ h}) = 6.87 \pm 0.12 \times 10^{23} \text{ m}^{-3}$]. The maximum value of $N_v(t)$ correlates with the maximum value of $f(t)$, $39.68 \pm 2.81\%$, because there are more $\gamma'(\text{L1}_2)$ -precipitates available to form necks between precipitates. Regime II can be differentiated from regime I because $N_v(t)$ increases in both regimes I and II, but $\phi_\gamma(t)$ and $\langle R(t) \rangle$ are approximately constant in regime I, whereas they are increasing continuously in regime II, Fig. 5.

4.2.2.3. Regime III: concurrent growth and coarsening via the coagulation and coalescence mechanism. Because $N_v(t)$ is decreasing continuously throughout regime III, we may conclude that nucleation is no longer occurring. It is distinguished from regime IV in that growth and coarsening are occurring mainly through the coagulation and coalescence mechanism rather than the evaporation-condensation mechanism (*the large eat the small*), as assumed for the mean-field LS and Calderon-Voorhees-Murray-Kostorz (CVMK) coarsening models, Section 4.5.

4.2.2.4. Regime IV: quasi-stationary coarsening. Regime IV in Fig. 5b displays a temporal exponent of $q = -0.75 \pm 0.03$, which is smaller in magnitude than the LS and CVMK value of -1 . We emphasize, however, that the slope of this curve, and hence the value of q is increasing continuously in regime IV in accord with the Kampmann-Wagner N(umerical) model. We anticipate that aging the alloy for a longer time at 823 K (550°C), for example to $10,000 \text{ h}$, or at an aging temperature $>973 \text{ K}$ ($>700^\circ\text{C}$), would yield a value of $q = -1$ [88]. Our earlier studies of Ni-6.5 Al-9.5 Cr at.% aged at 873 K [30]

and Ni-10 Al-8.5 Cr-2 Ru at.% aged at 1073 K (800°C) [31] both display a value of -1 for q , implying that a higher aging temperature and therefore a larger inter-diffusivity is needed to achieve a true stationary-coarsening regime. Ternary alloys have, however, a much smaller value of ΔF_{el} : Ni-5.2 Al-14.2 Cr, Ni-7.5 Al-8.5 Cr, and Ni-6.5 Al-9.5 Cr at.% have ΔF_{el} values at 873 K (600°C) of 1.1×10^5 , 2.5×10^6 , and $2.7 \times 10^6 \text{ kJ m}^{-3}$, respectively, compared to $4.96 \times 10^6 \text{ kJ m}^{-3}$ for our current alloy, Ni-12.5 Al at.%, at 823 K (550°C), which helps the ternary alloys to achieve a value of $q = -1$ faster than this binary alloy due to the much smaller lattice parameter misfit and elastic strain energy in these ternary Ni-Al-Cr alloys [22,30].

This value of $q = -1$ differs from a mathematical equation posited by Ardell [126] and Xiao and Haasen [121], who employed the relationship $N_v(t) = c_1 t^{-1} - c_2 t^{-4/3}$, where c_1 and c_2 are given in Refs. [121,126]. This relationship is not generally applicable, as shown by Marqusee and Ross [59,127,128]. In Ref. [127] Marqusee and Ross demonstrate rigorously that as time approaches infinity $\langle R(t) \rangle$ becomes proportional to $t^{1/3}$ and $N_v(t)$ is proportional to t^{-1} . If one adds mathematical corrections terms to these laws, as was posited by Ardell, and Xiao and Haasen, then it is necessary to add higher order terms to all the pertinent physical quantities, $\langle R(t) \rangle$, $N_v(t)$, $\Delta C_i^\gamma(t)$, and the PSDs, which are then no longer unique [127].

4.2.3. Temporal evolution of the mean radius, $\langle R(t) \rangle$, of $\gamma'(\text{L1}_2$ structure)-precipitates

Fig. 5c provides very strong evidence that Ni-12.5 Al aged at 823 K (550°C) follows a diffusion-limited coarsening process. The value of $1/p$ obtained from the data in Figs. 5c and 0.34 ± 0.02 , is in excellent agreement with the LS and CVMK coarsening model's value, $1/p = 1/3$ [32,33]. Because these coarsening models are based on a diffusion-limited coarsening process, we conclude that our Ni-12.5 Al at.% alloy aged at 823 K (550°C) obeys a diffusion-limited, rather than an interface-limited (source-sink-limited), coarsening process; the latter has a temporal exponent of 0.5 [33]. We find additional 3-D APT data and monovacancy-mediated LKMC₁ simulation evidence against a source-sink-limited (interface-controlled) coarsening mechanism in the temporal evolution of $\delta(t)$, Section 4.6.

4.3. Temporal evolution of the compositions of the $\gamma(\text{f.c.c.})$ - $\gamma'(\text{L1}_2$ structure)-phases

Our 3-D APT and monovacancy-mediated LKMC₁ results for Ni-12.5 Al at.% aged at 823 K (550°C) both indicate that the $\gamma(\text{f.c.c.})$ - and $\gamma'(\text{L1}_2)$ -precipitate-phases are initially supersaturated in Al, and that the compositions of both phases evolve temporally with increasing aging time; this is in contrast to standard review articles and text-book thermodynamic models, which state that the composition of a second-phase remains at or is very close to its

equilibrium value during phase separation. And hence the compositional evolution we observe suggests that we are detecting non-standard phase separation [129,130], which is distinctly different from standard pictures of phase separation (or phase decomposition or precipitation).

The initial 3-D APT value of $C_{Al}^{\gamma}(t)$, 12.50 ± 3.12 at.% at 0.08 h of aging, is equal to the nominal composition of the alloy, Ni-12.5 Al at.%. This was anticipated, as the corresponding initial value of $\phi_{\gamma}(t)$ is small, 0.002 ± 0.001 %. Therefore, in a solid-solution of essentially pure γ (f.c.c.), the small number density of γ' (L1₂)-precipitates doesn't alter significantly the value of $C_{Al}^{\gamma}(t)$. With increasing aging time, $\phi_{\gamma}(t)$ is increasing, and concomitantly $C_{Al}^{\gamma}(t)$ is moving toward the left along the horizontal tie-line, indicated by a bold black-arrow in Fig. 2, headed for the γ/γ plus γ' solvus curve. At 4096 h $C_{Al}^{\gamma}(t)$ is 11.25 ± 0.29 at.%, APT measurement, which agrees closely with the solvus curves due to Ma and Ardell [71] and Dupin et al. [70], which are identical in the temperature range 773 K (500 °C) to 900 K (627 °C), Fig. 2.

The γ' (L1₂)-precipitates nucleate far to the right of the $(\gamma + \gamma')/\gamma'$ solvus curve, and from the measured initial 3-D APT value of $C_{Al}^{\gamma}(t)$ (33.97 ± 49 at.%) the first observed precipitates are in the [γ' (L1₂) plus NiAl(B2)] phase-field, Fig. 2, if this portion of the existing phase diagram is correct. The value of $C_{Al}^{\gamma}(t)$ at the earliest aging time, 0.08 h, is determined using a proximity histogram [84,85] for 16 effective γ' (L1₂)-precipitates (due to a small number density, $N_v(t = 0.08h) = 0.08 \pm 0.02 \times 10^{23} \text{ m}^{-3}$), and thus its uncertainty is ± 8.49 at.% Al, implying that $C_{Al}^{\gamma}(t)$ could be as small as 25.48 at.% Al at 0.08 h, albeit with a very small probability. 3-D APT cannot determine a crystal structure and powder x-ray diffraction experiments performed at the Advanced Photon Source, Argonne National Laboratory, for the earliest aging times (0.08–0.25 h), were also inconclusive for determining the crystal structure because of the small number of atoms in all the precipitates and their small number density. They have, however, a high probability of having a γ' (L1₂)-structure at 0.08 h due to their coherency with the γ (f.c.c.)-matrix.

A possible reason for the γ' (L1₂)-precipitates nucleating in the [γ' (L1₂) plus NiAl(B2)] phase field, Figs. 2s and 6, can be explained by the Gibbs-Thomson-Freundlich effect [131], which yields the solute concentration at a matrix/precipitate heterophase-interface as a function of its radius, R . The Calderon-Voorhees-Murray-Kostorz (CVMK) [40,41] model permits modifying the Gibbs-Thomson equation for a general nonideal non-dilute solution utilizing a capillary length, l^a , which predicts the equilibrium concentration of Al on the γ (f.c.c)-side at the γ (f.c.c.)/ γ' (L1₂) heterophase-interface, $C_{Al}^{\gamma,eq}(R)$. The supersaturation of Al in the γ (f.c.c)-phase, $\Delta C_{Al}^{\gamma}(R)$, is given by:

Table 7

Curvature of the molar Gibbs free energy of mixing with respect to concentration in the γ (f.c.c.-) phase, $G_m^{\gamma''}$, and interfacial free energy, $\sigma_{\gamma/\gamma'}$, calculated using two different thermodynamic databases and the rate constants listed in Table 6 for a Ni-12.5 Al at.% alloy aged at 823 K. The two databases result in approximately equal values of $\sigma_{\gamma/\gamma'}$.

Thermo-Calc Database	Saunders [68]	Dupin et al. [70]
$G_m^{\gamma''}$	$283,056 \text{ J mol}^{-1}$	$269,968 \text{ J mol}^{-1}$
$\sigma_{\gamma/\gamma'}$	$29.94 \pm 1.69 \text{ mJ m}^{-2}$	$28.55 \pm 1.61 \text{ mJ m}^{-2}$

$$\Delta C_{Al}^{\gamma}(R) = C_{Al}^{\gamma,eq}(R) - C_{Al}^{\gamma,eq}(\infty) = \frac{2V_m^{\gamma'}\sigma_{\gamma/\gamma'}}{(C_{Al}^{\gamma,eq}(\infty) - C_{Al}^{\gamma,eq}(R))G_m^{\gamma}} \cdot \frac{1}{R} \quad (21)$$

where $C_{Al}^{\gamma,eq}(R)$ is a function of the γ' (L1₂)-precipitate radius, R , and the left-hand term of equation (21) is the capillary length, l^a , defined by equation (4). The supersaturation, $\Delta C_{Al}^{\gamma}(R)$, depends on the inverse of R , implying that as R increases $C_{Al}^{\gamma,eq}(R) \rightarrow C_{Al}^{\gamma,eq}(\infty)$. Employing a molar volume of the γ' (L1₂)-precipitate phase, $V_m^{\gamma'}$, value of $1.16 \times 10^{-29} \text{ m}^3$ [132,133], and taking $\sigma_{\gamma/\gamma'}$ and G_m^{γ} to be $28.55 \pm 1.61 \text{ mJ m}^{-2}$ and $269,968 \text{ J mol}^{-1}$, respectively (Section 4.7 and Tables 6 and 7), the supersaturation of the γ (f.c.c)-matrix-phase, $\Delta C_{Al}^{\gamma}(R)$, at 0.08 h with a mean radius, $\langle R(t = 0.08 \text{ h}) \rangle = 0.79 \pm 0.20 \text{ nm}$, increases to 1.56 ± 0.52 at.%, which agrees with our 3-D APT experimental data. The γ (f.c.c) matrix's Al concentration evolves from 12.5 at.% at $t = 0$, increases slightly to 12.74 at.% and then decreases continuously to the equilibrium concentration, 11.14 ± 0.32 at.%.

Alternatively, the γ' (L1₂)-precipitates nucleate from a highly supersaturated Al concentration; $C_{Al}^{\gamma}(t = 0.08h) = 33.97 \pm 8.49$, and decrease continuously to a concentration of 25.93 ± 0.45 at. % with a mean radius of $R(t) = 1.47 \pm 0.03 \text{ nm}$ at 1 h of aging. This unanticipated large Al supersaturation is explained by a smaller value of the second derivative of the Gibbs free energy in the γ' (L1₂)-phase; $G_m^{\gamma'} = 82,875 \text{ J mol}^{-1}$ [70] at the equilibrium Al concentration ($C_{Al}^{\gamma,eq}(\infty) = 23.14 \pm 0.47$ at.%), which is $\sim 1/3$ of the value of G_m^{γ} in γ (f.c.c)-matrix, $269,968 \text{ J mol}^{-1}$. This implies that the capillary length for a γ' (L1₂)-precipitate in eq (21) is larger than for the γ (f.c.c)-matrix; therefore, the supersaturation, $\Delta C_{Al}^{\gamma}(R)$, is greater by a factor of three compared to its value in the γ (f.c.c)-matrix.

4.4. Temporal evolution of the γ' (L1₂)-precipitate size distributions (PSDs)

The material for this section can be found in Supplement E2.

4.5. Temporal evolution of the fraction of γ' (L1₂)-precipitates interconnected by necks, $f(t)$, and the minimum edge-to-edge distances, $\langle \lambda_{edge-edge}(t) \rangle$, between neighboring γ' (L1₂)-precipitates

In Section 4.2.2 we demonstrate that the temporal evolution of γ' (L1₂)-precipitates in Ni-12.5 Al at.% aged at 823 K is divided into four distinct regimes, Fig. 5b: (I) nucleation from 0.08 to 0.25 h; (II) nucleation and growth from 0.25 to 1 h; (III) growth and coarsening from 1 to 64 h; and (IV) quasi-stationary coarsening beyond 64 h. Our results for the temporal evolution of $f(t)$ and $\langle \lambda_{edge-edge}(t) \rangle$ prove that coagulation and coalescence is the dominant mechanism of γ' (L1₂)-precipitate evolution in regime III, which is in agreement with the vacancy-mediated LKMC₁ simulations.

Table 6

Relevant physical constants measured or calculated from experimental data (3-D atom-probe tomography) utilized to determine the interfacial free energy, $\sigma_{\gamma/\gamma'}$, at 823 K (550 °C) for Ni-12.5 Al at.%, and the diffusivity, $D_{coarsening}^{experiment}$.

Measured Constant	Value
$V_m^{\gamma'}$	$6.98 \times 10^{-6} \text{ m}^3 \text{ mol}^{-1}$
$C_{Al}^{\gamma,eq}(\infty)$	11.14 ± 0.32 at.%
$C_{Al}^{\gamma,eq}(\infty)$	23.14 ± 0.47 at.%
K	$2.09 \pm 0.10 \times 10^{-31} \text{ m}^3 \text{ s}^{-1}$
κ^{γ}	$0.25 \pm 0.01 \text{ s}^{1/3}$
$\kappa^{\gamma'}$	$0.68 \pm 0.03 \text{ s}^{1/3}$
$F(\phi_{\gamma'})$	1.8308
l^a	$1.23 \pm 0.07 \times 10^{-11} \text{ m}$
$D_{coarsening}^{experiment}$	$2.51 \pm 0.14 \times 10^{-21} \text{ m}^2 \text{ s}^{-1}$

Table 8

Solute diffusion coefficient pre-factors, D_0 , and activation energies, Q , for Al solute diffusion in Ni and Ni_3Al and Ni solute diffusion in Ni_3Al , taken from different experimental and computational archival sources. Also listed are the resulting values of D_{Al} for Al in Ni and Ni_3Al at 823 K and D_{Ni} in Ni_3Al at 823 K.

D_0 ($10^{-4} \text{ m}^2 \text{s}^{-1}$)	Q (kJ mol $^{-1}$)	Temperature Range (K)	D at 823 K ($\times 10^{-21} \text{ m}^2 \text{s}^{-1}$)	Reference	Techniques
Inter-diffusivities in Ni-Al alloys					
1.87	267.8	1372–1553	1.83	[144]	Kirkendall diffusion couples
Al diffusivity in Ni					
1.10	249.1	1073–1243	17.01	[148]	Electron diffraction
10.0	272.0	1273–1573	5.44	[149]	Electron probe microanalysis
1.0	260	914–1212	3.14	[150]	Vapor deposition; SIMS
7.1	276.6	898–973	1.97	[41]	Analysis of coarsening data
29	290	1273–1623	1.14	[151]	Laser Induced Breakdown Spectrometry
7.52	284	1173–1673	0.71	[145]	Mobility database
9.03	282	600–900	1.14	[152]	First-principles calculations
Al diffusivity in Ni_3Al					
3.7	223.85	1418–1585	2292.17	[153]	MD simulations
0.00505	243	1173–1473	0.19	[154]	Electron probe microanalysis
Ni diffusivity in Ni_3Al					
3.23	302	1195–1523	0.02	[155]	Electron probe microanalysis
0.00917	116	1400–1550	3.98×10^7	[156]	MD simulations
0.00583	108	1300–1550	8.14×10^7	[157]	MD simulations

4.5.1. The evolution of the fraction of $\gamma'(\text{L1}_2)$ -precipitates interconnected by necks $f(t)$

The monovacancy-mediated LKMC₁ results for $f(t)$ are slightly greater than the 3-D APT results for $f(t)$ in regime I, and slightly smaller than the 3-D APT results for $f(t)$ in regimes II–IV, Fig. 8a. This is most likely due to the differences in how the $\gamma'(\text{L1}_2)$ -precipitates are defined in each case. The $\gamma'(\text{L1}_2)$ -precipitates in the 3-D APT reconstructions are delineated using iso-concentration surfaces, Section 2.3, while $\gamma'(\text{L1}_2)$ -precipitates in the monovacancy-mediated LKMC₁ simulations are delineated using iso-ordering surfaces [22,62]. This implies that the 3-D APT results define a neck as a region between two $\gamma'(\text{L1}_2)$ -precipitates with approximately the same composition as the interior of the $\gamma'(\text{L1}_2)$ -precipitates, while monovacancy-mediated LKMC₁ results have the added requirement that this region also exhibits L1_2 ordering. Because monovacancy-mediated LKMC₁ simulations have a more rigid criterion for what is or is not a neck than the 3-D APT results, the monovacancy-mediated LKMC₁ results for $f(t)$ are smaller than the 3-D APT results for $f(t)$ in regimes II–IV. Experimental 3-D APT analyses find necks present solely when connecting two $\gamma'(\text{L1}_2)$ -precipitates to one another. The analyses of atomic configurations generated by monovacancy-mediated LKMC₁ simulations find essentially two $\gamma'(\text{L1}_2)$ -precipitates interconnected by one neck. (Occasionally the presence of three $\gamma'(\text{L1}_2)$ -precipitates interconnected by two necks is detected.) Our prior studies have also shown definitively the presence of L1_2 ordered-necks utilizing 3-D APT data [18,29].

4.5.2. The temporal evolution of the edge-to-edge distances, $\langle \lambda_{\text{edge}-\text{edge}}(t) \rangle$, between neighboring $\gamma'(\text{L1}_2)$ -precipitates, and the flux diffusion mechanism

For the 3-D APT data and LKMC₁ simulation results, for aging times <0.25 h, the edge-to-edge distance $\langle \lambda_{\text{edge}-\text{edge}}(t) \rangle$ is greater than 200 nm, and $f(t)$ is less than 5%, Fig. 8, which implies that the evaporation-condensation coarsening mechanism (“the large precipitates eat the small precipitates”) prevails because the $\gamma'(\text{L1}_2)$ -

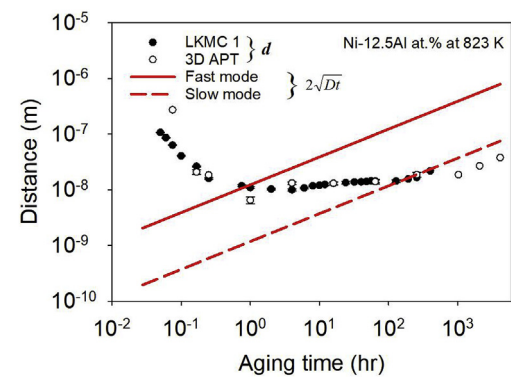


Fig. 12. The temporal evolution of the edge-to-edge inter-precipitate spacing d (open circles): 3-D APT; bold symbols LKMC₁) in this alloy compared to the root-mean-square (RMS) diffusion distance ($2\sqrt{Dt}$) for the fast and the slow modes of the diffusion-limited model. Fast mode.

precipitates are not sufficiently close to one another to form L1_2 -ordered necks. For aging times greater than 256 h, the evaporation-condensation mechanism once again triumphs, as $f(t)$ is $<20\%$ and $\langle \lambda_{\text{edge}-\text{edge}}(t) \rangle$ is >18 nm; the latter is too large a distance to permit $\gamma'(\text{L1}_2)$ -precipitates to form L1_2 -ordered necks as a result of their overlapping concentration profiles.

To interpret our results further we utilize some basic concepts of macroscopic diffusion theory, which are reviewed briefly in **Supplement F**. The model Ni-Al alloy is specified by the concentrations of the atomic species, C_{Ni} , C_{Al} , and the concentration of monovacancies, C_V ; the sum of the three concentrations is unity. Since the $\gamma'(\text{L1}_2)$ -precipitates are coherent with the γ (f.c.c.)-matrix, lattice sites are conserved locally during phase-separation. Because the mean edge-to-edge distance, $\langle \lambda_{\text{edge}-\text{edge}}(t) \rangle$, between $\gamma'(\text{L1}_2)$ -precipitates is small compared to the mean inter-dislocation

Table 9

The diffusion matrix and its related eigen-modes for the Ni-12.5 Al at.% alloy aged at 823 K (550 °C) as calculated employing LKMC₁. The calculations are performed in the γ (f.c.c.)-phase solid-solution with equilibrium composition, Ni-10.76 Al at.%. The last column displays the coupling between the Ni and Al flux, $J_{\text{Ni}}/J_{\text{Al}}$, required to build a $\gamma'(\text{L1}_2)$ -precipitate with its equilibrium $J_{\text{Ni}}/J_{\text{Al}}$ composition from the supersaturated solutions.

Diffusion matrix ($\text{m}^2 \text{s}^{-1}$)	Eigen diffusion coefficients ($\text{m}^2 \text{s}^{-1}$)	Diffusion flux coupling $J_{\text{Ni}}/J_{\text{Al}}$	$J_{\text{Ni}}/J_{\text{Al}}$ Equilibrium
$\begin{pmatrix} 1.14 \times 10^{-22} & 2.95 \times 10^{-21} \\ -2.95 \times 10^{-21} & 1.13 \times 10^{-20} \end{pmatrix}$	$D_{\text{fast}} = 1.05 \times 10^{-20}$ $D_{\text{slow}} = 9.58 \times 10^{-22}$	$J_{\text{Ni}}^{\text{fast}}/J_{\text{Al}}^{\text{fast}} = 0.082 \pm 0.02$ $J_{\text{Ni}}^{\text{fast}}/J_{\text{Al}}^{\text{fast}} = -12.3 \pm 0.5$	0.121

spacing, which is of the order of $<10^3$ nm (one micron), lattice sites are conserved at all space and time scales, which are given by the mean spacing between dislocations and the time it takes for vacancies to diffuse that distance.

To understand the precipitation mechanism, a clear way to visualize diffusional couplings is to search for the eigenmodes (eigenvalues and eigenvectors) of the diffusion matrix in LKMC₁ simulations. We obtain two distinguishable diffusion modes from the diffusion matrix in the LKMC₁ simulations listed in Table 9: fast and slow modes. The fast eigenvector of the diffusion matrix is such that: $\tilde{J}^{fast} = -D^{fast} \nabla C^{fast} Q^{-1}$ and the eigen-diffusion vector is thus $\nabla C^{fast} = -Q \tilde{J}^{fast} / D^{fast}$. For the fast eigen-mode, the eigen-diffusivity coefficient is $1.05 \times 10^{-20} \text{ m}^2 \text{ s}^{-1}$ (D^{fast}) with a diffusion flux coupling given by $\tilde{J}_{Ni}^{fast} / \tilde{J}_{Al}^{fast} = 0.082 \pm 0.02$. For the slow eigenmode, the eigen-diffusivity coefficient is $9.58 \times 10^{-22} \text{ m}^2 \text{ s}^{-1}$ (D^{slow}) with a diffusion flux coupling given by $\tilde{J}_{Ni}^{slow} / \tilde{J}_{Al}^{slow} = -12.3 \pm 0.5$. The fast eigen-diffusivity is one order of magnitude larger than the slow eigen-diffusivity. For a concentration profile to evolve at the scale of the mean edge-to-edge inter-precipitate distance, $\langle \lambda_{edge-edge}(t) \rangle$, (in the coarsening regime), a time $\tau = \frac{\langle \lambda_{edge-edge}(t) \rangle^2}{4D}$, is required. Fig. 12 displays the temporal evolution of the mean edge-to-edge inter-precipitate distance, $\langle \lambda_{edge-edge}(t) \rangle$, the root-mean square diffusion distance using the 3-D APT inter-diffusion diffusivity, and the two diffusional flux-eigen-modes. Furthermore, Fig. 12 demonstrates that the fast eigen-mode contributes to growth during the first hour of aging (across the edge-to-edge distance). For LKMC₁, within the Ni-based γ (f.c.c.)-matrix (Ni is a slow diffuser compared to Al), the fast eigen-mode (that is, the dominant eigen-flux) is mainly Al, which drags Ni in the same direction; $\tilde{J}_{Ni}^{fast} / \tilde{J}_{Al}^{fast} = 0.082 \pm 0.02$, while the coupling between the Ni and Al fluxes, J_{Ni}/J_{Al} , required to create a γ' (L1₂)-precipitate with its equilibrium composition from the supersaturated solutions with a deviation 0.121. Coagulation and coalescence of γ' (L1₂)-precipitates occurs mainly approximately at the aging time when the fast eigen-mode achieves the mean edge-to-edge inter-precipitate diffusion distance. The slow eigen-mode becomes significant only after 400 h (across the edge-to-edge distance), well within the coarsening regime. Inside the γ' (L1₂)-precipitates, the weaker slow eigen-mode is mainly Ni, which drags small amounts of Al out of the γ' (L1₂)-precipitates: $\tilde{J}_{Ni}^{slow} / \tilde{J}_{Al}^{slow} = -12.3 \pm 0.5$. At 400 h the γ' (L1₂)-precipitate morphology changes from spheroidal-to-cuboidal, which corresponds to the slow eigen-diffusion mode becoming dominant.

4.6. Temporal evolution of the compositional interfacial widths, $\delta(t)$, between the γ (f.c.c.)- and γ' (L1₂)-phases

Our results for $\delta(t)$, from both 3-D APT experiments and monovacancy-mediated LKMC₁ simulations, demonstrate that $\delta(t)$ decreases with increasing aging time, but it never achieves a value of zero, in contrast to the trans-interface diffusion-coarsening (TIDC) model, which hypothesizes the exact opposite temporal behavior for $\delta(t)$ for which there is neither experimental nor modeling evidence.

4.6.1. The temporal evolution of the concentration profiles between the γ (f.c.c)- and γ' (L1₂)-phases

The temporal evolution of the concentration profiles between the γ (f.c.c)- and γ' (L1₂)-phases, determined by 3-D APT experiments for our Ni-12.5 Al at.% alloy, are displayed in Fig. 9. For the γ (f.c.c)-matrix the Ni concentrations profiles an excess appears at 4 h (open green-triangles), which increases at 16 h (open purple-

inverse triangles), starts to saturate at 256 h (open blue-diamonds), and finally almost disappears completely at 4096 h (open black-square). Conversely, the Al concentration profiles exhibit a depletion commencing at 4 h, which increases at 16 h, increases further at 256 and disappears completely at 4096 h. Contrarywise, for the γ' (L1₂)-precipitates the Ni concentration profiles exhibit a strong depletion at 0.25 h (open red-circles), which commences to decrease at 4 h, continues to decrease at 16 h, then decreases further at 256 h and finally becomes almost flat at 4096 h. Conversely, the Al concentration profiles commence with a strong excess at 0.25 h, which decreases at 4 h, then decreases further at 16 h and 256 h, and finally at 4096 h it is almost flat.

For three different ternary Ni-Al-Cr alloys we find analogously similar results. In these studies, an excess of Ni and Cr atoms and a depletion of Al atoms are initially observed in the interfacial region between the two phases [12,13,16,18,22,23,30,61,62,134]. The differences between the binary and ternary concentration profiles occur because for ternary alloys diffusion of Al into the γ' (L1₂)-precipitates is opposed by the diffusion of Cr and Ni into the γ (f.c.c.)-matrix. Additionally, we emphasize strongly that in both the Ni-Al and the Ni-Al-Cr alloys an additional component, monovacancies, is necessary to understand the diffusive fluxes between the γ (f.c.c)- and γ' (L1₂)-phases. Hence, binary alloys are three-component systems and ternary alloys are four-component systems because of the necessity of including the monovacancy as a component in modeling the temporal evolution of the concentration profiles. None of the results we find concerning the temporal evolution of the concentration profiles in the Ni-Al and Ni-Al-Cr alloys are intuitively obvious nor are they accounted for in mean-field coarsening models.

4.6.2. The {100}-type compositional interfacial width $\delta(t)$

The average value of $\delta(t)$ for {100}-type interfaces decreases with increasing aging time, Fig. 10a, which is consistent with the Cahn-Hilliard [129,130] and Martin models [135], and with prior 3-D APT studies [27,95,136].

Our monovacancy-mediated LKMC₁ results for the Ni-12.5 Al at.% alloy agree with the 3-D APT results for $t > 1$ h, but slightly overestimate the value of $\delta(t)$ for $t < 1$ h. Both our 3-D APT experimental and our monovacancy-mediated LKMC₁ simulation results are in disagreement with the trans-interface diffusion-coarsening (TIDC) model for binary alloys, which hypothesizes the following ansatz: "... if $\delta(t) \propto \langle R(t) \rangle^m$ ($0 \leq m \leq 1$) over a certain range of particle (precipitate) radii, the kinetics of particle (precipitate) growth and solute depletion will obey equations of the type $\langle R(t) \rangle^n \propto t$ and $C_i^{\gamma,ff}(t) - C_i^{\gamma,eq}(\infty) \propto t^{1/n}$, where $n = m + 2$ " [42,137]. Additionally, the authors state, "We cannot yet provide theoretical justification for the relationship $\delta(t) \propto \langle R(t) \rangle^m$, though we believe that such a relationship is credible, given the ragged nature of the γ (f.c.c.)/ γ' (L1₂) interface" [137]. In strong contrast, our results demonstrate that $\delta(t)$ decreases with increasing aging time, but it never becomes equal to zero, and Fig. 10b establishes that $\delta(t)$ decreases continuously with increasing $\langle R(t) \rangle$. The data in Fig. 10b fit a $\langle R(t) \rangle^m$ -type relationship, where m is -0.47 ± 0.03 , which disagrees with the ansatz that is the basis of the TIDC model: that is, $0 \leq m \leq 1$. The value $m = -0.47 \pm 0.03$ implies a value of 1.53 for n ($n = m + 2$), which in turn implies that the TIDC model predicts $\langle R(t) \rangle \propto t^{0.65}$. The latter relationship is in disagreement with the experimental 3-D APT results, Fig. 5c, and therefore this ansatz is incorrect for the Ni-Al system. Additionally, our prior results for Ni-12.5 Al and Ni-13.4 Al at.% aged at 823 K (550 °C), and 873 K (600 °C), where we find that $\delta(t)/\langle R(t) \rangle$ varies to first order as $\langle R(t) \rangle^{-1}$ [95], and also for Ni-10.0 Al-8.5 Cr-2.0 Ta at.% aged at 1073 K (800 °C) [27], provides additional proof that $\delta(t)$ decreases

with increasing aging time and increasing $\langle R(t) \rangle$.

We have previously demonstrated that the $\delta(t)$ values for three Ni–Al–Cr alloys decrease with increasing aging time by performing monovacancy-mediated LKMC₁ simulations, which include monovacancy-solute binding energies to 4th NN distances [45,61] and atom-atom interactions that also extend to 4th NN, Section 2.5. Monovacancy-mediated LKMC₂ simulations of the same Ni–Al–Cr alloys produce $\delta(t)$ values that are smaller than those produced by the monovacancy-mediated LKMC₁ simulations, because the monovacancy-solute binding energy only extends to the 1st NN distance for monovacancy-mediated LKMC₂, Supplement Table C1, even though the atom-atom interactions extend to 4th NN distances. Nevertheless, these $\delta(t)$ values still decrease with increasing aging time. Thus, the $\delta(t)$ values are determined by atomistic interactions that include non-zero monovacancy–solute binding energies. The atom-atom and monovacancy-solute binding energies are not functions of aging time or $\langle R(t) \rangle$. We therefore conclude that the compositional thickness of the transition layer between the γ (f.c.c)- and γ' (L₁₂)-phases is affected by the details of the diffusion mechanism; indeed, decreasing the range of monovacancy-solute interactions (as does the monovacancy-mediated LKMC₂ parameterization), modifies the coupling between the solute and solvent fluxes. The interaction distance over which atom-atom and monovacancy-solute interactions occur, Ξ , is a constant for a given alloy at a specified temperature. Therefore, the ratio $\Xi/\langle R(t) \rangle$ must decrease with increasing aging time, because Ξ is a constant and $\langle R(t) \rangle$ is continuously increasing, which is the case for an alloy becoming quasi-stationary, Fig. 10b. Parenthetically, in the continuum limit, Ξ is the origin of the so-called gradient energy coefficient in the Cahn–Hilliard equation [129,130].

In this study, the vacancy–solute binding energy is also examined by employing only first NN distances up to an aging time of 400 h, which we refer to as LKMC₂ as discussed above. Technically, we replace ϵ_{V-S}^k with ϵ_{V-Ni}^k when $k > 1$, where k is the NN shell. We have demonstrated that the growth and coarsening mechanism switches from coagulation-coalescence to the classic evaporation-condensation mechanism during early aging times (<4 h). The maximum fraction of the precipitates connected by necks using LKMC₂ decreases to 9.6%, compared to 36% using LKMC₁. The compositional thickness of the transition layer using LKMC₂, between the γ (f.c.c)- and γ' (L₁₂)-phases, is thinner than those utilizing LKMC₁; about 43–56% when compared to the LKMC₁ value, during the early nucleation and coarsening regimes. The composition of the precipitates starts from 25.6 at.% Al using LKMC₂, compared to 30.13 at.% Al employing LKMC₁. This significant difference in the Al concentrations during the precipitation process demonstrates the effects of strong couplings between the solute and solvent fluxes, which have much larger values for the off-diagonal terms of the diffusion matrix when utilizing LKMC₁.

4.7. The interfacial free energy of the γ (f.c.c)/ γ' (L₁₂) interface $\sigma^{\gamma/\gamma'}$

The calculated values of $\sigma^{\gamma/\gamma'}$ from 3-D APT coarsening rate constant data are in good agreement with our first-principles calculations for the {100}-type interface [45,138].

4.7.1. The measured interfacial free energy of the γ (f.c.c)/ γ' (L₁₂) interface determined from coarsening experiments and their comparison with first-principles calculations of $\sigma^{\gamma/\gamma'}$

Table 6 summarizes the calculated constants that are necessary to determine $\sigma^{\gamma/\gamma'}$ utilizing Eq. (8). Each quantity listed is determined directly from our experimental 3-D APT data with the exceptions of $V_m^{\gamma'}$ [67] and $F(\phi_{\gamma'})$ [40,59], which are calculated. Table 7 displays values of $G_m^{\gamma'}$ taken from two thermodynamic databases in Thermo-Calc [68–70] and the resulting values of $\sigma^{\gamma/\gamma'}$ obtained for

each $G_m^{\gamma'}$. The values of $\sigma^{\gamma/\gamma'}$ obtained employing the Saunders and Dupin et al. $G_m^{\gamma'}$ values are 29.94 ± 1.69 and 28.55 ± 1.61 mJ m⁻², respectively, which are equal to one another within error.

We utilized first-principles calculations to calculate $\sigma^{\gamma/\gamma'}$ of the γ (Ni)/ γ' (Ni₃Al) interface for {100}-, {110}-, and {111}-type interfaces [45]. Of these three $\sigma^{\gamma/\gamma'}$ first-principles values the one for the {100}-type interface is the correct one to compare with the experimental results, because with increasing aging time the γ' (L₁₂)-precipitates develop a cuboidal morphology, Fig. 4e–f, and therefore the {100}-type plane is where the γ (Ni)/ γ' (Ni₃Al)-interface lies. The first-principles calculated values of $\sigma^{\gamma/\gamma'}$ at 823 K (600 °C) are 23.11, 26.83, and 28.42 mJ m⁻² for the {100}-, {110}-, and {111}-type interfaces, respectively [45], which are in the range of the experimental values, 26.94–31.16 mJ m⁻², within experimental error. Using a second-cluster expansion technique [46], Woodward et al. calculated $\sigma^{\gamma/\gamma'}$ values of 16.5, 17.7, and 15.9 mJ m⁻² for the {100}-, {110}-, and {111}-type interfaces, respectively. Because the cluster expansion technique overestimates the temperature by 335 K, these values are calculated at a scaled temperature of 488 K (215 °C) instead of our actual aging temperature, 823 K (550 °C). Ji-Cheng Zhao et al. used dual-anneal diffusion multiples to generate a composition gradient and adjusted the interfacial energy value in simulations using the classical nucleation and growth theories as implemented in the Kampmann–Wagner numerical (KWN) model. They obtained the average Ni/Ni₃Al(L₁₂) interfacial energy is 14 mJ m⁻² at 873 K [139], which is 10 mJ m⁻² lower than the ones we calculated. We found that the interfacial free energy decreases with increasing temperature due to entropy effects [45].

4.7.2. Equilibrium morphology of γ' (L₁₂)-precipitates

Because the equilibrium morphology of γ' (L₁₂)-precipitates is determined by the effects of $\sigma^{\gamma/\gamma'}$ and the elastic strain energy we calculate the ratio of the elastic strain-energy contribution to the $\sigma^{\gamma/\gamma'}$ contribution, L , for determining the morphology of γ' (L₁₂)-precipitates using [140–142]:

$$L = \frac{\mu \gamma \epsilon^2 \langle R(t) \rangle}{\sigma^{\gamma/\gamma'}} \quad (22)$$

where ϵ is the lattice parameter misfit between the two phases. The value of L is 0.02 for the shortest aging time (0.08 h), implying that the morphology of γ' (L₁₂)-precipitates is dominated by the interfacial free energies, $\sigma^{\gamma/\gamma'}$ at 0.08 h. The values of L are 0.29 at 2607 h and 0.40 at 4096 h, respectively, indicating that the elastic strain energy plays a larger role in the morphology of γ' (L₁₂)-precipitates with increasing aging times, but it is still smaller than the role played by $\sigma^{\gamma/\gamma'}$ at 4096 h.

4.8. Comparison of the diffusivities calculated from atom-probe tomography experimental data and monovacancy-mediated lattice-kinetic Monte Carlo simulation results

Our results demonstrate that $D_{\text{experiment}}^{\text{coarsening}}$, derived from coarsening rate constants determined from APT experiments, is equal to the inter-diffusion coefficient \tilde{D} for the binary Ni-12.5 Al at.% system, Eq. (23), and as determined by monovacancy-mediated LKMC₁ simulations.

4.8.1. Relationship of the interdiffusivity, \tilde{D} , determined by monovacancy-mediated LKMC₁ simulations and the diffusivity determined from the coarsening experiments $D_{\text{experiment}}^{\text{coarsening}}$

The monovacancy-mediated LKMC₁ $D_{\text{Al}}^{\gamma-\text{matrix}}$ values are $2.22 \pm 0.38 \times 10^{-21}$, $2.18 \pm 0.36 \times 10^{-21}$, and

$1.62 \pm 0.26 \times 10^{-21} \text{ m}^2 \text{ s}^{-1}$ for 1, 4, and 400 h of aging, respectively. And the $D_{\text{Ni}}^{\gamma\text{-matrix}}$ values are $1.11 \pm 0.14 \times 10^{-22}$, $1.02 \pm 0.38 \times 10^{-22}$, and $0.99 \pm 0.14 \times 10^{-22} \text{ m}^2 \text{ s}^{-1}$ for 1, 4, and 400 h of aging, respectively. The value of \tilde{D} is related to the individual diffusivities of Ni and Al by Ref. [98]:

$$\tilde{D} = C_{\text{Al}} D_{\text{Ni}} + C_{\text{Ni}} D_{\text{Al}} \quad (23)$$

Using Eq. (23) and the calculated values of $D_{\text{Al}}^{\gamma\text{-matrix}}$ and $D_{\text{Ni}}^{\gamma\text{-matrix}}$ yield values of $3.75 \pm 0.31 \times 10^{-22}$, $3.62 \pm 0.31 \times 10^{-22}$, and $2.90 \pm 0.25 \times 10^{-22} \text{ m}^2 \text{ s}^{-1}$ for \tilde{D} , for 1, 4, and 400 h of aging, respectively, for $C_{\text{Al}} = 0.125$ and $C_{\text{Ni}} = 0.875$ atomic fraction. The values of \tilde{D} for 1 and 4 h are equal, within experimental error, to $D_{\text{experiment}}^{\text{coarsening}}$, $2.51 \pm 0.14 \times 10^{-21} \text{ m}^2 \text{ s}^{-1}$ (Section 4.8.2), and the \tilde{D} value at 400 h is 15% of $D_{\text{experiment}}^{\text{coarsening}}$. Thus, there is semi-quantitative agreement between $D_{\text{experiment}}^{\text{coarsening}}$ and the monovacancy-mediated LKMC₁ values for 1, 4, and 400 h. In the course of phase separation, C_{Al} decreases while C_{Ni} increases, which improves the agreement between the APT and LKMC₁ results. In conclusion, $D_{\text{experiment}}^{\text{coarsening}}$ is properly described by \tilde{D} , which can be measured or calculated utilizing either a Kirkendall diffusion couple or LKMC₁ simulations, respectively. There are not, unfortunately, Kirkendall diffusion couple measurements available for $C_{\text{Al}} = 0.125$ and $C_{\text{Ni}} = 0.875$ atomic fraction.

Fig. 11a, c, and 11e show that the monovacancy spends the majority of its time inside the two $\gamma'(\text{L1}_2)$ -precipitates and the neck region connecting them at 1 and 4 h, Section 3.7, while the $\gamma'(\text{L1}_2)$ -precipitates are continuously ordering. Diffusion occurring in the $\gamma'(\text{L1}_2)$ -precipitates and the connecting necks, as demonstrated by the monovacancy-mediated LKMC₁ simulations, is not taken into account in any of the existing mean-field diffusion-limited models of coarsening, nor is the presence of the interconnecting neck(s) between $\gamma'(\text{L1}_2)$ -precipitates, which is at the origin of the coagulation-coalescence mechanism of coarsening. Because of correlation effects [51,143], the monovacancy is not able to diffuse as fast in the partially ordered $\gamma'(\text{L1}_2)$ -precipitates nor in the partially ordered L1_2 neck regions connecting the $\gamma'(\text{L1}_2)$ -precipitates, as it is in the disordered $\gamma(\text{f.c.c.})$ -matrix. This is demonstrated quantitatively in Table 3, where $D_i^{\gamma\text{-matrix}}$ is always larger than either $D_i^{\gamma'\text{-precipitates}}$ or D_i^{necks} .

For both Ni and Al interchanges with the monovacancy, D_i^{superell} is closer to $D_i^{\gamma\text{-matrix}}$ than it is to $D_i^{\gamma'\text{-precipitates}}$ for the values of $\phi_{\gamma'}(t)$ for the $\gamma'(\text{L1}_2)$ -precipitates at 1 and 4 h, 2.87 ± 0.05 and $3.64 \pm 0.16\%$, respectively. The volume fraction of the partially ordered necks connecting the $\gamma'(\text{L1}_2)$ -precipitates is significantly smaller than $\phi_{\gamma'}(t)$. While the value of $\phi_{\gamma'}(t)$ at 400 h is closer to its equilibrium value, 13.48%, implying that approximately 90% of the volume of the alloy is the $\gamma(\text{f.c.c.})$ -matrix, and D_i^{superell} is closer to $D_i^{\gamma\text{-matrix}}$ than it is to $D_i^{\gamma'\text{-precipitates}}$.

4.8.2. Calculation of the diffusivity, $D_{\text{experiment}}^{\text{coarsening}}$, from atom-probe tomography coarsening data and the inter-diffusivity, \tilde{D} , of Al and Ni

The calculated value of $D_{\text{experiment}}^{\text{coarsening}}$ from the 3-D APT coarsening rate data are compared with the existing archival values of the diffusivities in the Ni-Al system, Table 8, and is specifically compared to the inter-diffusion coefficient, \tilde{D} , measured experimentally by Swalin and Martin [144], because it is the only existing inter-diffusivity for a Ni-Al alloy.

Eq. (9) is used to calculate $D_{\text{experiment}}^{\text{coarsening}}$ for this alloy, which is $2.51 \pm 0.14 \times 10^{-21} \text{ m}^2 \text{ s}^{-1}$ at 823 K (550 °C). Table 8 summarizes

the archival values of the pre-factor, D_0 , and the activation energy for diffusion, Q , for diffusion in the Ni-Al system (solute diffusivity and inter-diffusivity), plus the applicable temperature ranges and experimental or computational methods utilized. Table 8 also lists the resulting diffusivity at 823 K (550 °C) for each reference utilizing:

$$D_{\text{experiment}}^{\text{coarsening}} = D_0 \exp\left(-\frac{Q}{k_B T}\right) \quad (24)$$

Most experimental research on the Ni-Al system was performed at higher temperatures than the current research, so calculations of $D_{\text{experiment}}^{\text{coarsening}}$ at 823 K (550 °C) are based on an extrapolation.

Our measured value of $D_{\text{experiment}}^{\text{coarsening}} = 2.51 \pm 0.14 \times 10^{-21} \text{ m}^2 \text{ s}^{-1}$ is 27% greater than the value measured by Swalin and Martin, $1.83 \times 10^{-21} \text{ m}^2 \text{ s}^{-1}$ [144], for $C_{\text{Al}} = 7 \times 10^{-3}$ at.fr., utilizing a Kirkendall effect couple to measure \tilde{D} for Al and Ni. We attribute this difference to the higher value of C_{Al} in our Ni-Al alloy: 12.5 versus 0.7 at. % Al. Additionally, $D_{\text{experiment}}^{\text{coarsening}}$ is 72% larger than the value for the Al diffusivity calculated by C. Campbell et al. [145], $0.71 \times 10^{-21} \text{ m}^2 \text{ s}^{-1}$, based on her mobility database.

5. Summary and conclusions

The temporal evolution of a binary Ni-12.5 Al at.% alloy undergoing phase-separation at 823 K (550 °C) is investigated using 3-D atom-probe tomography (APT), monovacancy-mediated lattice-kinetic Monte Carlo (LKMC₁) simulations, microhardness measurements, and some transmission electron microscopy (TEM). The main results obtained as a function of aging time include: (1) Vickers microhardness of bulk specimens of the alloy; (2) $\gamma'(\text{L1}_2)$ -precipitate morphology; (3) $\gamma'(\text{L1}_2)$ -precipitate volume fraction, $\phi_{\gamma'}(t)$; (4) $\gamma'(\text{L1}_2)$ -precipitate number density, $N_v(t)$; (5) mean radius of $\gamma'(\text{L1}_2)$ -precipitates, $\langle R(t) \rangle$; (6) Al concentration of the $\gamma(\text{f.c.c.})$ -phase, $C_{\text{Al}}^{\gamma}(t)$; (7) Al concentration of the $\gamma'(\text{L1}_2)$ -phase, $C_{\text{Al}}^{\gamma'}(t)$; (8) supersaturation of Al in the $\gamma(\text{f.c.c.})$ -phase, $\Delta C_{\text{Al}}^{\gamma}(t)$; (9) supersaturation of Al in the $\gamma'(\text{L1}_2)$ -phase, $\Delta C_{\text{Al}}^{\gamma'}(t)$; (10) partitioning coefficient of Al between the $\gamma'(\text{L1}_2)$ - and $\gamma(\text{f.c.c.})$ -phases, $K_{\text{Al}}^{\gamma'/\gamma}(t)$; (11) partitioning coefficient of Ni between the $\gamma'(\text{L1}_2)$ - and $\gamma(\text{f.c.c.})$ -phases, $K_{\text{Ni}}^{\gamma'/\gamma}(t)$; (12) $\gamma'(\text{L1}_2)$ -precipitate size distributions (PSDs); (13) fraction of $\gamma'(\text{L1}_2)$ -precipitates interconnected by necks, $f(t)$; (14) minimum edge-to-edge distance between $\gamma'(\text{L1}_2)$ -precipitates, $\langle \lambda_{\text{edge-edge}}(t) \rangle$; and (15) interfacial compositional width between the $\gamma(\text{f.c.c.})$ - and $\gamma'(\text{L1}_2)$ -phases, $\delta(t)$, for the {100}-type interface. Experimental atom-probe tomographic measurements and monovacancy-mediated LKMC₁ simulation results are used to calculate kinetic and thermodynamic quantities: (i) including the quasi-stationary nucleation currents, $J_{\text{APT}}^{\text{st}}$ and $J_{\text{LKMC}}^{\text{st}}$; (ii) the diffusivity, $D_{\text{experiment}}^{\text{coarsening}}$; and (iii) the interfacial free energy of the $\gamma(\text{f.c.c.})/\gamma'(\text{L1}_2)$ {100}-type interface, $\sigma^{\gamma/\gamma'}$. This is the most complete and detailed study of the temporal evolution of an alloy undergoing a first-order phase transformation made to date and it is possible because of correlative research employing 3-D APT in combination with monovacancy-mediated LKMC₁ simulations, which permits us to explore this four-dimensional space (positions of atoms in 3-D and chemical identity of each atom) in great detail. LKMC₁ includes monovacancy-solute binding energies and atom-atom interaction energies out to the fourth nearest-neighbor (NN) position, whereas LKMC₂ is only out to first NN positions for the same energies.

- The four regimes of the $\gamma'(\text{L1}_2)$ -phase's temporal evolution are: (I) quasi-stationary nucleation; (II) concomitant nucleation and growth; (III) concurrent growth and coarsening; and (IV) quasi-stationary coarsening, which are identified utilizing 3-D APT and monovacancy-mediated LKMC₁ simulations, Fig. 5.
- Monovacancy-mediated LKMC₁ simulations, which include monovacancy-solute binding energies out to 4th nearest-neighbor distances (Supplement Table C1) were performed, through 800 h, in parallel with the 3-D APT experiments. In Figs. 2, 5–7 and 9–11 we compare the LKMC₁ and 3-D APT results in detail.
- The $\gamma'(\text{L1}_2)$ -precipitates undergo a spheroidal-to-cuboidal transition prior to 1024 h, Fig. 4a–f. Additionally, the TEM micrographs, Fig. 4g, at 1024 h of aging, demonstrate that the $\gamma'(\text{L1}_2)$ -precipitates are well aligned along a <100>-type-direction, which is indicative of so-called rafting. The 3-D APT and TEM results provide collectively a reasonably complete picture of the morphological evolution of the $\gamma'(\text{L1}_2)$ -precipitates.
- The Vickers microhardness values are approximately constant, while the $\gamma'(\text{L1}_2)$ -precipitates are nucleating (<4 h of aging), and the values increase with increasing aging time, Fig. 3, because $\phi_{\gamma'}(t)$ is concomitantly increasing and the edge-to-edge distance between precipitates is decreasing. Hence, this alloy's strength is governed by the volume fraction of $\gamma'(\text{L1}_2)$ -precipitates and the main strengthening mechanism is most likely Orowan dislocation-looping at room temperature.
- As demonstrated by 3-D APT experiments, $\phi_{\gamma'}(t) = 0$ in the as-quenched state, implying that the alloy consists of only the $\gamma(\text{f.c.c.})$ -phase at $t = 0$.
- The initial value of $\phi_{\gamma'}(t)$ at 0.08 h is $0.002 \pm 0.001\%$, Fig. 5a, and it increases with increasing aging time toward its equilibrium value of 13.48% at 4096 h, where $\phi_{\gamma'}(t = 4096 \text{ h})$ is $12.80 \pm 1.40\%$: Fig. 2.
- The number density, $N_v(t)$, is $7.88 \times 10^{21} \text{ m}^{-3}$ for the earliest aging time (0.08 h), Fig. 5b. This value increases with increasing aging time as additional $\gamma'(\text{L1}_2)$ -precipitates nucleate in the $\gamma(\text{f.c.c.})$ -matrix, and it achieves a maximum value of $6.87 \times 10^{23} \text{ m}^{-3}$ after 1 h of aging, representing an increase of two orders of magnitude in $N_v(t)$. With further aging, $N_v(t)$ decreases as new $\gamma'(\text{L1}_2)$ -precipitates cease nucleating and existing $\gamma'(\text{L1}_2)$ -precipitates grow and coarsen via a coagulation and coalescence mechanism, which we have found previously for three different Ni-Al-Cr alloys [12,13,16–19,22,23,26,29,30]. The temporal exponent, q , of $N_v(t)$ for Ni-12.5 Al at.% aged at 823 K in the range 64–4096 h is 0.75 ± 0.03 , which is slowly approaching the predicted value for regime IV of $q = -1$, Fig. 5b. This implies that we should have had aged for 10,000 h or more.
- Based on the total solute atoms as possible nucleation sites, the stationary nucleation current, $J_{\text{CNT}}^{\text{st}}$, calculated assuming classical nucleation theory (CNT), is $1.34 \times 10^{22} \text{ m}^{-3} \text{ s}^{-1}$, which is 66 times greater than the 3-D APT value, $J_{\text{APT}}^{\text{st}}$, of $2.03 \times 10^{20} \text{ m}^{-3} \text{ s}^{-1}$ and 57 times greater than the monovacancy-mediated LKMC₁ value, $J_{\text{LKMC}}^{\text{st}}$, of $2.37 \times 10^{20} \text{ m}^{-3} \text{ s}^{-1}$, Table 5. This calculated value of $J_{\text{CNT}}^{\text{st}}$ employed a chemical driving force for phase separation, ΔF_{ch} , which is obtained from first-principles calculations, rather than utilizing the standard classical thermodynamic methodology [88,115]. Additionally, we use $\sigma^{\gamma'/\gamma} = 28.55 \pm 1.61 \text{ mJ m}^{-2}$, as determined from the 3-D APT coarsening experiments, Section 4.7, for calculating $J_{\text{CNT}}^{\text{st}}$, Section 4.2.2.1.
- Due to pre-existing solute short-range order in the $\gamma(\text{f.c.c.})$ -matrix, the effective number of nucleation sites per unit volume, $N_{\text{effective}}$, is proposed to replace the total number of possible nucleation sites per unit volume to address the faster diffusing solute clusters. In this study, $N_{\text{effective}}$ is only about 1.52% of the value of N . This approach for calculating $J_{\text{CNT}}^{\text{st}}$ yields better agreement with $J_{\text{CNT}}^{\text{st}}$ than the classical approaches [88,115] and it engages a value of $\sigma^{\gamma'/\gamma}$, which we measured from the coarsening experiments utilizing 3-D APT.
- $\gamma'(\text{L1}_2)$ -precipitates are detected at the earliest aging time studied experimentally (0.08 h) with an $\langle R(t) \rangle$ value of $0.79 \pm 0.20 \text{ nm}$, Fig. 5c. After aging for 4096 h, $\langle R(t) \rangle$ increases to $14.59 \pm 1.62 \text{ nm}$, which is 18.5 times greater than its initial value. The temporal exponent for $\langle R(t) \rangle$ in the quasi-stationary coarsening regime is $1/p = 0.34 \pm 0.02$, which is consistent with the Lifshitz-Slyozov (LS) and Calderon-Voorhees-Murray-Kostorz (CVMK) mean-field diffusion-limited coarsening models's value of 1/3, thereby indicating diffusion-limited coarsening behavior. The rate constant, K , for $\langle R(t) \rangle$ is $2.09 \pm 0.10 \times 10^{-31} \text{ m}^3 \text{ s}^{-1}$.
- $\gamma'(\text{L1}_2)$ -precipitates nucleate with an initial high Al-supersaturation (excess of Al), and then proceed to become less supersaturated in Al with increasing aging time, Fig. 6. Both supersaturations, $\Delta C_{\text{Al}}^{\gamma}(t)$ and $\Delta C_{\text{Al}}^{\gamma'}(t)$, decrease continuously with increasing aging time. The longest aging time studied (4096 h) is insufficient for the alloy to achieve complete equilibrium at 823 K (550 °C). Nevertheless, the temporal exponent for the decrease in supersaturations in both phases is $1/r = 0.33 \pm 0.03$. And this value is also in agreement with the LS and CVMK mean-field diffusion-limited coarsening models, which is completely consistent with diffusion-limited coarsening, but it is inconsistent with the trans-interface diffusion-controlled (TIDC) coarsening model.
- The calculated rate constants for $\Delta C_{\text{Al}}^{\gamma}(t)$ and $\Delta C_{\text{Al}}^{\gamma'}(t)$, κ^{γ} and $\kappa^{\gamma'}$, are 0.25 ± 0.01 and $0.68 \pm 0.03 \text{ s}^{1/3}$, respectively. Because of the difficulties involved with measuring $C_{\text{Al}}^{\gamma}(t)$ and $C_{\text{Al}}^{\gamma'}(t)$ with methods other than 3-D APT, it is rare to find reliable measured values for κ^{γ} and $\kappa^{\gamma'}$ in the archival literature.
- Utilizing the LS and CVMK equations for the supersaturations, the equilibrium concentrations of the $\gamma(\text{f.c.c.})$ - and $\gamma'(\text{L1}_2)$ -phases are 11.14 ± 0.32 and $23.14 \pm 0.47 \text{ at.\%}$, respectively, extrapolated to infinite aging time, Fig. 6a–b.
- The temporal evolution of $C_{\text{Al}}^{\gamma}(t)$ approaches the solvus curves due to Ma and Ardell [71] and Dupin et al. [70], and $C_{\text{Al}}^{\gamma'}(t)$ approaches the solvus curve due to Saunders [68] for the partial Ni-Al phase diagram, as indicated by the heavy black horizontal arrows, Fig. 2.
- In contrast to the conventional wisdom that the second-phase $\gamma'(\text{L1}_2)$ -precipitates should nucleate with a composition that is close to its equilibrium composition [88], we find that they nucleate far from their equilibrium composition and then evolve temporally toward it, Fig. 2, where the Al concentration trajectory is denoted by the heavy black horizontal arrow. This indicates that nucleation is occurring by a different mechanism than the one commonly found in review articles and text books on phase transformations, as opposed to what we find experimentally using atom-probe tomography and vacancy-mediated lattice kinetic Monte Carlo simulations.
- The PSDs evolve temporally with increasing aging time from a narrow PSD in regime I to a wider distribution in regimes II and III, and finally to a narrow PSD in regime IV, Supplement E. This last PSD is similar to the model PSDs generated from the Akaiwa-Voorhees (AV) simulations and Brailsford-Wynblatt (BW) calculations based on our semi-quantitative observations of PSDs.
- The maximum value of $N_v(t)$, Fig. 5b, corresponds to the maximum value of the fraction of $\gamma'(\text{L1}_2)$ -precipitates interconnected by necks, $f(t)$, $39.68 \pm 2.81\%$, and the minimum value of $\langle \lambda_{\text{edge-edge}}(t) \rangle$, Fig. 8. These results are consistent with a coagulation and coalescence mechanism of coarsening, over a range of aging times about the maximum value of $f(t)$, as

- opposed to the classic evaporation-condensation (“the large precipitates eat the small precipitates”) mechanism, which is assumed implicitly in the LS and CVMK mean-field models.
- Monovacancy-mediated LKMC₁ simulations are in reasonably good agreement with all the experimental 3-D APT data for all measured physical quantities, Figs. 2 and 5–7 and 10 and 11.
 - The monovacancy-mediated LKMC₁ results are consistent with experimental results for $C_{Al}^{\gamma'}(t)$, Fig. 6b, but underestimate slightly $C_{Al}^{\gamma'}(t)$ for >0.25 h, Fig. 6a. Additionally, the monovacancy-mediated LKMC₁ results are in better agreement with the experimental 3-D APT data for aging times longer than 4 h.
 - An important assumption of the so-called trans-interface diffusion-coarsening (TIDC) model concerns the dependence of the {100}-type interfacial composition width, $\delta(t)$, on aging time and $\langle R(t) \rangle$, which are in disagreement with our 3-D APT experimental and monovacancy-mediated LKMC₁ simulation results for this Ni–Al alloy. The value of $\delta(t)$ decreases with increasing time (t) and $\langle R(t) \rangle$, Fig. 10, as $t^{-0.08 \pm 0.01}$ and $\langle R(t) \rangle^{-0.47 \pm 0.03}$, respectively, but it is never equal to zero.
 - The value of $\sigma^{\gamma/\gamma'}$ is calculated from the coarsening data using the rate constants determined from the experimental 3-D APT data for $\langle R(t) \rangle$ and $\Delta C_{Al}^{\gamma}(t)$, and two different values of the curvature of the molar Gibbs free energy of mixing with respect to concentration, yielding values of 29.94 ± 1.69 and 28.55 ± 1.61 mJ m⁻², respectively, which are consistent with our prior first-principles calculations performed on the $\gamma(\text{Ni})/\gamma'(\text{Ni}_3\text{Al})$ interface for the {100}-, {110}- and {111}-type interfaces at 823 K (550 °C) [45].
 - In this work, all experimental determined values of $\sigma^{\gamma/\gamma'}$ are in a disagreement with the approach Ardell's used (1995) because they utilized a value of a diffusivity from the archival literature, rather than determining both values independently of one another.
 - The diffusivity, $D_{\text{coarsening}}^{\text{experiment}}$, at 823 K (550 °C) is calculated using the rate constants obtained from the 3-D APT experiments for $\langle R(t) \rangle$ and $\Delta C_{Al}^{\gamma}(t)$, which is equal to $2.51 \pm 1.41 \times 10^{-21}$ m² s⁻¹.
 - The calculated diffusivities for the entire monovacancy-mediated LKMC₁ supercell, $D_{Al}^{\text{supercell}}$ and $D_{Ni}^{\text{supercell}}$, are determined by counting the number of jumps of Al or Ni atoms for exchanges with the monovacancy. For both Al and Ni, $D_i^{\text{supercell}}$ is closer to the calculated $D_i^{\gamma-\text{matrix}}$ value than it is to the calculated $D_i^{\gamma'-\text{precipitates}}$ because of the small values of $\phi_{\gamma'}(t)$ of the $\gamma'(\text{L}_{12})$ -precipitates at 1 and 4 h, 2.14 ± 0.26 and $2.12 \pm 0.26\%$, respectively. The volume fraction of the partially ordered necks connecting the $\gamma'(\text{L}_{12})$ -precipitates is smaller than $\phi_{\gamma'}(t)$. The value of $\phi_{\gamma'}(t)$ at 400 h is close to its equilibrium value, 13.48%, where approximately 90% of the volume is the $\gamma(\text{f.c.c.})$ -matrix, and thus $D_i^{\text{supercell}}$ is closer to $D_i^{\gamma-\text{matrix}}$ than it is to $D_i^{\gamma'-\text{precipitates}}$.
 - $D_{\text{coarsening}}^{\text{experiment}}$ is equal to the value of the inter-diffusion coefficient, \bar{D} , derived from the monovacancy-mediated LKMC₁ calculations for 1 and 4 h, $3.75 \pm 0.31 \times 10^{-22}$ and $3.62 \pm 0.31 \times 10^{-22}$ m² s⁻¹, respectively, while \bar{D} at 400 h, $2.90 \pm 0.25 \times 10^{-22}$ m² s⁻¹, is 15% of $D_{\text{coarsening}}^{\text{experiment}}$. From this semi-quantitative agreement between simulations and experiment we conclude that our experimental results permit us to use the experimentally obtained coarsening rate constants to calculate the inter-diffusion coefficient of Ni and Al in our binary Ni-12.5 Al at.% alloy. This is an important result, as there are many examples in the archival literature where the proper diffusivity for coarsening is stated to be \bar{D} , without any indication as to whether it is an inter-diffusivity or the diffusivity of the solute species.

Acknowledgements

This research was supported by the National Science Foundation, Division of Materials Research grant number DMR-1610367 001; Profs. Diana Farkas and Gary Shiflet, grant monitors. Atom-probe tomography was performed at the Northwestern University Center for Atom-Probe Tomography (NUCAPT). The LEAP tomograph at NUCAPT was purchased and upgraded with grants from the NSF MRI (DMR-0420532) and ONR-DURIP (N00014–0400798, N00014–0610539, N00014–0910781, N00014–1712870) programs. NUCAPT received support from the MRSEC program (NSF DMR-1720139) at the Materials Research Center, the SHyNE Resource (NSF ECCS-1542205), and the Initiative for Sustainability and Energy (ISEN) at Northwestern University. A portion of this research was performed at the DuPont-Northwestern-Dow Collaborative Access Team (DND-CAT) located at Sector 5 of the Advanced Photon Source (APS). DND-CAT is supported by E.I. DuPont de Nemours & Co., The Dow Chemical Company, and Northwestern University. Use of the APS, an Office of Science User Facility operated for the U.S. Department of Energy (DOE) Office of Science by Argonne National Laboratory, was supported by the U.S. DOE under Contract No. DE-AC02-06CH11357. Ms. Elizaveta Y. Plotnikov was initially supported by a W. P. Murphy Fellowship and then this NSF grant. Drs. Zugang Mao and Sung-II Baik were partially supported by this NSF grant. Prof. Yongsheng Li was supported by the China Scholarship Council. Dr. Mehmet Yildirim was supported by the Scientific HR Development Program of the Middle East Technical University. The authors thank Dr. Nathalie Dupin for generous access to her Thermo-Calc data for the partial Ni–Al phase diagram. Additionally, Prof. Peter Voorhees is thanked for stimulating and enlightening discussions and Prof. Pascal Bellon is thanked for important discussions concerning correlated diffusion effects. Dr. C. E. Campbell is thanked for discussion for Ni mobility databases. Mr. Pavithran Maris (visiting undergraduate scholar) is thanked for helping with atom-probe tomography experiments during the summer of 2013; Dr. John Thompson for calculating the AV PSD and $F(\phi_{\gamma'})$; and Ms. Yanyan (Ashley) Huang for assisting in performing Vickers microhardness measurements.

Appendix A. Supplementary data

Supplementary data to this article can be found online at <https://doi.org/10.1016/j.actamat.2019.03.016>.

References

- [1] C.D. Desforges, Metals and alloys for high-temperature applications current status and future prospects, Rev. Int. Hautes Temp. 14 (1977) 28–45.
- [2] Y. Mishima, S. Ochiai, N. Hamao, M. Yodogawa, T. Suzuki, Solid-solution hardening of nickel - role of transition-metal and B-subgroup solutes, T. Jpn. I. Met. 27 (1986) 656–664.
- [3] J.W. Cahn, F. Larche, A simple-model for coherent equilibrium, Acta Metall. 32 (1984) 1915–1923.
- [4] J. Svoboda, E. Gamsjager, F.D. Fischer, P. Fratzl, Application of the thermodynamic extremal principle to the diffusional phase transformations, Acta Mater. 52 (2004) 959–967.
- [5] J. Svoboda, F.D. Fischer, P. Fratzl, E. Kozeschnik, Modelling of kinetics in multi-component multi-phase systems with spherical precipitates - I: theory, Mat Sci Eng a-Struct 385 (2004) 166–174.
- [6] E. Kozeschnik, J. Svoboda, P. Fratzl, F.D. Fischer, Modelling of kinetics in multi-component multi-phase systems with spherical precipitates - II: numerical solution and application, Mat Sci Eng a-Struct 385 (2004) 157–165.
- [7] K. Kawasaki, Y. Enomoto, Statistical-theory of Ostwald ripening with elastic field interaction, Phys. Stat. Mech. Appl. 150 (1988) 463–498.
- [8] C. Schmuck, F. Danoix, P. Caron, A. Hauet, D. Blavette, Atomic scale investigation of ordering and precipitation processes in a model Ni-Cr-Al alloy, Appl. Surf. Sci. 94–95 (1996) 273–279.
- [9] C. Schmuck, P. Caron, A. Hauet, D. Blavette, Ordering and precipitation of γ' -phase in low supersaturated Ni-Cr-Al model alloy: an atomic scale investigation, Philos. Mag. A 76 (1997) 527–542.

- [10] C. Pareige-Schmuck, F. Soisson, D. Blavette, Ordering and phase separation in low supersaturated Ni-Cr-Al alloys: 3D atom probe and Monte Carlo simulation, *Mat. Sci. Eng. A-Struct.* 250 (1998) 99–103.
- [11] C. Pareige, F. Soisson, G. Martin, D. Blavette, Ordering and phase separation in Ni-Cr-Al: Monte Carlo simulations vs. Three-dimensional atom probe, *Acta Mater.* 47 (1999) 1889–1899.
- [12] C.K. Sudbrack, K.E. Yoon, Z. Mao, R.D. Noebe, D. Isheim, D.N. Seidman, Temporal evolution of nanostructures in a model nickel-base superalloy: experiments and simulations, electron microscopy, in: J.R. Weertman, et al. (Eds.), *Its role in Materials science, 2003*, pp. 43–50. San Diego, CA, USA, TMS.
- [13] C.K. Sudbrack, D. Isheim, R.D. Noebe, N.S. Jacobson, D.N. Seidman, The influence of tungsten on the chemical composition of a temporally evolving nanostructure of a model Ni-Al-Cr superalloy, *Microsc. Microanal.* 10 (2004) 355–365.
- [14] C.K. Sudbrack, *Decomposition Behavior in Model Ni-Al-Cr-X Superalloys: Nanostructural Evolution and Compositional Pathways*, Northwestern University, 2004. Ph.D. thesis.
- [15] K.E. Yoon, C.K. Sudbrack, R.D. Noebe, D.N. Seidman, The temporal evolution of the nanostructures of model Ni-Al-Cr and Ni-Al-Cr-Re superalloys, *Z. Metallkd.* 96 (2005) 481–485.
- [16] C.K. Sudbrack, R.D. Noebe, D.N. Seidman, Temporal evolution of sub-nanometer compositional profiles across the γ/γ' interface in a model Ni-Al-Cr superalloy, in: J.M. Howe, D.E. Laughlin, J.K. Lee, U. Dahmen, W.A. Soffa (Eds.), *Solid-Solid Phase Transformations in Inorganic Materials 2005*, vol. 2, The Minerals, Metals & Materials Society, 2005, pp. 543–548.
- [17] C.K. Sudbrack, R.D. Noebe, D.N. Seidman, Direct observations of nucleation in a nondilute multicomponent alloy, *Phys. Rev. B* 73 (2006) 212101.
- [18] C.K. Sudbrack, K.E. Yoon, R.D. Noebe, D.N. Seidman, Temporal evolution of the nanostructure and phase compositions in a model Ni-Al-Cr alloy, *Acta Mater.* 54 (2006) 3199–3210.
- [19] C.K. Sudbrack, R.D. Noebe, D.N. Seidman, Compositional pathways and capillary effects during isothermal precipitation in a nondilute Ni-Al-Cr alloy, *Acta Mater.* 55 (2007) 119–130.
- [20] K.E. Yoon, R.D. Noebe, D.N. Seidman, Effects of rhenium addition on the temporal evolution of the nanostructure and chemistry of a model Ni-Cr-Al superalloy. II: analysis of the coarsening behavior, *Acta Mater.* 55 (2007) 1159–1169.
- [21] C.K. Sudbrack, T.D. Ziebell, R.D. Noebe, D.N. Seidman, Effects of a tungsten addition on the morphological evolution, spatial correlations and temporal evolution of a model Ni-Al-Cr superalloy, *Acta Mater.* 56 (2008) 448–463.
- [22] C. Booth-Morrison, J. Weninger, C.K. Sudbrack, Z. Mao, R.D. Noebe, D.N. Seidman, Effects of solute concentrations on kinetic pathways in Ni-Al-Cr alloys, *Acta Mater.* 56 (2008) 3422–3438.
- [23] C. Booth-Morrison, R.D. Noebe, D.N. Seidman, Effects of a tantalum addition on the morphological and compositional evolution of a model Ni-Al-Cr superalloy, *Superalloys 2008* (2008) 73–79.
- [24] C. Booth-Morrison, Z.G. Mao, R.D. Noebe, D.N. Seidman, Chromium and tantalum site substitution patterns in Ni_3Al (L_1_2) γ' -precipitates, *Appl. Phys. Lett.* 93 (2008).
- [25] Y. Zhou, Z. Mao, C. Booth-Morrison, D.N. Seidman, The partitioning and site preference of rhenium or ruthenium in model nickel-based superalloys: an atom-probe tomographic and first-principles study, *Appl. Phys. Lett.* 93 (2008).
- [26] Y. Zhou, C. Booth-Morrison, D.N. Seidman, On the field evaporation behavior of a model Ni-Al-Cr superalloy studied by picosecond pulsed-laser atom-probe tomography, *Microsc. Microanal.* 14 (2008) 571–580.
- [27] C. Booth-Morrison, R.D. Noebe, D.N. Seidman, Effects of tantalum on the temporal evolution of a model Ni-Al-Cr superalloy during phase decomposition, *Acta Mater.* 57 (2009) 909–920.
- [28] C. Booth-Morrison, *Nanoscale Studies of the Early Stages of Phase Separation in Model Nickel-Aluminum-Chromium-X Superalloys*, Northwestern University, 2009. Ph.D. thesis.
- [29] Y. Zhou, *Phase Separation on a Subnanoscale in Model Ni-Al-Cr-Based Superalloys*, Ph.D. thesis, Northwestern University, 2010.
- [30] C. Booth-Morrison, Y. Zhou, R.D. Noebe, D.N. Seidman, On the nanometer scale phase separation of a low-supersaturation Ni-Al-Cr alloy, *Philos. Mag. A* 90 (2010) 219–235.
- [31] Y. Zhou, D. Isheim, G. Hsieh, R.D. Noebe, D.N. Seidman, Effects of ruthenium on phase separation in a model $NiAlCrRu$ superalloy, *Philos. Mag. A* 93 (2013) 1326–1350.
- [32] I.M. Lifshitz, V.V. Slyozov, The kinetics of precipitation from supersaturated solid solutions, *J. Phys. Chem. Solids* 19 (1961) 35–50.
- [33] C. Wagner, Theorie der Alterung Niederschlägen durch Umlosen, *Z. Electrochem.* 65 (1961) 581–591.
- [34] A.J. Ardell, R. Nicholson, On modulated structure of aged Ni-Al alloys, *Acta Metall.* 14 (1966) 1295–1309.
- [35] D.H.B. Israel, M.E. Fine, Precipitation studies in Ni-10 At.Percent Ti, *Acta Metall.* 11 (1963) 1051–1059.
- [36] A.J. Ardell, Application of the theory of particle coarsening: the γ' precipitate in nickel-aluminum alloys, *Acta Metall.* 16 (1968) 511–516.
- [37] D.J. Chellman, A.J. Ardell, Coarsening of γ' precipitates at large volume fractions, *Acta Metall.* 22 (1974) 577–588.
- [38] T. Hirata, D.H. Kirkwood, The prediction and measurement of precipitate number densities in a nickel-6.05 wt.% aluminum alloy, *Acta Metall.* 25 (1977) 1425–1434.
- [39] C. Marsh, H. Chen, An in-situ X-ray diffraction study of precipitation from a supersaturated solid solution: the γ' precipitate in a nickel-12.5 at.% aluminum alloy, *Acta Metall. Mater.* 38 (1990) 2287–2298.
- [40] H.A. Calderon, P.W. Voorhees, J.L. Murray, G. Kostorz, Ostwald ripening in concentrated alloys, *Acta Metall. Mater.* 42 (1994) 991–1000.
- [41] A.J. Ardell, Interfacial free-energies and solute diffusivities from data on Ostwald ripening, *Interface Sci.* 3 (1995) 119–125.
- [42] A.J. Ardell, $A_1L_1_2$ interfacial free energies from data on coarsening in five binary Ni alloys, informed by thermodynamic phase diagram assessments, *J. Mater. Sci.* 46 (2011) 4832–4849.
- [43] D.L. Price, B.R. Cooper, Full-potential LMTO calculation of Ni/Ni_3Al interface energies, *Mater. Theory, Simulat. Parallel Algorith.* 408 (1996) 463–468.
- [44] Y. Mishin, Atomistic modeling of the γ and γ' -phases of the Ni-Al system, *Acta Mater.* 52 (2004) 1451–1467.
- [45] Z.G. Mao, C. Booth-Morrison, E. Plotnikov, D.N. Seidman, Effects of temperature and ferromagnetism on the γ -Ni/ γ' - Ni_3Al interfacial free energy from first principles calculations, *J. Mater. Sci.* 47 (2012) 7653–7659.
- [46] C. Woodward, A. van de Walle, M. Asta, D.R. Trinkle, First-principles study of interfacial boundaries in $Ni-Ni_3Al$, *Acta Mater.* 75 (2014) 60–70.
- [47] Y. Mishin, Calculation of the γ/γ' interface free energy in the Ni-Al system by the capillary fluctuation method, *Model Simul. Mater. Sc.* 22 (2014).
- [48] A. Baldan, Review progress in Ostwald ripening theories and their applications to nickel-base superalloys - Part I: Ostwald ripening theories, *J. Mater. Sci.* 37 (2002) 2171–2202.
- [49] A. Baldan, Review progress in Ostwald ripening theories and their applications to the gamma '-Precipitates in nickel-base superalloys - Part II - nickel-base superalloys, *J. Mater. Sci.* 37 (2002) 2379–2405.
- [50] D.J. Rowenhorst, J.P. Kuang, K. Thornton, P.W. Voorhees, Three-dimensional analysis of particle coarsening in high volume fraction solid-liquid mixtures, *Acta Mater.* 54 (2006) 2027–2039.
- [51] M. Marder, Correlations and Ostwald ripening, *Phys. Rev. A* 36 (1987) 858–874.
- [52] K. Trinckauf, J. Pesicka, C. Schlesier, E. Nembauch, The effect of the volume fraction on precipitate coarsening in nickel-base superalloys and aluminum lithium alloys, *Phys. Status Solidi A-Appl. Res.* 131 (1992) 345–355.
- [53] L. Rougier, A. Jacot, C.A. Gandin, P. Di Napoli, P.Y. Thery, D. Ponsen, V. Jaquet, Numerical simulation of precipitation in multicomponent Ni-base alloys, *Acta Mater.* 61 (2013) 6396–6405.
- [54] A.J. Ardell, Effect of volume fraction on particle coarsening. Theoretical considerations, *Acta Metall.* 20 (1972) 61–71.
- [55] A.D. Brailsford, P. Wynblatt, Dependence of Ostwald ripening kinetics on particle-volume fraction, *Acta Metall.* 27 (1979) 489–497.
- [56] N. Akaiwa, P.W. Voorhees, Late-stage phase-separation - dynamics, spatial correlations, and structure functions, *Phys. Rev. E* 49 (1994) 3860–3880.
- [57] S.P. Marsh, M.E. Glicksman, Kinetics of phase coarsening in dense systems, *Acta Mater.* 44 (1996) 3761–3771.
- [58] C.L. Chiang, *Statistical Methods of Analysis*, World Scientific Pub., River Edge, N.J., 2003.
- [59] J.A. Marqusee, J. Ross, Kinetics of phase transitions: theory of Ostwald ripening, *J. Chem. Phys.* 79 (1983) 373–378.
- [60] S.C. Yang, G.T. Higgins, P. Nash, Coarsening kinetics of solid and liquid silver particles in nickel, *Mater. Sci. Tech.-Lond* 8 (1992) 10–15.
- [61] Z.G. Mao, C.K. Sudbrack, K.E. Yoon, G. Martin, D.N. Seidman, The mechanism of morphogenesis in a phase-separating concentrated multicomponent alloy, *Nat. Mater.* 6 (2007) 210–216.
- [62] Z. Mao, C. Booth-Morrison, C.K. Sudbrack, G. Martin, D.N. Seidman, Kinetic pathways for phase separation: an atomic-scale study in Ni-Al-Cr alloys, *Acta Mater.* 60 (2012) 1871–1888.
- [63] R.A. Ricks, A.J. Porter, R.C. Ecob, The growth of γ' precipitates in nickel-base superalloys, *Acta Metall.* 31 (1983) 43–53.
- [64] A.C. Lund, P.W. Voorhees, The effects of elastic stress on microstructural development: the three-dimensional microstructure of a $\gamma+\gamma'$ alloy, *Acta Mater.* 50 (2002) 2585–2598.
- [65] J. Coakley, H. Basoalto, D. Dye, Coarsening of a multimodal nickel-base superalloy, *Acta Mater.* 58 (2010) 4019–4028.
- [66] T.M. Pollock, A.S. Argon, Directional coarsening in nickel-base single-crystals with high-volume fractions of coherent precipitates, *Acta Metall. Mater.* 42 (1994) 1859–1874.
- [67] A.B. Kamara, A.J. Ardell, C.N.J. Wagner, Lattice misfits in four binary Ni-base γ/γ' alloys at ambient and elevated temperatures, *Mettal. Mater. Trans.* 27 (1996) 2888–2896.
- [68] N. Saunders, Phase diagram calculations for Ni-based superalloys, *Superalloys* (1996) 101–110.
- [69] B. Sundman, B. Jansson, J.O. Andersson, The thermo-calc databank system, *Calphad* 9 (1985) 153–190.
- [70] N. Dupin, I. Ansara, B. Sundman, Thermodynamic Re-assessment of the ternary system Al-Cr-Ni, *Calphad* 25 (2001) 279–298.
- [71] Y. Ma, A.J. Ardell, The $(\gamma+\gamma')/\gamma'$ phase boundary in the Ni-Al phase diagram from 600 to 1200 °C, *Z. Metallkd.* 94 (2003) 972–975.
- [72] S.S. Bajikar, D.J. Larson, T.F. Kelly, P.P. Camus, Magnification and mass resolution in local-electrode atom probes, *Ultramicroscopy* 65 (1996) 119–129.
- [73] T.F. Kelly, P.P. Camus, D.J. Larson, L.M. Holzman, S.S. Bajikar, On the many advantages of local-electrode atom probes, *Ultramicroscopy* 62 (1996) 29–42.

- [74] T.F. Kelly, D.J. Larson, Local electrode atom probes, *Mater. Char.* 44 (2000) 59–85.
- [75] D.N. Seidman, Perspective: from field-ion microscopy of single atoms to atom-probe tomography: a journey: "Atom-Probe tomography", *Rev. Sci. Instrum.* 78 (2007) 031101, 78 (2007).
- [76] J.H. Bunton, J.D. Olson, D.R. Lenz, T.E. Kelly, Advances in pulsed-laser atom probe: instrument and specimen design for optimum performance, *Microsc. Microanal.* 13 (2007) 418–427.
- [77] D.N. Seidman, K. Stiller, An atom-probe tomography primer, *MRS Bull.* 34 (2009) 717–724.
- [78] D.N. Seidman, Three-dimensional atom-probe tomography: advances and applications, *Annu. Rev. Mater. Res.* 37 (2007) 127–158.
- [79] B. Gault, M.P. Moody, Julie M. Cairney, S.P. Ringer, *Atom Probe Microscopy*, Springer Series in Materials Science, 2012.
- [80] D.J. Larson, T.J. Prosa, R.M. Ufig, B.P. Geiser, T.F. Kelly, *Local Electrode Atom Probe Tomography*, Springer, 2013.
- [81] M.K. Miller, R.G. Forbes, *Atom Probe Tomography: the Local Electrode Atom Probe*, Springer, 2014.
- [82] T. Al-Kassab, H. Wollenberger, G. Schmitz, R. Kirchheim, Tomography by atom probe field ion microscopy, in: F. Ernst, M. Rühle (Eds.), *High-resolution Imaging and Spectrometry of Material*, Springer, Berlin Heidelberg, 2003, pp. 271–320.
- [83] E.Y. Plotnikov, Kinetic Pathways for Phase Separation: an Atomic Scale Study in Ni-Al Alloys, Ph.D. Thesis, Northwestern University (unfinished).
- [84] O.C. Hellman, J.A. Vandebroucke, J. Rusing, D. Isheim, D.N. Seidman, Analysis of three-dimensional atom-probe data by the proximity histogram, *Microsc. Microanal.* 6 (2000) 437–444.
- [85] O.C. Hellman, J. Blatz du Rivage, D.N. Seidman, Efficient sampling for three-dimensional atom probe microscopy data, *Ultramicroscopy* 95 (2003) 199–205.
- [86] L.G. Parratt, *Probability and Experimental Errors in Science: an Elementary Survey*, John Wiley & Sons, New York, 1961.
- [87] A.R.P. Singh, *Mechanisms of Ordered γ' Precipitation in Nickel Based Superalloys*, University of North Texas, 2001. Ph. D. Thesis.
- [88] R. Wagner, R. Kampmann, P.W. Voorhees, *Homogeneous Second-phase Precipitation*, Wiley-VCH, Weinheim, 2001.
- [89] R.P. Kolli, R.M. Wojes, S. Zaucha, D.N. Seidman, A subnanoscale study of the nucleation, growth, and coarsening kinetics of Cu-rich precipitates in a multicomponent Fe-Cu based steel, *Int. J. Mater. Res.* 99 (2008) 513–527.
- [90] R.P. Kolli, D.N. Seidman, Comparison of compositional and morphological atom-probe tomography analyses for a multicomponent Fe-Cu steel, *Microsc. Microanal.* 13 (2007) 272–284.
- [91] M.K. Miller, E.A. Kenik, Atom probe tomography: a technique for nanoscale characterization, *Microsc. Microanal.* 10 (2004) 336–341.
- [92] E.A. Marquis, J.M. Hyde, Applications of atom-probe tomography to the characterisation of solute behaviours, *Mater. Sci. Eng. R Rep.* 69 (2010) 37–62.
- [93] R.A. Karnesky, D. Isheim, D.N. Seidman, Direct measurement of two-dimensional and three-dimensional interprecipitate distance distributions from atom-probe tomographic reconstructions, *Appl. Phys. Lett.* 91 (2007) 013111.
- [94] E. Nembach, *Particle Strengthening of Metals and Alloys*, Wiley-VCH, New York, 1998.
- [95] E.Y. Plotnikov, Z. Mao, R.D. Noebe, D.N. Seidman, Temporal evolution of the γ (fcc)/ γ' (L1₂) interfacial width in binary Ni-Al alloys, *Scripta Mater.* 70 (2014) 51–54.
- [96] J. Stoer, R. Bulirsch, *Introduction to Numerical Analysis*, Springer, New York, NY, 2002.
- [97] G. Martin, Atomic mobility in Cahn diffusion-model, *Phys. Rev. B* 41 (1990) 2279–2283.
- [98] R.W. Balluffi, S.M. Allen, W.C. Carter, *Kinetics of Materials*, J. Wiley & Sons, Hoboken, NJ, 2005.
- [99] K. Compaan, Y. Haven, Correlation factors for diffusion in solids, *Trans. Faraday Soc.* 52 (1956) 786–801.
- [100] J.L. Bocquet, Correlation factor for diffusion in cubic crystals with solute-vacancy interactions of arbitrary range, *Philos. Mag. A* 94 (2014) 3603–3631.
- [101] V.P. Ramunni, Diffusion behavior in Nickel-Aluminum and Aluminum-Uranium diluted alloys, *Comput. Mater. Sci.* 93 (2014) 112–124.
- [102] S. Choudhury, L. Barnard, J.D. Tucker, T.R. Allen, B.D. Wirth, M. Asta, D. Morgan, Ab-initio based modeling of diffusion in dilute bcc Fe-Ni and Fe-Cr alloys and implications for radiation induced segregation, *J. Nucl. Mater.* 411 (2011) 1–14.
- [103] M.J. Stowell, Precipitate nucleation: does capillarity theory work? *Mater. Sci. Tech.-Lond.* 18 (2002) 139–144.
- [104] G. Martin, *The Theories of Unmixing Kinetics of Solid Solutions. Solid State Phase Transformation in Metals and Alloys*, Les Éditions de Physique, Orsay, France, 1978, pp. 337–406.
- [105] K.C. Russell, Nucleation in solids: the induction and steady state effects, *Adv. Colloid Interfac.* 13 (1980) 205–318.
- [106] D. Kashchiev, *Nucleation: Basic Theory and Applications*, Elsevier Science, Oxford, 2000.
- [107] Y. Brechet, G. Martin, Nucleation problems in metallurgy of the solid state: recent developments and open questions, *Comp. Phys.* 7 (2006) 959–976.
- [108] H.Y. Wang, T. Philippe, S. Duguay, D. Blavette, Temperature dependence of nucleation rate in a binary solid solution, *Phil. Mag. Lett.* 92 (2012) 718–725.
- [109] G. Martin, Reconciling the classical theory of nucleation and atomic scale-observations and modeling, in: J.M. Howe D. E. Laughlin, J.K. Lee (Eds.), *International Conference on Solid-Solid Phase Transformations in Inorganic Materials*, 2005, pp. 291–299. Phoenix, AZ.
- [110] E. Clouet, A. Barbu, L. Lae, G. Martin, Precipitation kinetics of Al₃Zr and Al₃Sc in aluminum alloys modeled with cluster dynamics, *Acta Mater.* 53 (2005) 2313–2325.
- [111] J.J. Hoyt, M. Sluiter, B. Clark, M. Kraitchman, D. Defontaine, Anomalous X-ray scattering study of early-stage precipitation in Al-Zn-Ag, *Acta Metall.* 35 (1987) 2315–2322.
- [112] W.O. Gentry, M.E. Fine, Precipitation in Ni-11.1 at% Al and Ni-13.8 at% Al alloys, *Acta Metall.* 20 (1972) 181–190.
- [113] S.A. Hill, B. Ralph, Continuous phase-separation in a nickel-aluminum alloy, *Acta Metall.* 30 (1982) 2219–2225.
- [114] T. Philippe, D. Blavette, P.W. Voorhees, Critical nucleus composition in a multicomponent system, *J. Chem. Phys.* 141 (2014).
- [115] H.I. Aaronson, K.R. Kinsman, K.C. Russell, Volume free energy change associated with precipitate nucleation, *Scripta Metall.* 4 (1970) 101–106.
- [116] G. Rog, A. Kozlowska-Rog, G. Borchardt, L. Dorrer, W. Loser, Determination of the standard Gibbs free energy of the intermetallic compound Ni₃Al in the temperature range (820 to 920) K by a solid-state galvanic cell method, *J. Chem. Thermodyn.* 37 (2005) 97–100.
- [117] J.W. Christian, *The Theory of Transformations in Metals and Alloys-Part I: Equilibrium and General Kinetic Theory*, Pergamon, Oxford, 1975.
- [118] S.V. Prikhodko, J.D. Carnes, D.G. Isaak, A.J. Ardell, Elastic constants of a Ni-12.69 at% Al alloy from 295 to 1300 K, *Scripta Mater.* 38 (1997) 67–72.
- [119] C. Stassis, F.X. Kayser, C.K. Loong, D. Arch. Lattice-dynamics of Ni₃Al, *Phys. Rev. B* 24 (1981) 3048–3053.
- [120] I.S. Servi, D. Turnbull, Thermodynamics and kinetics of precipitation in the copper-cobalt system, *Acta Metall.* 14 (1966) 161–169.
- [121] S.Q. Xiao, P. Haasen, HREM investigation of homogeneous decomposition in a Ni-12 at.% Al alloy, *Acta Metall. Mater.* 39 (1991) 651–659.
- [122] E. Clouet, Modeling of nucleation processes, in: D.U. Furrer, S.L. Semiatin (Eds.), *Fundamentals of Modeling for Metals Processing*, 22A, ASM Handbook, 2009, pp. 203–219.
- [123] G. Jacucci, A. Perini, G. Martin, Monte-carlo computation of cluster free-energies in the ising-model - a test for the validity of the capillary approximation, *J. Phys. A Math. Gen.* 16 (1983) 369–383.
- [124] A. Perini, G. Jacucci, G. Martin, Cluster free-energy in the simple-cubic ising-model, *Phys. Rev. B* 29 (1984) 2689–2697.
- [125] A. Perini, G. Jacucci, G. Martin, Interfacial contribution to cluster free-energy, *Surf. Sci.* 144 (1984) 53–66.
- [126] A.J. Ardell, Precipitate coarsening in solids: modern theories, chronic disagreement with experiment, in: G.W. Lorimer (Ed.), *Phase Transformations*, The Institute of Metals, London, 1988, pp. 485–494.
- [127] J.A. Marquesee, J. Jones, Kinetics of phase transitions: theory of Ostwald ripening, *J. Chem. Phys.* 79 (1) (1983) 373–378.
- [128] L. Ratke, P.W. Voorhees, *Growth and Coarsening*, Springer-Verlag Berlin Heidelberg, 2002.
- [129] J.W. Cahn, J.E. Hilliard, Free energy of a nonuniform system .1. Interfacial free energy, *J. Chem. Phys.* 28 (1958) 258–267.
- [130] J.W. Cahn, J.E. Hilliard, Free energy of a nonuniform system .3. Nucleation in a 2-component incompressible fluid, *J. Chem. Phys.* 31 (1959) 688–699.
- [131] R.A. Swalin, *Thermodynamics of Solids*, Wiley, New York, 1962.
- [132] H. Gleiter, E. Hornbogen, 133 formation of coherent ordered precipitates in Ni-Cr-Al-alloy, *Z. Metallkd.* 58 (1967) 157–163.
- [133] A. Taylor, K.G. Hinton, A study of order disorder and precipitation phenomena in nickel chromium alloys, *J. I. Met.* 81 (1952) 169–180.
- [134] T. Rojhirunsakool, S. Meher, J.Y. Hwang, S. Nag, J. Tiley, R. Banerjee, Influence of composition on monomodal versus multimodal γ' precipitation in Ni-Al-Cr alloys, *J. Mater. Sci.* 48 (2013) 825–831.
- [135] G. Martin, A diffuse interface model for the interfacial transfer coefficient, *Acta Mater.* 53 (2005) 2629–2632.
- [136] S. Meher, T. Rojhirunsakool, J.Y. Hwang, S. Nag, J. Tiley, R. Banerjee, Coarsening behaviour of gamma prime precipitates and concurrent transitions in the interface width in Ni-14 at.% Al-7 at.% Cr, *Phil. Mag. Lett.* 93 (2013) 521–530.
- [137] A.J. Ardell, V. Ozolins, Trans-interface diffusion-controlled coarsening, *Nat. Mater.* 4 (2005) 309–316.
- [138] Z. Mao, C. Booth-Morrison, C.K. Sudbrack, R.D. Noebe, D.N. Seidman, Interfacial free energies, nucleation, and precipitate morphologies in Ni-Al-Cr alloys: calculations and atom-probe tomographic experiments, *Acta Mater.* (2019) 702–714.
- [139] Q.F. Zhang, S.K. Makineni, J.E. Allison, J.C. Zhao, Effective evaluation of interfacial energy by matching precipitate sizes measured along a composition gradient with Kampmann-Wagner numerical (KWN) modeling, *Scripta Mater.* 160 (2019) 70–74.
- [140] M.E. Thompson, C.S. Su, P.W. Voorhees, The equilibrium shape of a misfitting precipitate, *Acta Metall. Mater.* 42 (1994) 2107–2122.
- [141] E.A. Marquis, D.N. Seidman, Coarsening kinetics of nanoscale Al₃Sc precipitates in an Al-Mg-Sc alloy, *Acta Mater.* 53 (2005) 4259–4268.
- [142] W.C. Johnson, J.W. Cahn, Elastically induced shape bifurcations of inclusions, *Acta Metall.* 32 (1984) 1925–1933.
- [143] N. Kurita, M. Koiba, Correlation factor in diffusion in the L1₂ structure for atomic migration via triple defects, *Intermetallics* 10 (2002) 735–741.

- [144] R.A. Swalin, A. Martin, Solute diffusion in nickel-base substitutional solid solutions, *T. Am. I. Min. Met. Eng.* 206 (1956) 567–572.
- [145] C.E. Campbell, W.J. Boettinger, U.R. Kattner, Development of a diffusion mobility database for Ni-base superalloys, *Acta Mater.* 50 (2002) 775–792.
- [146] H. Wendt, P. Haasen, Nucleation and growth of γ' -precipitates in nickel-14 at.% alumum, *Acta Metall.* 31 (1983) 1649–1659.
- [147] A.J. Ardell, R.B. Nicholson, The coarsening of gamma' in Ni-Al alloys, *J. Phys. Chem. Solids* 27 (1966) 1793–1804.
- [148] H.W. Allison, H. Samelson, Diffusion of aluminum, magnesium, silicon, and zirconium in nickel, *J. Appl. Phys.* 30 (1959) 1419–1424.
- [149] M.M.P. Janssen, Diffusion in the nickel-rich part of Ni-Al system at 1000 to 1300 °C; Ni₃Al layer growth, diffusion coefficients, and interface concentrations, *Metall Trans* 4 (6) (1973) 1623–1633.
- [150] W. Gust, M.B. Hintz, A. Lodding, H. Odelius, B. Predel, Impurity diffusion of Al in Ni single-crystals studied by secondary ion mass-spectrometry (SIMS), *Phys. Status Solidi A-Appl. Res.* 64 (1981) 187–194.
- [151] C.G. Lee, K.T. Youn, H.H. Cho, Y.I. Lee, D.S. Yoo, T. Shimozaki, Measurement of the impurity diffusion of Al in Ni by laser induced breakdown spectrometry (LIBS), in: Y. Limoge, J.L. Bocquet (Eds.), 5th International Conference on Diffusion in Materials, 2001, pp. 109–114. Paris, France.
- [152] Q. Wu, S.S. Li, Y. Ma, S.K. Gong, First principles calculations of alloying element diffusion coefficients in Ni using the five-frequency model, *Chin. Phys. B* 21 (2012).
- [153] J. Duan, Y.N. Ossetsky, D.J. Bacon, Atomistic study of self-diffusion in Ni, Al, and Ni₃Al, in: Y. Limoge, J.L. Bocquet (Eds.), 5th International Conference on Diffusion in Materials Location, 2001. Paris, France.
- [154] C. Cserhati, A. Paul, A.A. Kodentsov, M.J.H. van Dal, F.J.J. van Loo, Intrinsic diffusion in Ni₃Al System, *Intermetallics* 11 (2003) 291–297.
- [155] K. Fujiwara, Z. Horita, Intrinsic diffusion in Ni₃Al, in: Y. Limoge, J.L. Bocquet (Eds.), 5th International Conference on Diffusion in Materials, France, Paris, 2001, pp. 565–570.
- [156] J.S. Duan, Atomistic simulations of diffusion mechanisms in stoichiometric Ni₃Al, *J. Phys.-Condens. Mat.* 18 (2006) 1381–1394.
- [157] J.S. Duan, Atomistic simulations of diffusion mechanisms in off-stoichiometric Al-rich Ni₃Al, *J. Phys.-Condens. Mat.* 19 (2007) 1–9.